The Cosmic-Ray Electron Anisotropy Measured with H.E.S.S. and Characterization of a Readout System for the SST Cameras of CTA

Suche nach einer Anisotropie in der Richtungsverteilung kosmischer Elektronen mit H.E.S.S. und Charakterisierung einer Ausleseelektronik für die SST Kameras von CTA

Der Naturwissenschaftlichen Fakultät
der Friedrich-Alexander-Universität Erlangen-Nürnberg
zur Erlangung des Doktorgrades Dr. rer. nat.

vorgelegt von
Manuel Kraus
aus Mannheim

Als Dissertation genehmigt von der Naturwissenschaftlichen Fakultät
der Friedrich-Alexander-Universität Erlangen-Nürnberg

Tag der mündlichen Prüfung:	23.04.2018
Vorsitzender des Promotionsorgans:	Prof. Dr. Georg Kreimer
Gutachter:	Prof. Dr. Stefan Funk
	Prof. Dr. Stefan Schael

Abstract

The cosmic-ray electron energy spectrum has been studied in detail by several experiments, ranging from balloon and satellite experiments to ground-based Cherenkov telescope systems. Data from the High Energy Stereoscopic System (H.E.S.S.) demonstrated in 2008 and 2009 that the large collection area of atmospheric Cherenkov telescopes offers the possibility to analyse the cosmic-ray electron spectrum in the TeV energy range, where satellite experiments suffer from low event rates. Besides the energy spectrum the analysis of the distribution of the electron arrival directions and the search for anisotropies in this observable yields important consequences for astrophysical or dark matter source models. Despite the importance of this measurement, an anisotropy study has not been published so far by any of the ground-based Cherenkov telescope systems. It will be shown in this work, that an anisotropy analysis is possible for Cherenkov telescope arrays despite the large systematics involved in the analysis of the data. The study of the systematics involved in the analysis of Cherenkov telescope data performed in this work for both the electron spectrum and anisotropy is an important pathfinding measurement in the light of the future Cherenkov Telescope Array (CTA).

In the first part of this work, the combined cosmic-ray electron plus positron spectrum is measured using H.E.S.S. data. Compared to previous publications by H.E.S.S. in 2008 and 2009 an advanced event reconstruction technique and a significantly larger dataset is used. The cosmic-ray electron plus positron energy range extends from 300 GeV to 40 TeV. The spectrum is well described by a broken power law with a break energy of $\sim$ 900 GeV. No spectral feature like an upturn in flux, that would hint at the existence of a close-by source, is observed at highest energies. A new technique to analyse anisotropies in the arrival directions of cosmic-ray electrons and positrons with Cherenkov telescopes is introduced. No anisotropy is detected on all angular scales. Upper limits on the dipole anisotropy amplitude on a $\sim 5 - 7\,\%$ level were placed through this work.

In the second part of this work a readout system for the cameras of the small-sized telescopes for CTA is analyzed with respect to the charge resolution performance. It is shown that the TARGET 7 readout system fulfills the CTA requirements assuming some necessary hardware modifications.

Zusammenfassung

Das Spektrum der kosmischen Elektronen und Positronen wurde bisher sowohl mit Ballon- und Satellitenexperimenten, als auch mit Tscherenkovteleskopen untersucht. Im TeV-Bereich sind bodengebundene Detekorsysteme wie z.B. das High Energy Stereoscopic System (H.E.S.S.) dank ihrer großen Detektionsfläche im Vorteil gegenüber Satellitenexperimenten. Der bisher bekannte Bereich des kombinierten Elektronen- und Positronenspektrums erstreckt sich bis zu einer maximalen Energie von 4 TeV. Eine Erweiterung dieses Energiebereichs hin zu höheren Energien ist sehr interessant, da gängige astrophysikalische Produktionstheorien einen Anstieg im Elektronen- und Positronenfluss knapp über 4 TeV vorhersagen. Ein bisher von Tscherenkovteleskopen vernachlässigter Bereich ist die Suche nach Anisotropien in der Richtungsverteilung von kosmischen Elektronen und Positronen. Neben dem Spektrum bei Energien $\geq$ 4 TeV ist die Suche nach einer signifikanten Anisotropie sehr wichtig um z.B. potentiell zwischen einem astrophysikalischen Quellmodel und einer Produktion durch Zerfall dunkler Materie zu unterscheiden.

Im ersten Teil der vorliegenden Arbeit wurde das Spektrum der kosmischen Elektronen und Positronen mit Daten des Tscherenkovteleskopsystems H.E.S.S. untersucht. Im Vergleich zu den 2008 und 2009 veröffentlichten H.E.S.S.-Spektren wurde der Energiebereich auf bis zu 40 TeV deutlich erweitert. Das resultierende Spektrum zeigt keine spektralen Besonderheiten bei Energien größer als 4 TeV, sondern kann in diesem Energiebereich sehr gut dargestellt werden durch ein einfaches Potenzgesetz. Der bereits 2008/2009 entdeckte spektrale Abbruch bei $\sim$ 900 GeV wurde in dieser Arbeit bestätigt. Desweiteren wurde eine Analysemethode für die Suche nach Anisotropien in der Richtungsverteilung von kosmischen Elektronen und Positronen entwickelt, die es trotz der großen Systematiken bei der Auswertung von Tscherenkovteleskopdaten ermöglicht, die Dipol-Amplitude der Anisotropie im Prozentbereich zu untersuchen. Keine signifikante Dipol-Anisotropie wurde im Rahmen dieser Arbeit entdeckt.

Im zweiten Teil dieser Arbeit wurde ein Auslesesystem für die Tscherenkovkameras für das zukünftige Cherenkov Telescope Array (CTA) hinsichtlich seiner Ladungsauflösung charakterisiert. Es wurde gezeigt, dass dieses System mit kleineren Modifikationen die CTA Anforderungen erfüllen kann.

Contents

Part I:

Cosmic-Ray Electron Anisotropy Measured with H.E.S.S.

Preface

The first part of this work is dedicated to the study of cosmic-ray electrons and positrons using the H.E.S.S. experiment. Although small in numbers compared to the total cosmic-ray particle flux, this particle species is extremely interesting for its diagnostics potential towards determining nearby sources of these particles. Electrons and positrons with energies above a few GeV lose energy very rapidly due to synchrotron and inverse compton processes. The energy loss is so drastic for high energies that electrons and positrons in the TeV energy range must have been accelerated in the local environment, where local means source distances of less than 1 kpc. The existence of local electron and positron sources has been implied by the measurement of the combined electron and positron energy spectrum up to 4 TeV by the H.E.S.S. experiment in 2008. Only a small set of astrophysical sources is believed to determine the shape of the energy spectrum of cosmic-ray electrons and positrons at the highest energies beyond 1 TeV. In the extreme case of a single source that dominates the TeV energy range of the spectrum, features like a sharp upturn in flux are predicted by several models, right around the energy range previously covered by Cherenkov telescopes. The combined electron and positron spectrum is not only interesting in itself. Being able to attribute the flux of this species to a specific source type could help to unveil the long-standing question of the existence of primary positron sources. Theories about a possible primary production scenario for positrons first came up when an increase in the positron-to-electron ratio was measured by the PAMELA experiment. Models that can explain this increase exist for both a dark matter and an astrophysical source scenario like pulsars.

The energy spectrum is not the only tool to search for single source imprints. Assuming purely diffuse particle motion in the galaxy, a dipole anisotropy in the arrival direction distribution is expected for a single source scenario. The detection of a strong anisotropy combined with a sharp feature in the energy spectrum would boost the astrophysical source scenario and disfavor the dark matter scenario of positrons. On the other hand a non-detection of an anisotropy with a strong feature in the energy spectrum being present would question the diffusion dominated transport model.

In this work both the combined electron and positron energy spectrum and the anisotropy in the arrival directions was analyzed using data from the H.E.S.S. experiment. The major goal for the energy spectrum was to enlarge the energy range to energies above 4 TeV by

using an advanced event reconstruction technique and a larger data set with respect to the previous publications in 2008 and 2009. Two different analysis chains that are specialized on the reconstruction of electrons and positrons have been developed for this work.

In contrast to the well-established energy spectrum determination technique no published anisotropy analysis method for Cherenkov telescopes prior to this work existed. It will be shown for the first time in this work that such an analysis is possible and that techniques exist that can deal with the high level of systematics of Cherenkov telescope data.

This part is structured as follows:

- The first chapter gives a brief introduction to the properties of cosmic-ray electrons and positrons. Possible production scenarios are introduced and imprints on the energy spectrum and the anisotropy are discussed.
- The second chapter is dedicated to the working principles of Cherenkov telescopes and air-shower physics.
- The third chapter introduces the analysis chains that have been developed for the cosmic-ray electron reconstruction.
- In the fourth chapter the results of the energy spectrum analysis are presented.
- The fifth and sixth chapter show the results of two different anisotropy analysis techniques.
- The seventh chapter summarizes the results of the chapters four to six and discusses possible interpretations of the results.

CHAPTER 1

Introduction: Cosmic-Ray Electrons & Positrons

In this chapter the physical content of the present work is outlined with a strong focus towards cosmic-ray electrons and positrons. Starting point is the all-particle cosmic-ray spectrum as well as its cosmic-ray electron component as measured by several experiments (Section 1.1). In Section 1.2 the standard propagation model for cosmic-ray electrons and the expected energy loss processes are introduced, followed by a section about the most probable production scenarios and source types (Section 1.3). The possible sources contributing to the cosmic-ray electron flux at Earth are introduced in Section 1.4. Predictions about possible imprints of the different production scenarios on the cosmic-ray electron spectrum and the arrival direction anisotropy are made. As this thesis puts special emphasis on the dipole component of the cosmic-ray electron anisotropy, this point is highlighted in particular.

Since the analysis used in this work cannot distinguish electrical charges, the term "electrons" refers to both electrons and positrons throughout the whole work. In the case of a separated treatment of electrons and positrons, the terms "negative electrons" and "positrons" are used. All electron spectra shown in this work are combined electron and positron spectra.

1.1 The Cosmic-Ray Electron Spectrum

In Figure 1.1 the local all-particle cosmic-ray and proton differential energy spectra are shown together with the spectra of cosmic-ray electrons, positrons and antiprotons. This collection of measurements comprises the results of many experiments with a vast variety of detection techniques and over 12 decades of energy. The largest fraction of cosmic rays are protons (87 %). Only roughly 2 % of cosmic rays are electrons, which represent the particles of interest for this work. Higher mass nuclei like alpha particles are of no interest for this work as they can be sorted out very efficiently, leaving cosmic-ray protons as the most significant source of background. A more detailed investigation of possible backgrounds is given in Section 3.1. The local all-particle cosmic-ray spectrum above several GeV/nucleon is well described by a single power law $\frac{dF}{dE} = E^{-\alpha}$ with $\alpha \sim 2.7 - 2.8$ until the onset of a spectral feature called the "knee" at several PeV/nucleon. Cosmic rays are believed to be accelerated in astrophysical

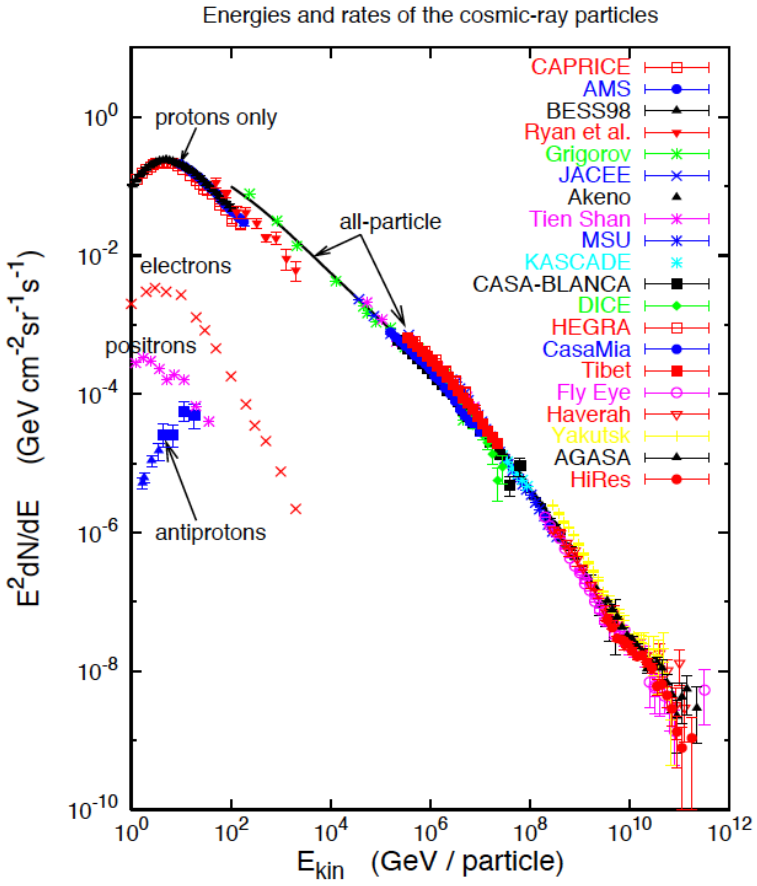

Figure 1.1: Local all-particle differential cosmic-ray energy spectrum and its proton/electron component. Image taken from Hillas (2006).

sources like supernovae or pulsar wind nebulae, the knee is in this context usually thought to mark the limiting energy of galactic accelerators and goes along with a softening of the index to $\alpha \sim 3.0$.

The present knowledge about the cosmic-ray electron spectrum is shown in Figure 1.2. This collection of measurements is dominated by the satellite experiments Alpha Magnetic Spectrometer AMS-02 (Aguilar et al. 2014) and the Fermi Large Area Telescope Fermi/LAT (Abdollahi et al. 2017b). Together they cover the energy range from GeV energies up to 2 TeV. Above 1 TeV the most sensitive experiments so far are ground-based Imaging Atmospheric Cherenkov Telescopes (IACTs) like the High Energy Stereoscopic System H.E.S.S., the Very Energetic Radiation Imaging Telescope Array System VERITAS (Staszak 2015) and the Major Atmospheric Gamma Imaging Cherenkov Telescopes MAGIC (Borla Tridon 2011). With typically 1 km^2 their collection areas are much larger than those of satellite experiments with typically a few m^2 and are therefore much better suited for the high energy regime. However, in the near future two additional satellite experiments, the Dark Matter Particle Explorer DAMPE (Gargano 2017) and the Calorimetric Electron Telescope CALET (Marrocchesi 2015) will tackle the supremacy of IACTs in the Multi-TeV regime. Both experiments have been successfully launched in 2015 and are operating in science data taking mode since $\sim$ 1.5 years.

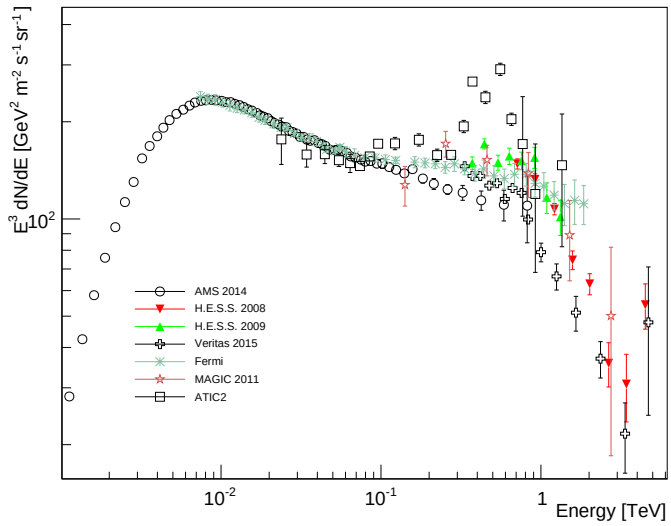

Figure 1.2: Spectrum of cosmic-ray electrons for a selection of experiments including the already published spectra of H.E.S.S. The spectra have been published by AMS-02 (Aguilar et al. 2014), Fermi/LAT (Abdollahi et al. 2017b), ATIC2 (Chang et al. 2008) VERITAS (Staszak 2015) , MAGIC (Borla Tridon 2011) and H.E.S.S. (Aharonian et al. 2008, 2009). Only statistical errors are shown.

According to the cosmic-ray electron analysis published by H.E.S.S. in 2008 and 2009 (Aharonian et al. 2008, 2009), the cosmic-ray electron spectrum above 300 GeV can be well described by a broken power law $dN/dE = k \cdot (E/E_b)^{-\Gamma_1} \cdot (1+(E/E_b)^{1/\alpha})^{-(\Gamma_2-\Gamma_1)\alpha}$ with a normalization $k = (1.5 \pm 0.1)\ 10^{-4}$ TeV^{-1} m^{-2} sr^{-1} s^{-1}, spectral indices $\Gamma_1 = 3.0 \pm 0.1$ and $\Gamma_2 = 4.1 \pm 0.3$ before and after the spectral break energy $E_b = 0.9 \pm 0.1$ TeV. The parameter $\alpha < 0.3$ parametrizes the sharpness of the transition and suggests a very sharp spectral break. The excess in the cosmic-ray electron flux seen by the ballon-borne experiment Advanced Thin Ionization Calorimeter ATIC (Chang et al. 2008) at 300 - 800 GeV could not be confirmed by H.E.S.S. or any other experiment.

The spectral steepening in the TeV regime is observed by all IACT experiments, however, besides H.E.S.S., only the VERITAS experiment can extract a significant spectral break. The latest update of the cosmic-ray electron spectrum of Fermi/LAT excludes a spectral break below 1.8 TeV at 95 % confidence level. Another complication is the fact that the absolute flux normalization among the IACT experiments varies by up to 40 %. This can be traced down to the systematics in the data calibration and analysis, the uncertainty of the absolute energy scale of IACTs and the signal extraction method common to all IACTs and Fermi/LAT. This technique relies heavily on the used hadronic interaction model for the Monte Carlo simulation of protons. This signal extraction technique will be explained in detail in Section 3.3. One of the major motivations of this work is therefore to reinvestigate the cosmic-ray electron spectrum with an increased amount of data with respect to 2008/2009 and to make use of improved/advanced analysis methods. The focus of the spectrum will lie on the spectral break and a possible extension of the energy range beyond 4 TeV.

IACTs are in general not able to distinguish between negative electrons and positrons, therefore both species are not discussed separately in this work. However, the overall size of the positron fraction $f_{e^+}(E)$, defined in Equation 1.1, is important for understanding und

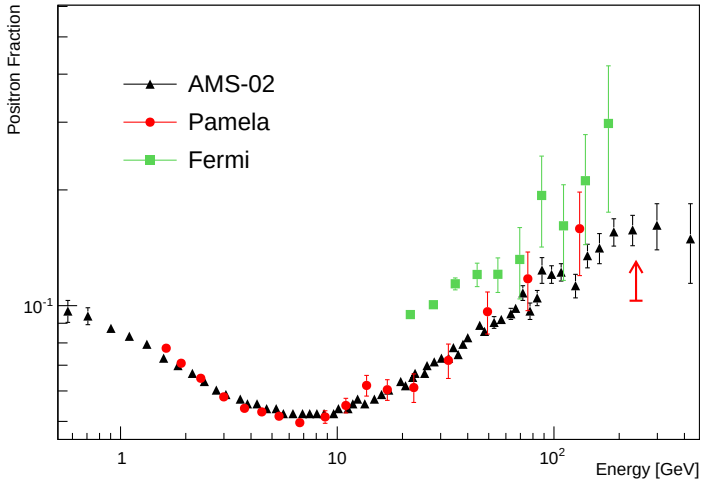

Figure 1.3: Positron fraction measurements for a selection of experiments. Graphs have been processed with data from AMS-02 (Caroff 2016), Fermi/LAT (Ackermann et al. 2012a) and PAMELA (Adriani et al. 2013)

distinguishing possible production scenarios of cosmic-ray electrons.

$$f_{e^+}(E) = \frac{F_{e^+}(E)}{F_{e^+}(E) + F_{e^-}(E)} \tag{1.1}$$

Here $F_{e^+(E)}$ and $F_{e^-(E)}$ are the fluxes of positrons and negative electrons for a particle energy E, respectively. Of particular importance in this aspect are trends like the rise in the positron fraction above 10 GeV. A collection of measurements of the positron fraction is shown in Figure 1.3. The latest update of AMS-02 (Caroff 2016) indicates for the first time a possible end of the high energy upturn. If this saturation will proof to be significant in the future it could be used to distinguish between different production scenarios.

1.2 Propagation and Energy Loss Processes of Cosmic-Ray Electrons

The innergalactic transport of cosmic-ray electrons can be described by the so-called "transport equation" defined in Equation 1.2 (Manconi et al. 2017). Here $N_e\left(\mathrm{E}, t, \mathbf{x}\right)$ is the number of electrons with energy E at time t and position $\mathbf{x}$ and $Q\left(\mathrm{E}, t, \mathbf{x}\right)$ the astrophysical source term. The term $\frac{\partial}{\partial \mathrm{E}}\left(\frac{\partial \mathrm{E}}{\partial t} N_e\right)$ describes the energy loss processes. For Equation 1.2 a pure random walk movement with a spatially invariant diffusion parameter $D\left(\mathrm{E}\right)$ has to be assumed. Terms of the transport equation not relevant for cosmic-ray electrons, like the radioactive decay, are not considered here. They are for example defined by Tinivella (2016).

$$\frac{\partial N_e\left(\mathrm{E}, t, \mathbf{x}\right)}{\partial t} = D\left(\mathrm{E}\right) \nabla^2 N_e + \frac{\partial}{\partial \mathrm{E}} \left(\frac{\partial \mathrm{E}}{\partial t} N_e \right) + Q\left(\mathrm{E}, t, \mathbf{x}\right) \tag{1.2}$$

The diffusion coefficient $D\left(\mathrm{E}\right)$ is usually approximated by a power law with spectral index δ above several GeV/nucleon (Obermeier et al. 2012):

$$D\left(\mathrm{E}\right) = D_0 E^{\delta}. \tag{1.3}$$

The value of δ can be extracted out of the cosmic-ray Boron-to-Carbon ratio. It is assumed that cosmic-ray boron is only produced by spallation of elements like oxygen or carbon during their propagation in the galaxy. In contrast to this, cosmic-ray carbon is believed to be produced directly by supernova nucleosynthesis. By measuring the energy-dependent flux ratio of boron and carbon the influence of the galactic diffusion can be extracted in terms of the energy dependence, parametrized by δ.

The energy loss term for electrons is given by Equation 1.4 and 1.5 (Manconi et al. 2017) with the assumption that, in the covered energy range $> 300\,\mathrm{GeV}$, only energy losses due to synchrotron and inverse compton (IC) interaction are of relevance.

$$\frac{\partial \mathrm{E}}{\partial t} = -k\mathrm{E}^2 \tag{1.4}$$

$$k = \frac{4}{3}\sigma_T c \left(\frac{1}{m_e c^2}\right)^2 \left(\omega_{ph} + \frac{B^2}{8\pi}\right) \tag{1.5}$$

Here m_e is the electron mass, B the galactic magnetic field strength with a typical literature value of $B = 5\,\mu\mathrm{G}$ (Kobayashi et al. 2004) and ω_{ph} the target photon field for IC scattering. The IC target fields can consist out of CMB photons $\left(0.26\,\mathrm{eV/cm^2}\right)$, stellar $\left(0.45\,\mathrm{eV/cm^2}\right)$ or dust $\left(0.20\,\mathrm{eV/cm^2}\right)$ radiation (Mathis et al. 1983). The scattering cross section for both interactions is approximated by the Thompson cross section σ_T. Depending on the target photon field Klein-Nishina corrections to the energy loss rate can become important. For a detailed discussion the reader is referred to Hinton & Hofmann (2009).

In contrast to other charged particle populations like protons, electrons in the GeV-TeV regime lose energy very rapidly due to these energy loss processes. This limits the number of possible electron sources contributing to the cosmic-ray electron flux at Earth to local ones. With Equation 1.4 we can define the livetime of an electron as $\tau = \frac{\mathrm{E}}{\partial \mathrm{E}/\partial t} = 1/\left(k\mathrm{E}\right)$ which gives the time for an electron to lose all its energy E. Since the movement of electrons should be dominated by a diffusive motion, the distance λ travelled in a livetime τ is given by $\lambda = 2\sqrt{D\tau}$ (Atoyan et al. 1995). Using the assumed values for B and ω_{ph} and an energy independent diffusion coefficient $D = (2-5)\cdot 10^{29}\,\mathrm{cm^2 s^{-1}}$ (Kobayashi et al. 2004) the calculated values of $\tau = 4\cdot 10^5\,\mathrm{yr}$ and $\lambda = 0.6 - 0.9\,\mathrm{kpc}$ for 1 TeV electrons illustrate the confinement to local sources, no matter which specific type of source is considered.

1.3 Production of Cosmic-Ray Electrons

The following chapter gives an overview over the types of cosmic-ray electron sources relevant for this work. The question which specific sources might be of interest in the energy range of IACTs will be covered in Section 1.4. For more details about general properties of cosmic-ray electrons and their generation processes the reader is referred to Tinivella (2016); Bell (2013).

In general two different production scenarios of cosmic-ray electrons have to be distinguished. Electrons are said to be of primary origin if they are directly accelerated by astrophysical sources like supernova remnants (SNRs), pulsars and pulsar wind nebulae (PWNs) or generated by dark matter decay and annihilation. Note that not all source types produce both negative electrons and positrons in equal numbers. All of the source types discussed in the

following are also gamma-ray sources, which are important as a contribution to the expected background and will be discussed in Section 3.1.

A secondary origin describes the possibility that electrons are generated by interactions of protons with the interstellar medium (ISM) and a subsequent decay of the scattering products (charged pions and kaons):

$$p + \mathrm{ISM} \rightarrow \pi^{\pm}, K^{\pm} \rightarrow \mu^{\pm} \rightarrow e^{\pm}$$

Neglecting the influence of the charge asymmetry induced by the involved protons, this scenario yields a roughly equal production rate of negative electrons and positrons. Following a very simple argumentation by Kobayashi et al. (2004) the fraction of secondary electrons can be approximated. It is assumed that positrons at energies before the increase in the positron fraction at an energy of $\sim 10\,\mathrm{GeV}$ (see Figure 1.2) are of secondary origin. Positrons beyond this energy might originate from astrophysical sources. Given the positron fraction of 5 % at 10 GeV the flux ratio of secondary to primary electrons yields roughly 10 % at 10 GeV. According to Kobayashi et al. (2004), the spectrum of secondary electrons is expected to be softer with respect to the spectrum of the electron population at the acceleration site (2.7 with respect to 2.4, assuming $\delta \sim 0.3$ in the TeV regime). Therefore the secondary to primary ratio of electrons is expected to decrease with energy according to the difference of both spectral indices and is assumed to be $\sim 2.5\,\%$ at 1 TeV. The primary origin of negative cosmic-ray electrons is therefore regarded as dominant for the present analysis and shall be further explained in the following chapters.

1.3.1 Supernova Remnants

Supernovae are formed after the explosion of a progenitor star that subsequently ejects a large portion of its mass. Based on features in their absorption spectra supernovae are sorted into different classes, type 1a, 1b, 1c and type 2. The expected generation scenario differs between the types. Type 1a supernovae are believed to be formed by the thermonuclear explosion of a degenerate star that accretes mass from a companion object and surpasses its Chandrasekhar limit. In contrast, the collapse of a massive star is believed to be the origin of type 1b, 1c and type 2 supernovae (Tinivella 2016). With the total kinetic energy released in this process being in the order of 10^{51} erg, supernovae could be the main acceleration sites for the observed galactic cosmic-ray population. In the following the evolution of a typical core-collapse supernova is described, since supernovae of type 1a are believed to be very rare events with respect to the total supernova rate (Longair 2011).

The first stage of the evolution of a supernova is governed by the free expansion of the ejecta into the ISM with Mach numbers $M \gg 1$. The expected speed of ejecta and ISM are $\sim (5-10) \cdot 10^3\,\mathrm{km\ s^{-1}}$ and $\sim (1-10)\,\mathrm{km\ s^{-1}}$, respectively (Tinivella 2016). This stage lasts for typically 10^2 to 10^3 years. Once the swept-up material exceeds the mass of the ejected material the supernova enters the so-called "Sedov-Taylor Phase" in which the expansion is significantly slowed down. This phase is believed to last for $\sim 10^4$ years. In the third phase, the temperature inside the supernova drops below $10^6\,\mathrm{K}$ and electron recombination with heavy elements becomes important. One characteristic of this phase is the cooling by line emission of heavy ions (Longair 2011). After this radiation stage the expansion finally becomes subsonic and the supernova merges with the ISM. Supernovae in this late stage are believed to be roughly 10^5 years old. In the first two phases the high Mach numbers of the

ejecta leads to the formation of a shock with a discontinuous increase in density and pressure moving from upstream to downstream of the shock. The presence of strong magnetic turbulences in the vicinity of the shock (both up- and downstream) enable a very efficient acceleration method for charged particles called "Diffusive Shock Acceleration" (DSA).

The idea of a stochastical particle acceleration by elastic reflection on magnetic turbulences in interstellar clouds was for the first time proposed by Fermi (1949). In this framework charged particles gain energy if they are scattered on the turbulences head-on and lose energy in the case of a tail-on scattering. This leads to an average energy gain $\langle \delta E \rangle \sim (\frac{u}{c})^2$ where u is the speed of the cloud and the particles are assumed to move with the speed of light c. The dependence on $(\frac{u}{c})^2$ makes this acceleration scenario rather inefficient, the biggest problem being the presence of both head-on and tail-on collisions.

This problem is circumvented in the case of a strong shock in supernovae. The following model is for example discussed by Bell (2013). Magnetic turbulences both up- and downstream act as magnetic mirrors like in the case of the scattering at clouds. Both the shocked rest frame downstream, as well as the un-shocked rest frame upstream see approaching material from across the shock front. Therefore unlike to the case of the scattering at clouds this time there are only head-on collisions. The particles can cross the shock multiple times and gain energy for every crossing with the average energy gain $\langle \delta E \rangle \sim \frac{u}{c}$ and are therefore accelerated much faster. This model of the Diffusive Shock Acceleration is only valid under the assumption of a fast directional isotropization after a shock crossing. In order to guarantee the acceleration to highest energies ($\sim$TeV and maybe even up to the knee) the magnetic field B needed is believed to be $\mathrm{B} \sim 100\,\mu\mathrm{G}$, which is much higher than the usual magnetic field in the ISM. These high magnetic field strengths can only be explained in the context of magnetic field acceleration in streaming instabilities (Bell 2013).

The accelerated particles have an equal probability to escape downstream with the advective flux of the shocked ISM for every crossing of the shock. This naturally produces a power law in the number of generated particles $n(E)$ with respect to the energy E. Together with a maximum reachable energy E_{max}, which in the case of electrons is given by the onset of the domination of radiative losses over the energy gain, the expected injected particle spectrum can be written as:

$$n(\mathrm{E}) \propto \mathrm{E}^{-\gamma_{inj}} \exp\left(-\mathrm{E}/\mathrm{E}_{max}\right) \tag{1.6}$$

Here γ_{inj} is the resulting spectral index of the injected power law spectrum, which is considered to be around 2 for a strong shock with a high Mach number (Bell 2013).

One of the biggest unknowns in the modelling of a SNR electron spectrum arriving at Earth is the time of injection τ_{inj} of the electrons. The electrons are considered to be trapped inside the shock front until it merges with the ISM Kobayashi et al. (2004), which happens roughly after $10^5\,\mathrm{yr}$. This makes the contribution of very young sources rather unlikely, at least for this very simple model of the supernova evolution. In principle all charged particles can take part in the DSA processes, in the case of supernova shocks mainly protons and negative electrons from the shocked ISM are considered.

1.3.2 Pulsars and Pulsar Wind Nebulae

The degenerate, rapidly spinning neutron star that is left from the supernova of a massive star together with its particle wind nebula is considered another possible acceleration source

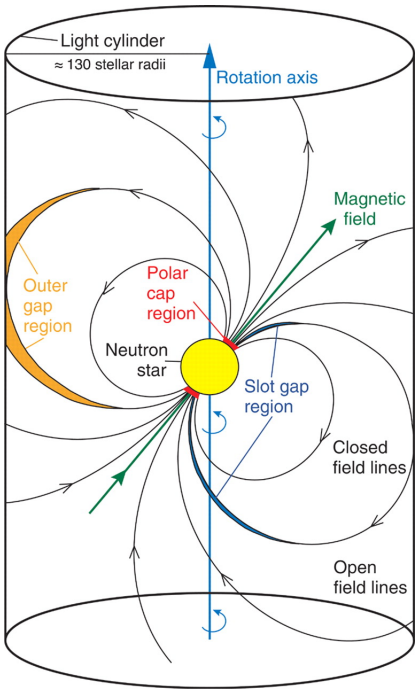

Figure 1.4: Illustration of the geometry of a pulsar system with its magnetic field, magnetosphere and light cylinder. The expected sites of particle acceleration (polar cap, outer gap and slot gap regions) are also depicted. Image taken from Aliu et al. (2008).

of cosmic-ray electrons. These stars were first detected at radio wavelengths as point sources showing a pulsed emission and were therefore named pulsars. The description and explanation of the acceleration of charged particles and the pulsar system in general is very complex and shall only be scetched in the following. For a detailed view the reader is referred to explicit reviews (Kirk et al. 2009; Gaensler & Slane 2006).

The most striking characteristics of a pulsar is its strong dipolar magnetic field with field strengths of up to 10^{15} G. Assuming a perfectly conductive stellar interior it has been shown by Goldreich & Julian (1969) that the electric field component $\mathbf{E}_{\parallel}$ parallel to the magnetic field near the pulsar surface is strong enough to rip off charged particles. They are fed to a so-called "magnetosphere", a dense plasma that is co-rotating with the pulsar. Outside the so-called "light cylinder" the resulting rotation speed of the particles would be superluminal which leads to open magnetic field lines. Particles can escape the pulsar system since they are gyrating around the field lines (see Figure 1.4).

In the force-free case where all electrical charges in the plasma are screened, $E_{\parallel}$ vanishes and no acceleration of particles can take place. A complete screening is only given if the charge density equals the Goldreich-Julian charge density $\rho \simeq \mathbf{\Omega} \cdot \mathbf{B}/2\pi c$, where $\mathbf{\Omega}$ is the angular velocity and $\mathbf{B}$ the magnetic field vector. In polar cap models this charge density is not reached in charge depleted zones at the polar caps and therefore $E_{\parallel} \neq 0$. In outer gap or slot gap models acceleration areas are connected to the last closed magnetic field lines inside the light cylinder. In both models charged particles are accelerated and emit synchrotron photons that create cascades of e^+e^- pairs in the strong magnetic field environment. This so-called "pulsar wind" of supersonically moving particles form a nebula around the pulsar that is eventually terminated in a strong shock. Particle reacceleration of both negative electrons and positrons can take place at this shock via the DSA process previously discussed for the

case of supernova remnants. Like in the case of the acceleration at the SNR shock, usually mature sources with ages larger than 50 kyr are considered for the modelling of the local electron spectrum (Manconi et al. 2017). Since in a PWN-dominated production scenario of cosmic-ray electrons both negative electrons and positrons are accelerated, this scenario could naturally explain the increase in the positron fraction and the resulting primary origin of positrons above particle energies of 10 GeV.

1.3.3 Dark Matter

Another possible source of cosmic-ray electrons is the production by self-annihilation or decay of dark matter (DM) particles. The DM particle population is in most models expected to consist of weakly interacting, massive non-standard model particles that can decay to two photons, two leptons or other pairs like quarks. Like in the case of a PWN dominated production scenario equal numbers of negative electrons and positrons would be generated. In 2016 the dark matter scenario of the cosmic-ray electron production (and especially the positron production) draw a lot of attention, when for the first time the measured AMS-02 positron fraction seemed to saturate above $\simeq 300$ GeV (see Figure 1.3). It could be shown (for example by Kopp (2013)) that the self-annihilation of dark matter particles with masses ~ 1 TeV could explain the AMS-02 data.

The biggest issue for most DM theories is the prediction of annihilation cross-sections orders of magnitude lower than the level that is needed to explain the measured cosmic-ray electron flux. Some theoretical models propose physical mechanisms that could boost the cross-sections like the very popular Sommerfeld enhancement (Sommerfeld 1931). This would however also lead to an increased gamma-ray flux from dark matter sources that should have been detected by Fermi/LAT in the isotropic gamma-ray background, for example discussed by Bringmann et al. (2014). Furthermore the existence of a primary positron population due to dark matter decay or annihilation should also give rise to a primary antiproton population that has not been discovered so far by AMS-02 (Nozzoli 2017). This argumentation is of course only valid for dark matter models that are not restricted to the decay or annihilation into photons or leptons.

1.4 Source Imprints on the Electron Spectrum and Anisotropy

Local Sources

As already pointed out in Section 1.2 cosmic-ray electrons with an energy of 1 TeV are considered to be produced by sources in the local environment. Local in this context is defined as a source distance d $\leq$ 1 kpc. In Table 1.1 all possible local SNRs in the Green catalog are listed (list taken and adapted from Di Mauro et al. (2014)). Additionally, PWNe are listed that are considered to be most powerful according to the analysis done in Di Mauro et al. (2014). Other local PWNe are considered to be too weak to have a significant contribution to the cosmic-ray electron flux at Earth. The analysis in this work will focus on the Vela SNR/PWN, Monogem PWN and Geminga PWN since these sources are in most models considered to contribute the most to the local electron flux in the TeV energy range and, even more important, their source positions are within the sky region observed by H.E.S.S.. In the case of a dark matter dominated electron flux one possible scenario is discussed by

Source [Green/ATNF]	Other Name	d [kpc]	Age [kyr]
SNRs :			
G065.3+05.7		0.9 ± 0.1	26
G065.7+01.2		[1.0, 1.8]	20
G074.0-08.5	Cygnus Loop	0.58 ± 0.06	10
G114.3+00.3		0.7	7.7
G127.1+00.5	R5	1.0 ± 0.1	[20,30]
G156.2+05.7		0.9 ± 0.3	[15,26]
G160.9+02.6	HB9	0.8 ± 0.4	[4,7]
G263.9-03.3	Vela SNR	$0.294^{+0.76}_{-0.50}$	11.3
G266.2-01.2	Vela Jr.	0.75	[1.7,4.3]
G347.3005		1	[1.6,4.9]
PWNe :			
J0633+1746	Geminga	0.25	343
B0656+14	Monogem	0.28	112
J0835-4510	Vela X	0.29	11.3

Table 1.1: List of potential SNRs/PWNe contributing to the cosmic-ray electron flux, taken from Di Mauro et al. (2014) with an additional cut to the distance $d \leq 1\,\mathrm{kpc}$. Additionally PWNe from the ATNF catalog (Manchester et al. 2005) that are considered as "powerful sources" are given. The Vela region was split into the SNR and the PWN Vela X.

Borriello et al. (2012). In this model the existence of DM substructures/clumps additionally to a smooth DM halo around the galactic center is discussed. Clumps that are close to Earth might have a significant contribution to the cosmic-ray electron flux. The fact that these close DM substructures should have been detected in the gamma-ray channel will be ignored in the following.

The cosmic-ray electron spectrum in the TeV regime should be dominated by these handful of sources, possible spectral features in the energy spectrum can be traced down to single sources. The exact shape of the energy spectrum depends very sensibly on source parameters like distance d, injection time τ_{inj} and on the galactic diffusion coefficient D. Possible astrophysical source models can be found in Kobayashi et al. (2004) and Manconi et al. (2017). Most astrophysical cosmic-ray electron models have in common that, if τ_{inj} is considered to be smaller than 10 kyr, the young Vela SNR dominates the electron spectrum in the TeV regime. In some of these Vela SRN scenarios a strong upturn in the electron flux above several TeV is predicted (see Figure 1.5). Assuming conservative injection times in the order of 100 kyr, older sources like the Monogem PWN should determine the shape of the energy spectrum at TeV energies. In this scenario electrons accelerated by Vela are not yet released into the ISM. In this case however a strong spectral feature at energies of multiple TeV is rather unlikely, since the electron flux contribution of older sources like Monogem is considered to be restricted to lower energies than for Vela. The comparison between a dominating Vela SNR and a Monogem PWN production scenario is shown in Figure 1.5.

Models specifically dealing with the flux contribution of the Vela PWN region (Vela X) suggest production scenarios of cosmic-ray electrons that circumvent the issue of the very young age of the Vela PWN. In the model proposed by Hinton et al. (2011) (see Figure 1.6) cosmic-ray electrons from Vela X are not confined to the PWN due to the interaction of the

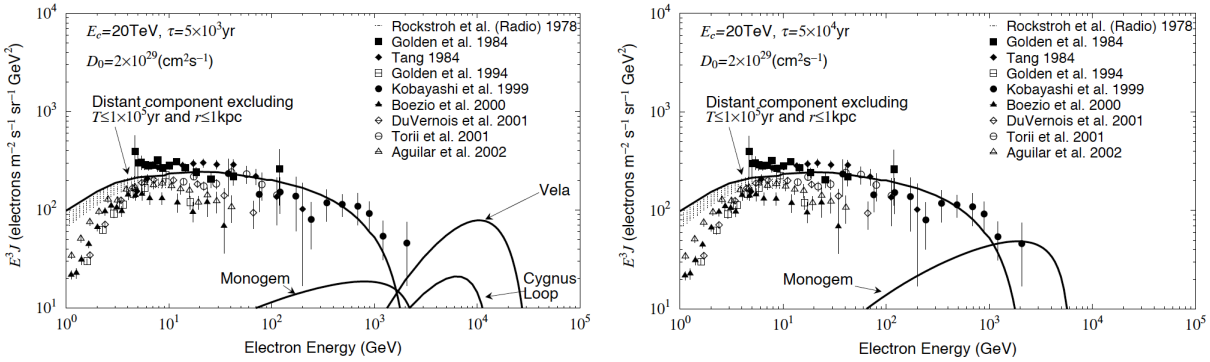

Figure 1.5: Calculated cosmic-ray electron spectra with a separated distant SNR component plus single source contributions, taken from Kobayashi et al. (2004) assuming a cutoff energy $E_c = 20\,\mathrm{TeV}$ in the injection spectrum and a diffusion coefficient $D_0 = 2 \cdot 10^{29}\,\mathrm{cm^2 s^{-1}}$. *Left*: injection time $\tau_{inj} = 5\,\mathrm{kyr}$ *Right*: $\tau_{inj} = 50\,\mathrm{kyr}$. For small injection times or even a prompt release, the Vela SNR should determine the shape of the energy spectrum at TeV energies.

PWN shock front with a reverse shock from the SNR. This leads to an upturn in the local cosmic-ray electron flux just above the energy range that is currently covered. This makes an extension up to higher energies very interesting and a primary subject of this work.

Cosmic-Ray Electron Anisotropy

Under the assumption that only a few (or even a single) sources contribute to the TeV flux of cosmic-ray electrons not only imprints in the energy spectrum itself, but also on the arrival directions of cosmic-ray electrons are expected. Neglecting all angular scales but the dipole component, the cosmic-ray electron anisotropy δ can be defined as:

$$\delta = \frac{I_{max} - I_{min}}{I_{max} + I_{min}}. \tag{1.7}$$

Here I_{max} and I_{min} are, respectively, the maximum and minimum flux intensity of cosmic-ray electrons measured over the whole (accessible) sky. Following Mao & Shen (1972) a local electron source i will induce a dipolar anisotropy with amplitude δ_i under the assumption of isotropic diffusion:

$$\delta_i = \frac{3D}{c} \frac{\nabla \Psi_i}{\Psi_i}. \tag{1.8}$$

Here Ψ_i is the number density of electrons measured at Earth and D is the diffusion coefficient. Depending on which source exactly determines the shape of the energy spectrum at TeV energies, the predicted anisotropy values (Manconi et al. 2017) range from a few % in the case of a dominating Vela SNR (see Figure 1.7) to $\delta < 0.1\%$ in the case of dominating PWNe. Also shown in Figure 1.7 is a prediction by Borriello et al. (2012) for the dark matter production scenario. In this scenario the anisotropy originates from fluctuations in the number density of dark matter substructures in the Earth's local environment, this effect should lead to rather low anisotropy values, like in the PWNe scenario.

The dipole anisotropy models discussed before are in general only valid for a special galactic magnetic field configuration. A more general model of the expected degree of dipole anisotropy of cosmic-rays is discussed in Mertsch & Funk (2015). By separating the magnetic field **B**

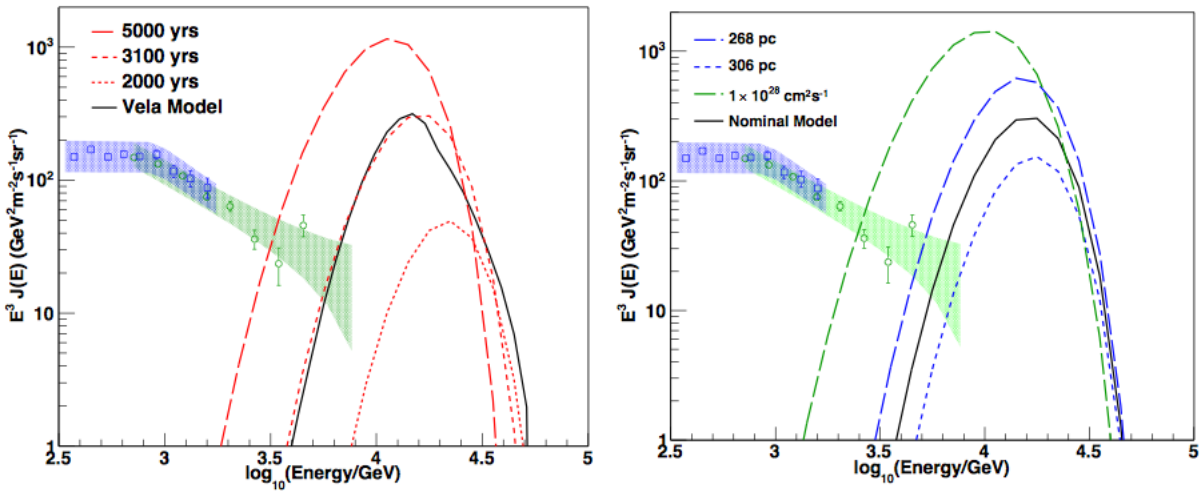

Figure 1.6: Predicted cosmic-ray electron spectrum from the PWN Vela X with the production scenario of Hinton et al. (2011) and the flux measured by H.E.S.S. (Aharonian et al. 2008, 2009). *Left*: Effects of varying burst-like injection times in red and a time dependent injection model in black. *Right*: Effects of varying source distance (blue) and diffusion coefficient (green, nominal model $D = 5 \cdot 10^{27}\,\mathrm{cm^2 s^{-1}}$).

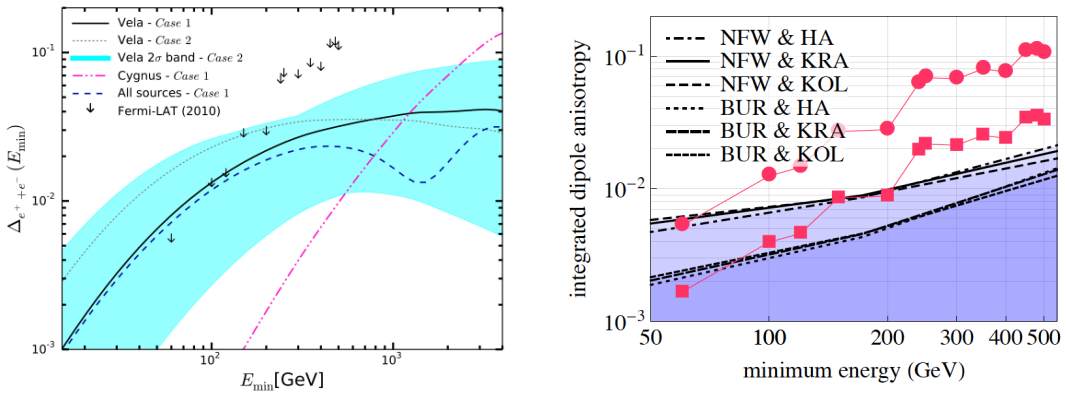

Figure 1.7: Predictions for the cosmic-ray electron dipole anisotropy. *Left*: Single source scenario for the Vela + Cygnus SNR from Manconi et al. (2017). Case 1 & 2 models refer to different Vela SNR source parameters. The 2010 Fermi/LAT dipole upper limits (Ackermann et al. 2010) are also depicted, the 2017 Fermi/LAT upper limits (Abdollahi et al. 2017a) eventually rule out this scenario *Right*: Dark matter scenario from Borriello et al. (2012) with the 2010 Fermi/LAT upper limits (red circles) and the expected 10 year sensitivity (red squares).

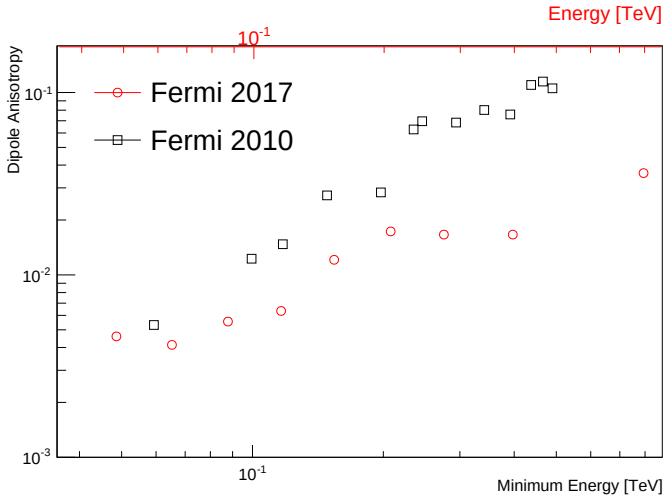

Figure 1.8: Fermi/LAT upper limits on the dipole amplitude of the cosmic-ray electron anisotropy. The 2010 anisotropy analysis was performed using energy thresholds, the 2017 analysis used energy bins. The plot was generated with data from Ackermann et al. (2010); Abdollahi et al. (2017a).

into a regular field $\mathbf{B_0}$ and a turbulent field $\delta\mathbf{B}$ the level of turbulence η can be defined as:

$$\eta = \frac{\delta B^2}{\delta B^2 + B_0^2} \tag{1.9}$$

$$\mathbf{B} = \mathbf{B_0} + \delta\mathbf{B} \tag{1.10}$$

Only in the special case that the level of turbulence is high ($\eta \simeq 1$) the anisotropy models discussed before are considered to be valid. In the case of a strong regular magnetic field component, the level of measured anisotropy strongly depends on the misalignment between electron source and $\mathbf{B_0}$. For a misalignment of 90 ° the dipole anisotropy would be heavily suppressed. In this case a strong spectral feature, like an upturn in the electron flux, in the energy spectrum would not automatically induce a high level of dipole anisotropy. On the other hand if a spectral feature is observable in the electron spectrum without a strong dipole anisotropy this would have strong implications on the galactic magnetic field configuration.

So far the only experiment that studied the cosmic-ray electron anisotropy in the GeV-TeV energy range is Fermi/LAT. In 2017 the published upper limits from 2010 (Ackermann et al. 2010) were updated (Abdollahi et al. 2017a) down to a dipole anisotropy level of $< 1\,\%$. This analysis showed for the first time enough sensitivity to seriously constrain the most popular scenario of a dominating Vela SNR (see Figure 1.8). Anisotropy studies of diffuse emission with IACTs are much more challenging than with satellite experiments due to the only partial coverage of the sky and the high level of systematics linked to atmospheric variations. So far it has not been shown that it is even possible for IACTs. In this work a new anisotropy study technique is introduced that for the first time is capable of opening the anisotropy field for IACTs. Upper limits on the dipole amplitude will be derived in order to confirm the very restrictive upper limits from the 2017 Fermi/LAT analysis.

CHAPTER 2

Indirect Detection of Cosmic Rays with H.E.S.S

The direct detection of cosmic rays and gamma rays using satellites and balloon-borne instruments has shown its capabilities in the past for example with the very successful AMS and Fermi/LAT experiments. This detection technique however fails to collect a substantial amount of statistics at the highest energies ($\sim$ TeV) due to the steeply falling energy spectra of all involved particles and the very small effective detection area. Due to atmospheric absorption of cosmic rays and gamma rays a direct detection of GeV-TeV particles on earth is not possible. However, the fact that cosmic rays and gamma rays form so-called "air showers" when interacting with nuclei in the atmosphere makes an indirect detection possible. The atmosphere is thereby treated as the calorimeter part of the detector. The secondary charged particles that are produced in these air showers emit Cherenkov light. The Cherenkov light can be detected by telescope cameras with a nanosecond exposure time and the properties of the involved particle can be reconstructed. One of the first successful uses of this detection technique was reported by the Whipple observatory in 1989 (Weekes et al. 1989) with the detection of gamma rays coming from the Crab nebula. In 1996 the High Energy Gamma Ray Astronomy (HEGRA) experiment followed using the first stereoscopic reconstruction of air shower events (Kohnle et al. 1996). Today there a four operational IACTs with MAGIC, H.E.S.S., VERITAS and CANGAROO (Ebisuzaki et al. 1991). The future Cherenkov Telescope Array CTA (Acharya et al. 2013), as an advancement of all predecessor experiments, is well on track.

In this chapter the generation of air showers (Section 2.1) and their detection using the indirect IACT technique is explained (Section 2.2). The simulation of air shower events as one of the most important challenges in the analysis of Cherenkov telescope data is introduced in Section 2.3. The H.E.S.S. experiment itself, its standard data taking mode and analysis method, as well as the standard background-rejection technique will be explained in Section 2.4. Despite being specifically developed for the detection of gamma rays it will be shown in the later chapters that adapted analysis chains from the H.E.S.S. experiment can be utilized to detect and reconstruct cosmic-ray electron events.

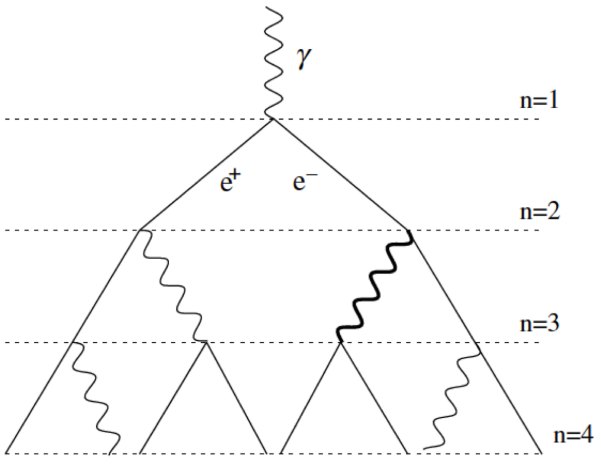

Figure 2.1: Heitler model for the generation of an electromagnetic shower initiated by a gamma ray. The interaction layers n are separated by one radiation length. Each node is either associated with a e^+e^- pair-production or the emission of a bremsstrahlung photon. Image taken from Matthews (2005).

2.1 Air Shower Generation

When entering the Earth's atmosphere cosmic rays and gamma rays interact with the atoms therein and cascades of secondary particles are generated. The underlying interaction mechanisms differ depending on the type of the primary particle. The resulting showers can be roughly grouped into two types, "electromagnetic air showers" and "hadronic air showers".

Electromagnetic Showers

Electromagnetic showers, which are initiated by gamma rays and cosmic-ray electrons, can be very efficiently described by the Heitler model (Heitler 1938) and its extension by Matthews (Matthews 2005). In this model gamma rays and electrons undergo successive two-body splittings in the coloumb field of atmospheric nuclei with one-photon bremsstrahlung as interaction process for electrons and e^+e^- pair-production for gamma rays. The distance d travelled between two interaction steps is $d = \ln 2 \; \mathrm{X}_0$ for bremsstrahlung and $d = \ln 2 \; \frac{9}{7} \; \mathrm{X}_0$ for pair-production with X_0 being the radiation length for the bremsstrahlung process. In the Heitler model the radiation length X_0 is used for both processes as an approximation. Usually d is called the "splitting length".

The growth of the number of particles at each interaction step ends when the energy losses of the radiative processes equal the losses of ionization processes which happens below the critical energy E_c ($E_c \simeq 85\,\mathrm{MeV}$ in air). The total number of particles N at each interaction layer n is given by $N = 2^n$, where interaction layers are defined to have a distance of one splitting length to each other (see Figure 2.1). The maximum shower height X_{max} can be defined as the distance to the first interaction point at which the number of particles in the shower reaches its maximum N_{max}:

$$X_{max} = n_c \; \ln 2 \; X_0. \tag{2.1}$$

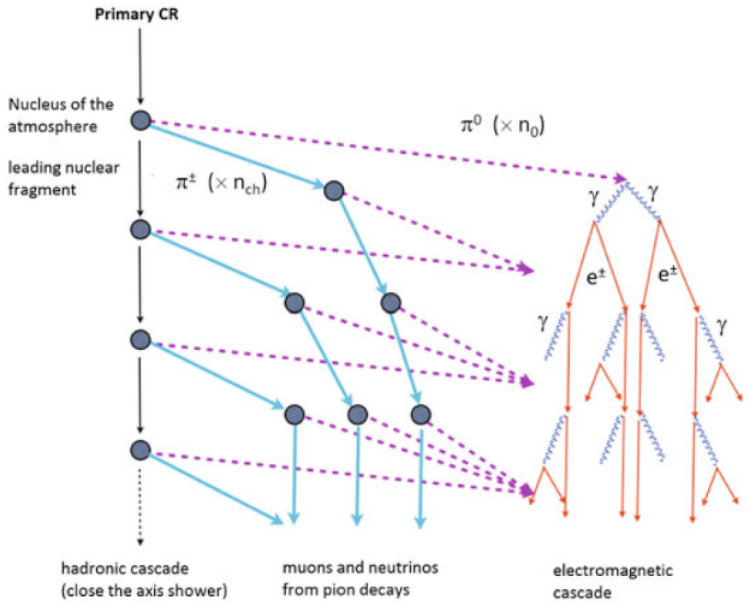

Figure 2.2: Hadronic shower model by Spurio (2014) that only takes pion production into account. The most important quantity is the amount of energy transferred from the hadronic to the electromagnetic component.

Here n_c is the interaction layer where ionization processes start to dominate. Two very important conclusions can be drawn from the Heitler model:

$$N_{max} = 2^{n_c} = \frac{E_0}{E_c} \tag{2.2}$$

and

$$X_{max} = X_0 \ln \frac{E_0}{E_c}. \tag{2.3}$$

Here E_0 is the initial energy of the primary particle. The Heitler model hence predicts that the maximum number of particles N_{max} in the shower is proportional to the initial energy E_0 of the primary particle. Furthermore the maximum shower height X_{max} is proportional to the logarithm of E_0. Both variables are very important indirect shower parameters for the reconstruction of the primary particle. With $X_0 = 37.2\,\mathrm{g/cm^2}$ the maximum shower height can be calculated to be $X_{max} \simeq 350\,\mathrm{g/cm^2}$ for gamma rays and electrons with an energy of 1 TeV, corresponding roughly to a height above sea level of $\simeq 10\,\mathrm{km}$. The value for X_{max} depends heavily on the zenith angle of the incident primary particle and the atmospheric conditions. Since the shower evolution for gamma rays and cosmic-ray electrons only differs in the first interaction step both particles species are considered to be indistinguishable for IACTs.

Hadronic Showers

The shower development for protons or heavier nuclei as primary particles is much more complex as in the case of a pure electromagnetic shower since also strong and weak interactions take place. With an interaction length of $X_0 \simeq 120\,\mathrm{g/cm^2}$ (Gaisser 1990) hadronic showers start deeper in the atmosphere. The secondary particles produced by interactions with the nuclei in the atmosphere can be grouped into two classes, a hadronic cascade of nuclear

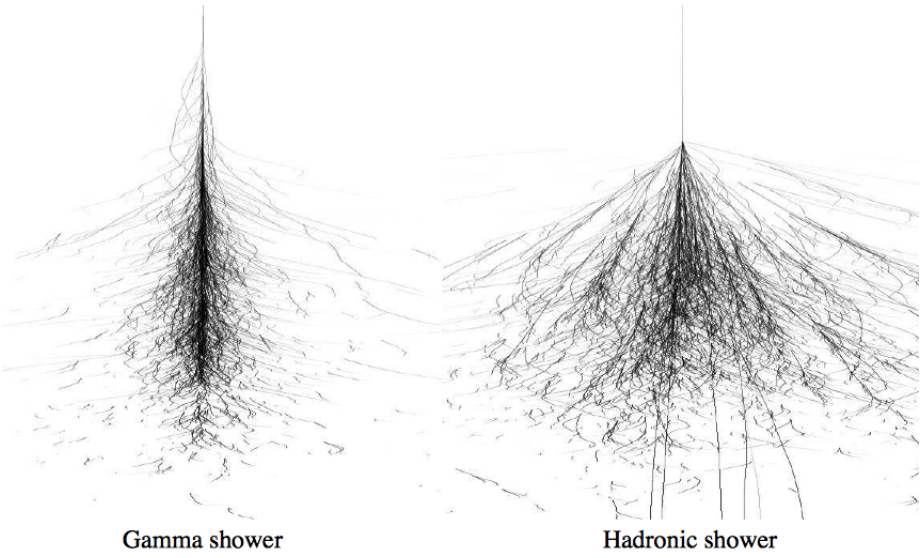

Figure 2.3: Simulated air showers for a primary gamma-ray (*left*) and a primary proton (*right*). The proton shower shows a much more irregular geometry and a smaller alignment to the shower axis. Image taken from Völk & Bernlöhr (2009).

fragments and an electromagnetic component of leptons and gamma rays. The evolution and therefore the geometry of the shower depends strongly on the amount of energy that is transferred from the hadronic to the electromagnetic component (see Figure 2.2).

In the simplest model, for example discussed by Spurio (2014) or Matthews (2005), only the production of pions is considered to determine the average evolution of a hadronic shower, whereas in reality also other hadrons can be produced. The main decay channels of the produced pions are given by

$$\pi^{\pm} \rightarrow \mu^{\pm} + \nu_{\mu}(\bar{\nu_{\mu}}) \tag{2.4}$$

$$\pi^{0} \rightarrow \gamma + \gamma. \tag{2.5}$$

Neutral pions initialize purely electromagnetic sub-showers, but also charged pions can contribute to the electromagnetic component by the production of muons and subsequent electron production.

Due to the large transverse momenta that can be generated by strong interactions, the geometry of hadronic showers is much more irregular than in the case of electromagnetic showers. An illustration of a shower initiated by a gamma ray and a shower initiated by a proton is depicted in Figure 2.3, The secondary particles in the gamma-ray shower are much more aligned to the shower axis than in the case of the primary proton. Since the event classification in IACT analysis chains is based on shower geometry, the biggest threat are the electromagnetic sub showers initiated by neutral pions.

2.2 Detection of Air Shower Events with IACTs

The detection of air shower events is based on their emission of Cherenkov photons. Charged particles, most dominantly electrons, polarize a dielectric medium when traversing trough it.

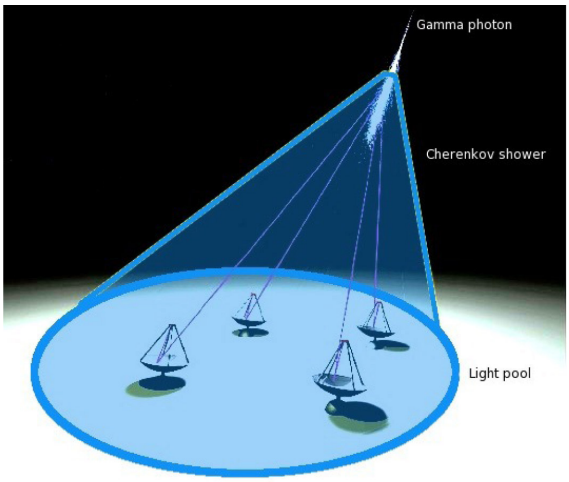

Figure 2.4: Illustration of the Cherenkov light cone induced by a gamma-ray air shower for a H.E.S.S.-like IACT array with four telescopes. Image taken from Canestrari (2011).

If the velocity of the particle exceeds the phase velocity of the medium the electromagnetic waves emitted by the atoms in the medium interfere constructively and form a common shock front. This is called Cherenkov radiation. The opening angle Θ of the Cherenkov light cone is given by the relation

$$\cos\Theta = \frac{1}{n\beta}. \tag{2.6}$$

Here n is the refractive index of the dielectric medium and $\beta = \frac{v}{c}$ the particle velocity divided by the speed of light. In air the opening angle is roughly $\simeq 1\,^\circ$. The necessary condition $n\beta > 0$ gives the threshold energy E_{th} for the Cherenkov effect, which is determined to be $\simeq 20\,\mathrm{MeV}$ for electrons in air.

Since the Cherenkov light emitted by an electromagnetic shower is not produced by a single, but rather by an ensemble of electrons, the Cherenkov light reaches the earth as a filled "light pool" with a radius of about 125 m for gamma rays with an energy of 1 TeV (Völk & Bernlöhr 2009). The maximum of the Cherenkov spectrum lies in the ultraviolet wavelength range, but due to strong absorption the observed maximum is at $\simeq 330\,\mathrm{nm}$ at sea level. The Cherenkov light flash only lasts for a few nanoseconds, outshining the otherwise dominant night sky background (NSB, usually $\leq 100\,\mathrm{MHz}$ for H.E.S.S.).

Telescopes positioned in the light pool can trigger on the Cherenkov light flash and generate images of the Cherenkov shower. If more than one telescope is situated in the light pool, the shower can be recorded from multiple perspectives (see Figure 2.4). This yields the advantage of a stereoscopic reconstruction of an air shower event. It is therefore usually requested that more than one telescope triggered on an event. The cameras of Cherenkov telescopes need a very small exposure time and a fast readout technique. In the past the pixels of these cameras consisted out of fast photomultiplier tubes (PMTs), for the upcoming CTA also telescopes with silicon photomultipliers are planned (for example discussed in Otte et al. (2015)). For gamma-ray-like events the pixelized images can be well parametrized as an ellipse, for hadronic events the majority of images show an irregular shape. In Figure 2.5 this is shown for the example of a simulated TeV gamma-ray event and a proton event for one of the H.E.S.S. cameras. In order to calibrate IACTs, simulations of air shower events

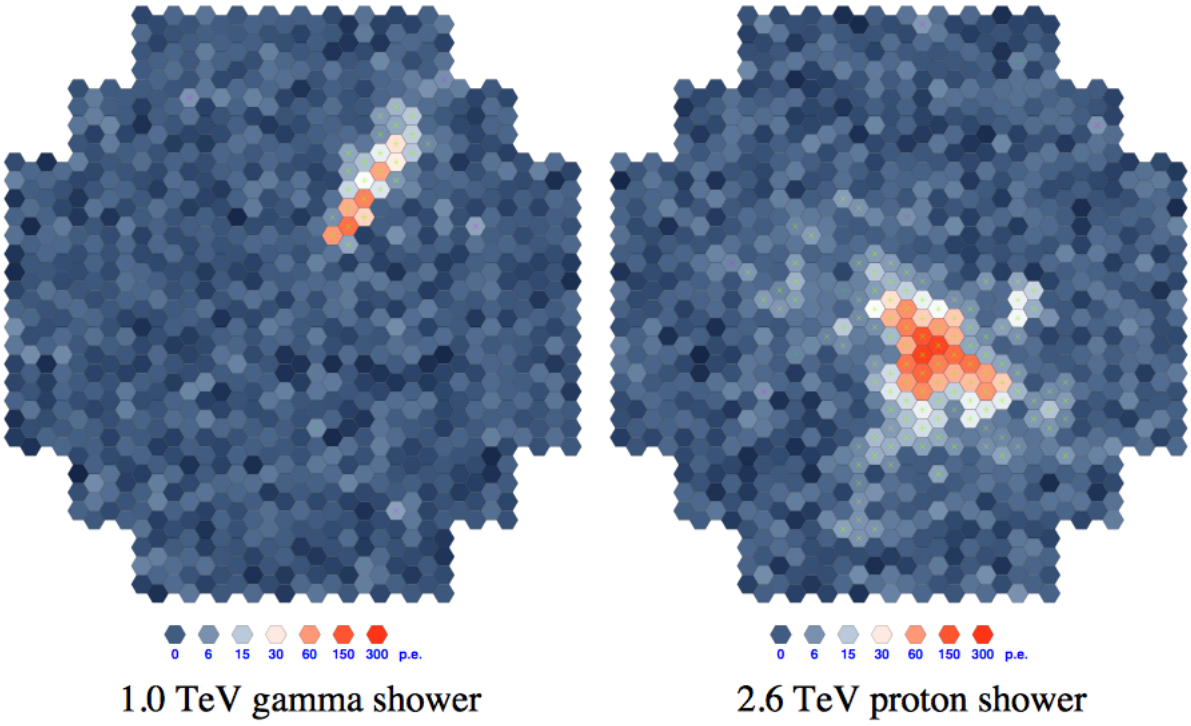

Figure 2.5: H.E.S.S. camera images for a simulated gamma-ray and proton shower. The gamma-ray shower image shows an ellipse-like shape, which is exploited in the event reconstruction technique. The proton image shows a much broader, irregular shape. Image taken from Völk & Bernlöhr (2009).

and the detector response have to be performed. The CORSIKA package, a Monte Carlo tool capable of simulating the air shower evolution for various particles, will be introduced in the next section. The simulation of the detector response will be explained in Section 2.4.2.

2.3 Simulation of Air Shower Events

The CORSIKA (Heck et al. 1998) program (Cosmic Ray Simulations for Kascade) is a FORTRAN-based package of routines to simulate air showers initiated by various particles in the atmosphere. It was originally developed for the KASCADE experiment, but is also widely used by the IACT community. CORSIKA is able to simulate air showers for 50 primary elementary particles, ranging from leptons ($e^{\pm}$, $\mu^{\pm}$, ...) and mesons ($\pi^{\pm}$, π^0, ...) to baryons (p, n, Λ, ...) and resonance states ($\rho^{\pm}$, ρ^0, ...). The arrival direction of the primary particle can be arbitrarily chosen, the local Earth's magnetic field at the observers position is taken into account. The atmosphere is modelled by five layers, in each layer the mass overburden follows a decreasing exponential dependence on the altitude. The Earth's curvature is not taken into account, this could lead to problems for quasi-horizontal arrival directions, but since only small zenith angles are allowed in this work this is a valid approximation.

Each particle in the shower above a configurable energy threshold is tracked individually. CORSIKA includes all known interaction processes, the biggest issues arise in the modelling of hadronic interactions. At high energies most secondary particles from hadronic interactions are produced with very low transverse momenta and therefore only few data exist from

	Set A	Set B
Corsika Version	6.990	7.410
Low-Energy Model	UrQMD 1.3	UrQMD 1.3
High Energy Model	QGSJETII-04	Sibyll 2.1

Table 2.1: Program versions used for the generation of proton simulation Set A and Set B.

Figure 2.6: Image of the full H.E.S.S. telescope array in the H.E.S.S. 2 phase with the four 12 m and the single 28 m telescopes (Credits: Frikkie van Greunen).

accelerator experiments. Therefore the modelling of hadronic interactions relies on the extrapolation of existing experimental data. In order to compare results from two different high energy models (energies > 80 GeV), two sets of simulations have been generated using the QGSJETII (Ostapchenko & Heck 2005) (Simulation Set A) as well as the Sibyll (Fletcher et al. 1994) (Simulation Set B) package. The exact versions of the packages used are summarized in Table 2.1. Electron and gamma-ray showers were generated with the CORSIKA version of set A only. Interactions of hadrons below an energy of 80 GeV are modelled using the UrQMD (Bleicher et al. 1999) package. In this energy range enough accelerator data exist and hadronic interactions can be modelled very well.

Since proton-induced air showers are the main background for IACT experiments, it is important to study the differences in the predicted shower observables by different hadronic interaction models. One of the main differences is, as for example pointed out by Parsons et al. (2011), the amount of energy that is transferred to the electromagnetic component. For this work the biggest uncertainty should be differences in the production rate of π^0 very early in the shower development since these showers lead to very gamma-ray-like images in the camera. The results of both hadronic interaction models used in this work will be compared to each other for both the electron spectrum and the anisotropy. The difference will be treated as a systematic uncertainty.

2.4 The H.E.S.S. Experiment

The H.E.S.S. Cherenkov telescope system is located in the southern hemisphere in the Khomas Highlands of Namibia at 1800 m above sea level (see Figure 2.6). It consists of five Cherenkov telescopes, of which four have a dish size of 12 m (CT1-4) and one a size of 28 m (CT5). The four small telescopes are arranged in a square with a side length of 120 m, which is a trade-off between a high probability for a stereoscopic event and a large base length. The large telescope was placed in the center of the square to lower the achievable energy threshold with its big photon collection area. The H.E.S.S. experiment was designed to cover the gamma-ray energy range between several tens of GeV and 100 TeV, the actual energy threshold changes with atmospheric conditions and detector system parameters. The four small telescopes (H.E.S.S. 1 phase) started stereoscopic operation in late 2003 and were officially inaugurated in 2004, the fifth telescope was added in 2012 (H.E.S.S. 2 phase). In late 2016 the cameras of the small telescopes were replaced, the scientific operation stopped for only a few months.

For this work only data from the H.E.S.S. 1 phase have been used, therefore the following description of the telescopes, calibration and analysis procedures is only valid for the 12 m telescopes. Only parts of the detector system and the software that are of interest for this work will be described, other system parts like the central trigger system will not be explained. For a detailed description of the H.E.S.S. detector system and the analysis procedures the reader is referred to Aharonian et al. (2006) for H.E.S.S. 1 and Holler et al. (2015b) for H.E.S.S. 2.

2.4.1 Telescope and Camera System

The 12 m H.E.S.S. reflectors are segmented into 328 round mirror facets of 60 cm diameter and follow a Davies-Cotton design with a focal length of 15 m. The mirrors consist of quartz-coated aluminized glass. The nominal reflectivity of the mirror system is $\sim 80\,\%$ and decreases with time due to mirror aging. This makes regular refurbishments necessary. For the alignment of the mirror system the orientation of each facet is adjustable by two motors. The total photon collection area is $\sim 100\,\mathrm{m}^2$ per telescope. The reflector is supported by a rotating steel frame that is alt-az mounted. The optical system is described in detail in Bernlöhr et al. (2003); Cornils et al. (2003). The cameras of the H.E.S.S. 1 telescopes (see Figure 2.7) consist of 960 8-stage PMTs and are designed for a field of view of $5\,^\circ$. Light guides on top of the PMTs, so-called "Winston cones", lead to a maximum light yield. Since the Cherenkov flashes only last for a few ns the readout electronics has to operate with GHz sampling. The readout buffer is 128 ns deep, the pulse integration window is 16 ns. In order to guarantee a good charge resolution for a wide photoelectron range the analog-to-digital (ADC) converter path is split into a high-gain and a low-gain path. The camera is run in a coincidence trigger mode with a threshold of five pixels exceeding a predefined signal limit in an 8x8 pixel sector. Details about the H.E.S.S. cameras are described in Punch & H.E.S.S. Collaboration (2001).

2.4.2 Detector Response Simulation

The H.E.S.S. detector response to incident Cherenkov photons from an air shower event can be modelled very precisely by the package *sim_telarray* introduced by Bernlöhr (2008).

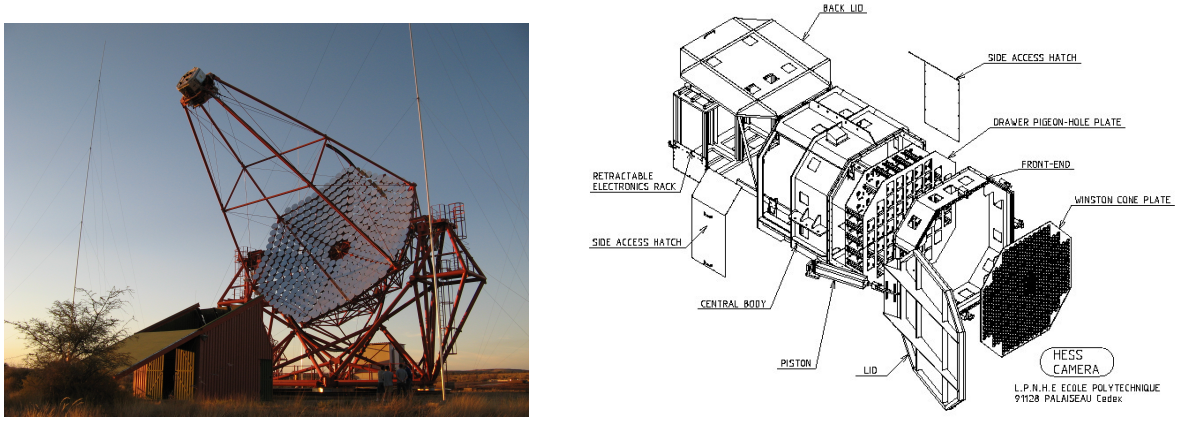

Figure 2.7: Image of one of the 12 m telescopes (*left*, Credits: Dalibor Nedbal) and an exploded view of its Cherenkov camera (*right*) taken from Punch & H.E.S.S. Collaboration (2001).

Sim_telarray was build to be a standalone back-end software for the CORSIKA shower simulation package. Since the shower simulation in CORSIKA is the most CPU-demanding part of the whole detector simulation chain a single shower event is processed several times by altering the relative position of the array with respect to the shower axis. The response to both point-like and diffuse emission for the whole camera field of view can be modelled. All known effects of the detector system and also external effects are included in the detector response simulation. The most important simulation steps are:

- Modelling of an average namibian atmosphere
- NSB with a nominal rate of 100 MHz for 100 % mirror reflectivity modelled as Poissonian noise on the pixel baseline
- Reflectivity of the mirror system taking into account imperfect mirror facets
- PMT characteristics like pulse shape and after-pulsing
- Simulation of the readout system

The output from *sim_telarray* is converted to a raw data format identical to the format of standard H.E.S.S. data. Therefore data of both origins can be treated the same during the calibration and analysis steps.

2.4.3 Raw Data Calibration

The data acquisition for the H.E.S.S. experiment is organized in runs of $\sim$ 28 minutes duration. The raw data of every run is calibrated for every telescope individually. The goal of the calibration of a H.E.S.S. telescope image is the determination of the pixel-wise number of photoelectrons that fits to the measured pixel signal. The calibration procedure that will be explained in the following section, can be separated in the following steps:

- Pixel-wise determination of the number of photoelectrons that corresponds to the measured ADC value (gain calibration)
- Telescope image cleaning

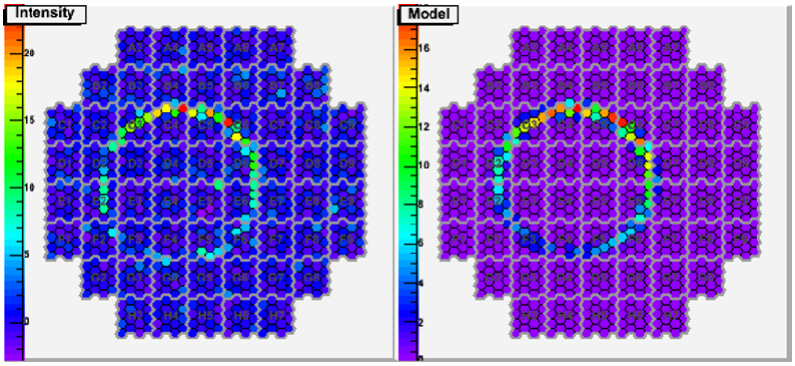

Figure 2.8: Measured (*left*) and simulated (*right*) image of a muon ring. The muon energy can be calculated with simple geometric observables and is used to extract the optical efficiency of the telescope. Image taken from Chalme-Calvet et al. (2014).

- Determination of the optical efficiency of the telescope

Two completely separated calibration chains exist for the H.E.S.S. experiment, the "H.E.S.S. Analysis Package" (HAP) and "Paris Analysis" (PA) both with their own set of calibration and analysis chains. For this work the HAP chain was used, all results were cross-checked with the PA chain. A detailed explanation of the H.E.S.S. calibration procedure can be found in Aharonian et al. (2004).

Gain Calibration and Image Cleaning

For every event the integrated pixel ADC value is measured in both low-gain and high-gain channel (ADC^{LG} and ADC^{HG}). The pixel amplitude in photoelectrons (A^{LG} and A^{HG}) is determined according to Equation 2.7.

$$\begin{aligned} A^{HG} &= \frac{ADC^{HG} - P^{HG}}{\gamma^{ADC}} \text{ x } FF \\ A^{LG} &= \frac{ADC^{LG} - P^{LG}}{\gamma^{ADC}} \text{ x } (HG/LG) \text{ x } FF \end{aligned} \tag{2.7}$$

Here P^{LG} and P^{HG} are the pedestal values, γ^{ADC} the gain factor for the high-gain channel, FF the flat-field coefficient and (HG/LG) the ratio of the gains of the low and high-gain channel, respectively. The high-gain channel is only used for $A^{HG} < 150$.

The image cleaning procedure is used to reject single pixel signals that are very likely induced by noise (NSB, electrical and PMT noise) and not part of a signal cluster. It requires a pixel to have either an amplitude above 10 and a neighbor pixel above 5 or to have an amplitude above 5 and a neighbor pixel above 10. This 5/10 cleaning is the standard H.E.S.S. cleaning level, any deviation to this cleaning level will be noted in the specific analysis chain introduction.

Determination of the Optical Efficiency

The next step after the determination of the pixel-wise number of photoelectrons for every telescope, is the determination of the optical effiency of the telescopes. Due to degradation

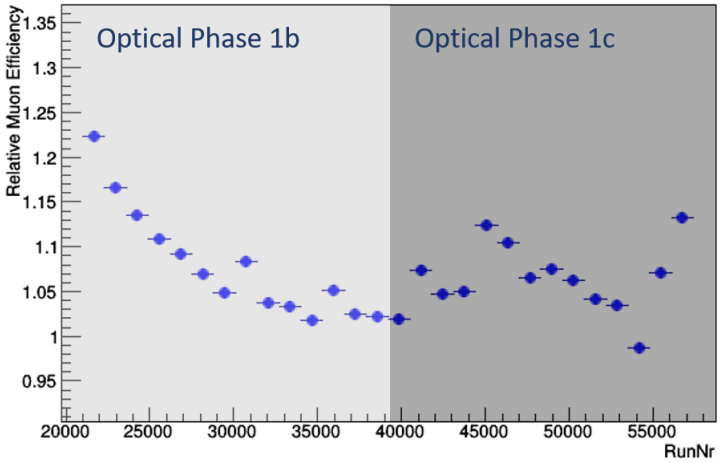

Figure 2.9: Optical efficiency correction factors for CT1 obtained by muon events for the data set used in this work. The data are split into two optical phases, the correction factors are given relative to the corresponding simulation set.

of the PMTs and changes in the reflectivity of the mirrors, the measured signals in the pixels change over time for a fixed particle energy. This effect is quantifiable with the help of muon events. These events are easily recognizable by their ring-like shape (see Figure 2.8) and their expected measured pixel signals can be calculated by simple geometric image parameters (see Chalme-Calvet et al. (2014) for details). Changes in the optical efficiency can therefore be tracked by comparing the expected and measured pixel signals of a muon image. The H.E.S.S. data is split into optical phases and a Monte Carlo simulation set of gamma rays (or electrons) is produced for every phase. An optical efficiency correction factor γ_{corr} relative to the Monte Carlo set of this phase is assigned to every run. The correction factors for the used data set for the example of CT1 are shown in Figure 2.9. A size correction of $< 15\,\%$ for the majority of the data set is usually regarded as acceptable.

The image parameter that is calibrated with respect to changing optical effiency are the summed-up pixel amplitudes of every telescope, the so-called "size-value". This value is later used to determine the energy of the triggered event. The measured *size*-value of every event in a run is telescope-wise converted to a corrected value *corr_size*:

$$corr\_size = \gamma_{corr} \cdot size \tag{2.8}$$

The individual pixel signals, that are for example used in the standard Hillas analysis discussed in Section 2.4.5, are not efficiency corrected. All reconstructed values besides the energy are instead compared to the mean values in the corresponding optical phase. The mean values are extracted by simulating Cherenkov shower events with CORSIKA and *sim_telarray* for every optical phase.

2.4.4 Standard Energy Reconstruction

In order to reconstruct the gamma-ray (or electron) energy of a shower image, the measured telescope size-values have to be connected to the primary particle energy. For this step energy lookup tables for every telescope and different reconstructed event directions are generated for simulated point sources at various offset angles to the camera center. These lookups only

Observation parameter	Simulated values
Source type	Electron point source
Source power law index	1.5
Energy Range	[0.01,100]TeV
Mirror reflectivity (CT1/CT2/CT3/CT4)	70/70/70/70 (Phase1b)
	60/54/60/60 (Phase1c)
Azimuth angle	0° and 180°
Zenith angle	0°, 10°, 20° and 30°
Offset angle to the camera center	0°, 0.5°, 1.0° and 1.5°

Table 2.2: Observational parameters used for the simulation and generation of the energy calibration lookups. The event energy is interpolated between the boundary lookups that match the event parameters best. The optical phase (1b,1c) is not used for interpolation, but the size value is corrected relative to the nominal mirror reflectivity.

depend on the measured size-value and the reconstructed distance to the telescope on the ground. The event energy is interpolated between the tables that match the reconstructed event parameters best. The optical phase is not used in the lookup interpolation routine since the size value is corrected relative to the nominal mirror reflectivity. The individual telescope energies are combined to an event energy by averaging over the telescope energies for all telescopes that participate in a shower event.

2.4.5 Standard Hillas-based Analysis

Most analysis and event reconstruction techniques for IACTs have been developed to determine the number of events coming from a gamma-ray point source. Point source is here defined as a source smaller than the instrument's point-spread function (PSF). Besides the directional reconstruction of the primary shower particle, the background-rejection power is the most important figure of merit for an analysis technique. In the following an event direction reconstruction technique will be introduced that most recent H.E.S.S. analysis techniques are based on (sometimes as seed value for a more advanced technique). Also the standard background-rejection method for a point source analysis will be introduced.

Image Parametrization and Directional Reconstruction

The standard IACT event reconstruction technique is based on the image parametrization by Hillas (1985). This technique utilizes the fact that telescope images of electromagnetic showers can be described very efficiently by ellipses. The image parameters are the width and length of the telescope shower ellipses, the distance between the shower center and the center of the camera and the orientation of the ellipse in the camera system. The shower images of all telescopes that participate in an event are combined in a joined camera coordinate system. In Figure 2.10 the Hillas parametrization is shown for the example of a stereoscopic event with two participating telescopes. The image source direction can be reconstructed by intersecting the elongated major axis of the individual telescope ellipses. In a similar way the impact position of the shower and the height of maximum shower intensity can be reconstructed. For events with more than two participating telescopes weighted averaging methods have to be introduced in order to prefer telescope images with the best quality. The most important image parameters are the width and the length of the ellipses since these parameters will be

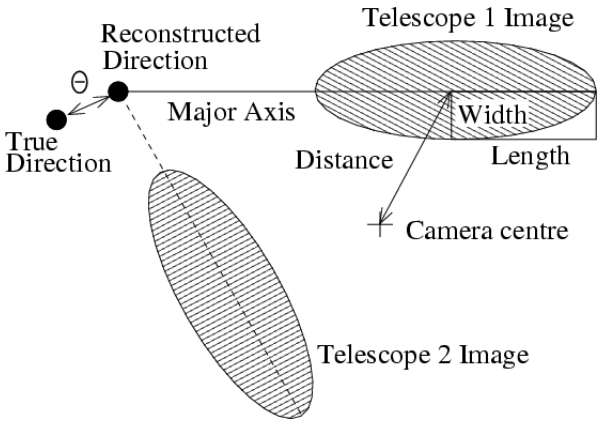

Figure 2.10: Illustration of the Hillas parametrization for a stereoscopic air shower event. The width and the length of the ellipses can be used to separate electromagnetic and hadronic showers. Image taken from Aharonian et al. (2006).

used by the background-rejection method.

Background Rejection

The measured width and length values ($width_i$ and $length_i$) for telescope i depend on many observational parameters like the zenith and azimuth angle. Therefore the measured values are compared to those expected on average from Monte Carlo simulations for a specific optical phase ($\langle width_i^{MC} \rangle$ and $\langle length_i^{MC} \rangle$), taking into account the parameter spread σ_i^{MC}. The average Monte Carlo width and length values are stored in lookups organized in the same way as the energy lookups defined in Table 2.2. The resulting parameters *Mean Scaled Width* ($MSCW$) and *Mean Scaled Length* ($MSCL$) are defined in Equations 2.9 and 2.10.

$$MSCW = \frac{1}{N_{tel}} \sum_{i=1}^{N_{tel}} \frac{width_i - \langle width_i^{MC} \rangle}{\sigma_i^{MC}} \tag{2.9}$$

$$MSCL = \frac{1}{N_{tel}} \sum_{i=1}^{N_{tel}} \frac{length_i - \langle length_i^{MC} \rangle}{\sigma_i^{MC}} \tag{2.10}$$

Since hadronic shower images are much more irregular and are also wider on average than electromagnetic shower images, an event selection cut on MSCW and MSCL alone gives a cosmic-ray background rejection of several magnitudes. However, this is usually not enough to achieve a reasonable Signal-to-Background (S/B) ratio.

In addition to the event selection cuts on MSCW and MSCL, the remaining background is determined from sky regions in the field of view where no gamma-ray source is expected. The number of background events is then subtracted from the measured event counts coming from the expected source direction. The size of these so-called "background regions" is chosen to be the same as the size of the "signal region" that is defined by a circular region around the expected source direction with the size of the PSF (for point source analyis). Usually more than one background region is used to achieve a better estimate of the background. In order to ensure that both signal and background regions see the same systematics with

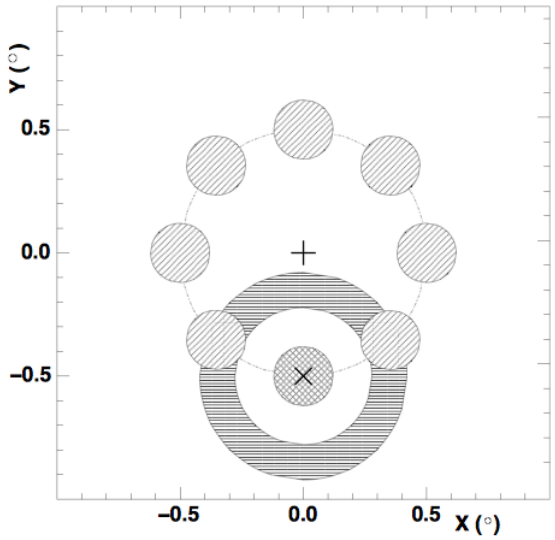

Figure 2.11: Illustration of the signal and background regions for a target position marked by an X. The actual pointing position (cross) is offset by 0.5 ° from the target position so that both signal and background regions have the same offset from the camera center. The signal region is marked by a cross hatched circle, background regions are filled by diagonal lines. Image taken from Aharonian et al. (2006).

respect to camera acceptance a ring with 0.5 ° radius around the camera center is defined and the regions are placed on them (see Figure 2.11). Point source observations are therefore always performed with a pointing offset of 0.5 ° to the expected source direction. The number of gamma-ray events N_γ is then defined as:

$$N_\gamma = N_{Sig} - \alpha N_{Bkg} \tag{2.11}$$

Here N_{Sig} are the number of counts in the signal region, N_{Bkg} the summed-up number of counts for all background regions and α the geometric normalization factor of the background regions. This analysis technique can also be used for slightly extended sources by increasing the size of signal and background region, but it is not suited for the analysis of diffuse emission across the whole field of view. Two analysis techniques specialized on the signal extraction of diffuse emission will be introduced in the next chapter.

CHAPTER 3

Cosmic-Ray Electron Analysis with H.E.S.S.

The requirements for a cosmic-ray electron analysis with IACTs differ vastly from those for a gamma-ray point source analysis. The most important difference is caused by the diffuse nature of cosmic-ray electrons. Since electrons are expected over the whole camera field of view, the usual background-rejection method introduced in Section 2.4.5 is not applicable. Two analysis chains are introduced in the following that are specialized on the extraction of cosmic-ray electrons and diffuse emission in general. The correct estimation and treatment of the background is the most crucial part of an electron analysis with IACTs. All possibly contributing sources of background will be introduced in Section 3.1. The data set and the data quality critera will be introduced in Section 3.2. The main analysis technique in this work represents an advanced version of the method used for the previous H.E.S.S. cosmic-ray electron publications and will be introduced in Section 3.3. An additional advanced IACT signal extraction method will be introduced in Section 3.4, this method will be only used for the determination of the cosmic-ray electron spectrum in Chapter 4. The determination technique of the effective areas and performance tests with respect to energy and directional reconstruction of both analysis chains will be discussed in Section 3.5 and 3.6 respectively.

3.1 Expected Sources of Background

Gamma-Ray Emission Regions

For both analysis chains used in this work cosmic-ray electrons and gamma-rays are indistinguishable and therefore contribute directly to the measured signal flux. The most problematic region in this sense is the galactic plane with its diffuse gamma-ray emission and huge collection of known sources. Galactic diffuse emission has been detected in the GeV regime by Fermi/LAT (Ackermann et al. 2012b) and by H.E.S.S. in the TeV regime (Abramowski et al. 2014) as part of the H.E.S.S. Galactic Plane Survey (Carrigan et al. 2013). According to the published H.E.S.S. data the diffuse emission extends roughly up to galactic latitudes of $|b| < 2^\circ$ for energies above 1 TeV. Similar to the analysis in previous H.E.S.S. cosmic-ray electron publications it was therefore decided to use a galactic latitude cut of $|b| > 7^\circ$ for the

observation position of a H.E.S.S. run. Additionally, known gamma-ray sources were excluded by rejecting signal events with a distance to a source $d < 0.4\,^{\circ}$. Since all known extragalactic gamma-ray sources are point-like, the value of this cut is motivated by roughly twice the size of the PSF (see Section 3.5).

Isotropic Diffuse Gamma-ray Background

Besides the known gamma-ray emission from the galactic plane and resolved gamma-ray sources, that are both easily rejected by the stated selection cuts, a bigger issue is the presence of the isotropic diffuse gamma-ray background (IGRB) in extragalactic field of views. Due to its diffuse nature it cannot be rejected and has to be accepted as part of the signal flux. The spectrum of the IGRB was both measured by EGRET (Strong et al. 2004) and Fermi/LAT (Ackermann et al. 2015), but only the Fermi/LAT measurements extend to high GeV energies with a maximum energy of 820 GeV. According to Ackermann et al. (2015) the IGRB spectrum is well described by a power law model with exponential cutoff energy E_{cut}:

$$\frac{dN}{dE} = I_{100} \left(\frac{E}{100\,\mathrm{MeV}} \right)^{-\gamma} \exp\left(\frac{-E}{E_{cut}} \right) \tag{3.1}$$

Depending on the used signal extraction method the derived best-fit values for the intensity at 100 MeV I_{100} and the spectral index γ vary, but can be approximated as $I_{100} \simeq 10^{-7}\,\mathrm{MeV^{-1}cm^{-2}s^{-1}sr^{-1}}$ and $\gamma \simeq 2.3$. The cut-off energy is determined to be $E_{cut} \simeq 230\,\mathrm{GeV}$. Adopting this model, the expected IGRB contamination at 400 GeV is less than 1 % and hence completely negligible in the TeV regime.

Cosmic-Ray Protons

The biggest challenge for the analysis in this work and for IACTs in general are cosmic-ray protons. Protons are the only component of cosmic rays that are able to produce gamma-ray-like air showers in a substantial amount. All other components are rejected very efficiently. The cosmic-ray proton spectrum measured for example by BESSII (Abe et al. 2016) or PAMELA (Adriani et al. 2011) shows a very stable spectral power law index $\simeq 2.7$ above 100 GeV/nucleon and a flux roughly 3 orders of magnitude higher than the cosmic-ray electron flux. Due to the harder index of the proton spectrum with respect to the electron spectrum, background rejection becomes more and more important with increasing energy. Since both signal and background are of diffuse nature, specific analysis techniques have to be developed that do not use any spatial information in contrast to the standard analysis described in Section 2.4.5. The different strategies (**ZetaBDT − Fit**, **ZetaBDT − Cut** and **ImPACT − MSSG**) will be introduced in Section 3.3 and 3.4, respectively. Additionally to these specific background-rejection strategies, only very high quality events are considered for reconstruction. The exact event selection cuts differ between the analysis chains and are stated in the respective sections in the following.

3.2 Data Set and Run Selection Cuts

The H.E.S.S. data quality classification scheme separates all possible factors that might affect the quality of a data run into two main categories: The quality of the atmosphere and the hardware. The most important hardware quality criteria are the number of broken pixels and

the participation fraction of a single telescope in shower events. A very low or high event participation fraction might indicate hardware problems of the respective telescope. The energy calibration algorithm is very vulnerable to a too high number of broken pixels, since the size value of the affected pixels is simply lost.

The tracking of the atmospheric conditions is very important for IACTs since it is a crucial part of the detector system. Atmospheric absorption variations, for example due to clouds or an increased aerosol content, lead to multiple effects on the observed shower signals. The most important effect is the change in measured photoelectrons for a fixed primary energy. Since this might also be caused by a change in the optical efficiency of the telescope system, a hardware independent number that quantifies the atmospheric absorption has to be defined and tracked for all runs. In the H.E.S.S. data quality monitoring scheme developed by Hahn et al. (2015) the so-called "transparency coefficient" (TC) introduced by Hahn et al. (2014) quantifies the atmospheric absorption. This value is only defined and further explained in the electron anisotropy chapters (Section 5.4) since for the energy spectrum it was only used as a run quality indicator. Using the TC value as a run selection criterion minimizes the impact of the atmospheric quality on the measured flux. The run quality criteria used in this work are summarized in Table 3.1. Additionally to these cuts the following run selection cuts were used:

- The mean zenith angle of each run must be $\leq 25\,^\circ$ to reduce systematics in the analysis
- Only extragalactic observations $\rightarrow \pm 7\,^\circ$ distance to the galactic plane
- Three (BDT) / Four (Impact-MSSG) operational telescopes of H.E.S.S. 1 phase
- Runs taken between May 2004 and April 2010 (optical efficiency phases 1b and 1c)
- The energy threshold is determined run-wise by imposing a maximum allowed energy bias of 3 % (see Section 3.5 for details)

The resulting number of runs and the dead-time corrected livetime at 1 TeV of both the BDT and ImPACT-MSSG analysis is shown in Table 3.2. The livetime is not a constant with respect to energy, because changes in the optical efficiencies and the mean zenith angle of a run shift the achievable energy threshold.

3.3 ZetaBDT Analysis Chain

The ZetaBDT analysis chain has been developed as an on-top analysis to the standard Hillas analysis and reconstruction technique. The standard energy calibration and Hillas reconstruction is performed, but instead of using cuts on the Hillas parameters, a more sophisticated machine-learning algorithm is used to separate signal from background. The idea of using multivariate analysis tools like random forests (RFs) or boosted decision trees (BDTs) for background rejection is neither new for the IACT community in general nor to the H.E.S.S. collaboration. It was already shown in 2009 by Ohm et al. (2009) that BDTs in combination with Hillas image parameters are superior to plain cuts on the Hillas parameters themselves with respect to the resulting S/B ratio. The H.E.S.S. cosmic-ray electron analysis in 2008 and 2009 used RFs which are very similar to BDTs. In the following, the BDT classification technique itself is introduced in Section 3.3.1, the actual implementation in the H.E.S.S.

Cut Criterion	Cut Range [Unit]
Quality of Atmosphere :	
Transparency Coefficient	0.8 - 1.2 [arb. units]
Trigger Rate Fluctuation	0 - 10 [% of mean value]
Trigger Rate Slope	-30 - 30 [% of mean value]
Hardware Quality :	
Run Duration	600:7200 [sec]
Tel. Participation Fraction	0:0.4 [rel. fraction]
Pixels with 'hardware' Flag	0:120 [number]
Pixels with 'HV-off' Flag	0:50 [number]
RMS of Az. Deviation Distr.	0:10 [arcsec]
RMS of Alt. Deviation Distr.	0:10 [arcsec]
Mean Deviation in RA	0:1 [arcmin]
Mean Deviation in Dec	0:1 [arcmin]

Table 3.1: Run selection criteria used for the quality classification of H.E.S.S. data runs. The specified quality criteria are associated with the highest quality class of observation runs and used for spectral analysis of gamma-ray sources.

	BDT Analysis	ImPACT-MSSG Analysis
Number Runs Phase1b	1188	589
Number Runs Phase1c	1773	1316
Corr. Livetime @ 1 TeV [h]	1253.4	805.2

Table 3.2: Number of runs in the data set for the two different analysis chains. The corresponding livetimes are corrected with respect to the trigger deadtime.

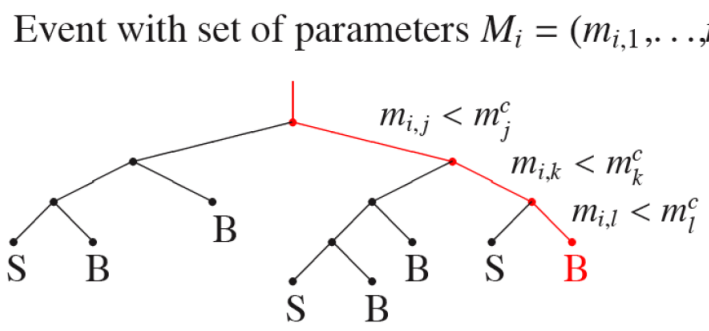

Figure 3.1: Decision tree with a *depth* = 3. Based on decisions made in the tree nodes the tested parameter realization ends either in a signal or background leaf. A BDT is built as a "forest" of these simple decision trees. Image taken from Ohm et al. (2009).

analysis chain is described in Section 3.3.2. The signal extraction and background estimation method is introduced in Section 3.3.3.

3.3.1 Boosted Decision Trees

A BDT algorithm is a machine learning technique capable of separating signal from background events based on a set of image parameters M. The layout of a BDT classifier consists out of a number of so-called "decision trees" (see Figure 3.1). Each tree judges if a given realization m_i of the parameter set M is signal or background-like based on decisions made in the "nodes" of the tree. Based on the decisions taken, each event takes a certain route through a tree and ends in a "leaf' associated with either signal or background. The depth of the tree is for most implementations chosen to be smaller than the total number of available image parameters, so not all trees test all image parameters. A decision tree is therefore nothing else than a set of cuts capable of separating signal from background.

The power of a collection of decision trees (a so-called "forest") lies in the fact that a single decision tree might make the wrong decision, but the majority vote of the whole forest will be much less prone to that. In a simple "Random Forest" the decision trees are trained independently from each other with a set of parameter realizations for which the answer (signal/background) is known. For a random pick of N image parameters the set of cuts in the nodes are optimized until the best separation efficiency is reached. The disadvantage of a simple random forest classifier lies in the fact that small systematic deviations from the training to the actual data can lead to wrong decisions.

This issue is minimized with the "boosting"-technique. The training phase is partitioned in sequential training stages. In each training stage only one decision tree is trained. After the training of the decision tree T_l in stage l the voting weight $\alpha_l = \log\left[\left(1 - err_l\right)/err_l\right]$ is determined with the fraction of misclassified events err_l. For the next training stage the weights of the misclassified events are multiplied by e^{α_l} so that the training in the next stage focuses on the misclassified events. The final decision T is determined by averaging over the

Event Selection Cut	Allowed Range
Multiplicity	≥ 3
Telescope Local Distance	$\leq 0.525\,\mathrm{m}$
Telescope Size Value	$\geq 60\,\mathrm{p.e.}$
Core Distance	$\leq 200\,\mathrm{m}$
Offset	$\leq 1.5\,^{\circ}$
Energy	$\leq 40\,\mathrm{TeV}$

Table 3.3: Event selection cuts for the ZetaBDT analysis.

weighted decisions T_l (+1/-1 for signal/background) from the individual trees:

$$T = \sum_{l}^{l \leq N_{Tree}} \alpha_l T_l \tag{3.2}$$

The raw decision value T is further processed into a continuous signal likeliness parameter between -1 (background) and +1 (signal) that can be used for signal/background separation.

3.3.2 BDT-based Electron Analysis

The BDT implementation in this work utilizes the latest version 4.2.0 of the TMVA package (Hoecker et al. 2007) for the ROOT software. This package offers easy-to-use implementations of multivariate analysis techniques like neuronal networks, random forests and boosted decision trees. The structure of the BDT analysis chain is based on the original implementation by Ohm et al. (2009). The TMVA BDT implementation has a wide range of control parameters like the number of decision trees in the forest or the depth of each single tree. The configuration and layout of the BDT used for the electron analysis is summarized in Appendix A.1.

The BDT was trained with Monte Carlo simulations of diffuse electrons as signal and diffuse protons as background (see Appendix A.1 for more details). The four separation parameters used by the decision trees are a combination of Hillas-based image parameters (MSCW and MSCL of Section 2.4.5) and reconstructed event parameters ($\frac{\Delta E}{E}$ and X_{max}). $\frac{\Delta E}{E}$ is given by the uncertainty of the reconstructed event energy, estimated from the differences between the participating telescopes and X_{max} is the reconstructed height of maximum shower intensity. All separation parameters show a strong energy dependence. It was therefore decided to train the BDT in energy bands similar to the original implementation by Ohm et al. (2009). In order to guarantee a very high quality of the telescope images and the reconstructed values, stringent event selection cuts, specified in Table 3.3, were applied. Only events with a stereoscopic multiplicity of more than two participating telescopes were allowed. The "Telescope Local Distance" restricts the position of the center of gravity of the ellipses to a circle with radius 0.525 m within the camera. The motivation of this cut is to reject truncated shower images. The cut on the distance of the shower core to the center of the array (core distance) is the most important quality cut since showers that are very close to the array center are reconstructed better than those far away. This cut is also an efficient proton-rejection cut.

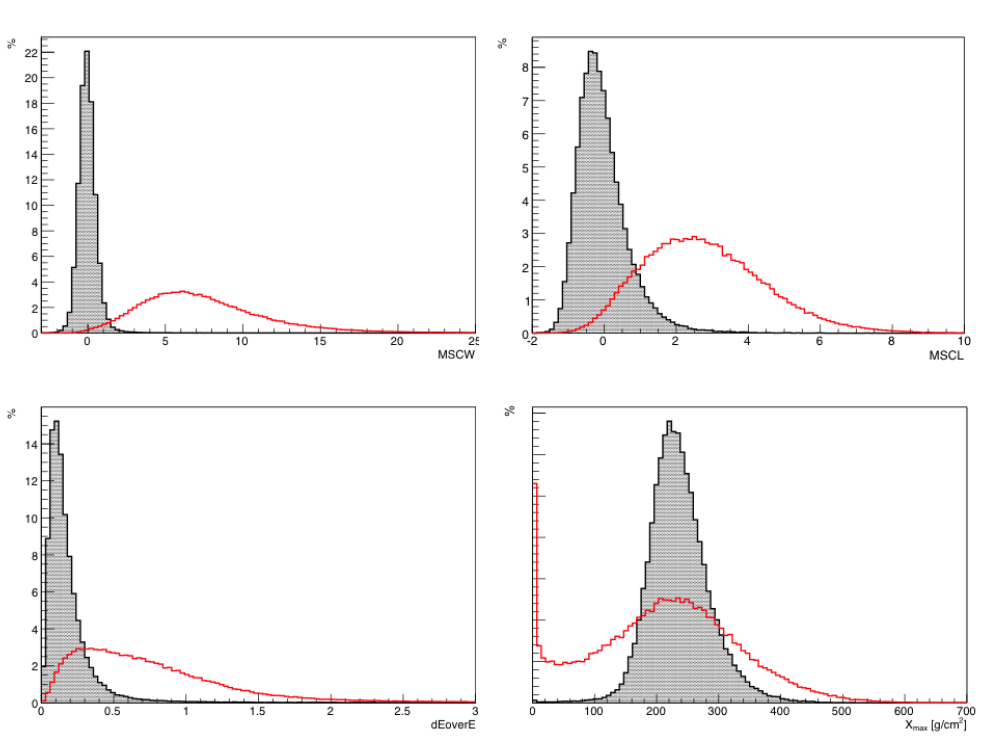

Figure 3.2: Event separation parameters used for the cosmic-ray electron BDT implementation in the training energy band from 500 to 600 GeV. Signal events (electrons) are shown in grey, background events (protons) in red. The BDT was trained with diffuse Monte Carlo simulations of both species.

Protons show in general a systematically higher reconstructed core distance than gamma rays or electrons. The cut on the offset of the shower direction to the pointing direction and the upper bound of the reconstructed energies were introduced to reduce the systematics in the analysis.

Figure 3.2 shows the event separation parameters for the energy training band from 500 GeV to 600 GeV with the event selection cuts applied. All parameters show signal/background separation power with only a small linear correlation at the same time (see Figure 3.3 right). BDTs are in general rather vulnerable to linear correlations, decorrelation techniques are available in TMVA, but have to be used with care according to user experiences. It was therefore decided to stick with the small, uncorrelated set of four parameters. The same parameter combination was used for the cosmic-ray electron analysis by VERITAS (Staszak 2015). Figure 3.3 shows the resulting BDT score distribution for a collection of simulated particles. Heavy nuclei are rejected very efficiently. The rise in the proton distribution for signal-like BDT scores shows the fraction of proton showers that transfer a large fraction of the primary particle energy into π_0s very early in the shower development. These showers cannot be sorted out by the BDT.

The raw BDT score itself is not suited as a cut parameter since the resulting cut efficiency would show a strong energy dependence due to the training in energy bands. The separation for energies > 1 TeV is much more efficient than for low energies, a hard cut for low energies would reject an unnecessary high fraction of high energy events. The BDT implementation by Ohm et al. (2009) circumvents this issue by defining an energy-dependent $\zeta_{BDT}(E)$ parameter defined as the gamma-ray cut efficiency for signal events at energy E. This allows

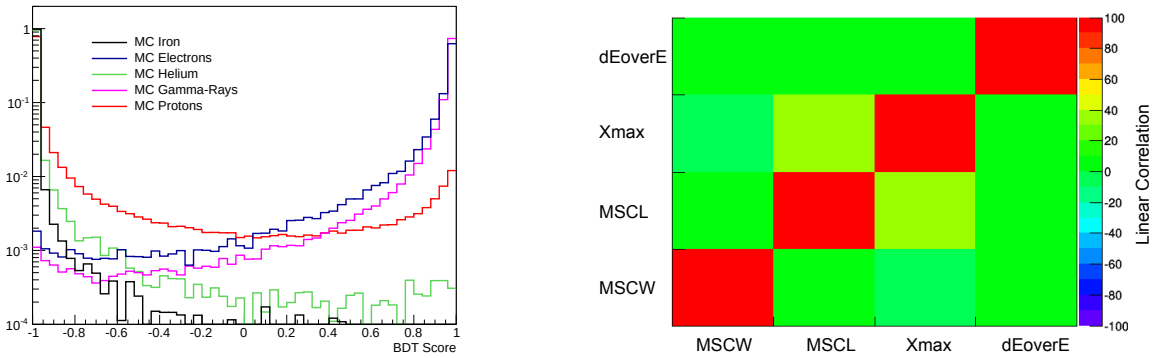

Figure 3.3: *Left* : Raw BDT score for various simulated particle species. The main background in the signal region is given by gamma rays and protons. *Right* : Linear correlations between the BDT separation parameters.

one to define an energy independent cut. Since cut values of ζ_{BDT} are usually chosen to be smaller than one, a fixed fraction of signal events is rejected even in the case of a perfect signal/background separation. For this reason a different definition of ζ_{BDT} was used for the electron analysis:

$$\zeta_{BDT}(E) = 1 - Eff_P(BDT, E) \tag{3.3}$$

Here Eff_P is the cut efficiency for simulated protons. In Figure 3.4 the proton efficiency for different energy bands is shown. A very useful side effect of the definition of ζ_{BDT} is the fact that the proton background should be flat in this variable and the electron signal should show itself as a peak towards +1 on top of the background.

Two different analysis strategies with different BDT cut values (see Table 3.4) were defined:

- A strategy using a soft ζ_{BDT} cut (ZetaBDT-Fit) for the energy spectrum in Chapter 4 and the anisotropy study in Chapter 6. For this strategy the remaining proton background is directly estimated and subtracted using the BDT template fit technique discussed in Section 3.3.3. As a result, this analysis strategy should get rid of all background in the case that the hadronic interaction models used to simulate protons resemble the reality reasonably well.

- A strategy using a hard ζ_{BDT} cut (ZetaBDT-Cut) for the anisotropy study in Chapter 5. Also for this strategy the remaining proton background is estimated using the BDT template fit technique discussed in Section 3.3.3. In difference to the other BDT strategy, this time the proton background is accepted as part of the signal.

The resulting proton contamination for both strategies will not be discussed here, but in the corresponding chapters. The performance with respect to effective areas, energy and direction reconstruction will be analyzed together with the ImPACT-MSSG analysis chain in Section 3.5 and 3.6.

3.3.3 BDT Template Fit Technique

The RF algorithm used for event classification in the 2008 and 2009 cosmic-ray electron analysis showed that the proton contamination for a Hillas-based multivariate analysis is

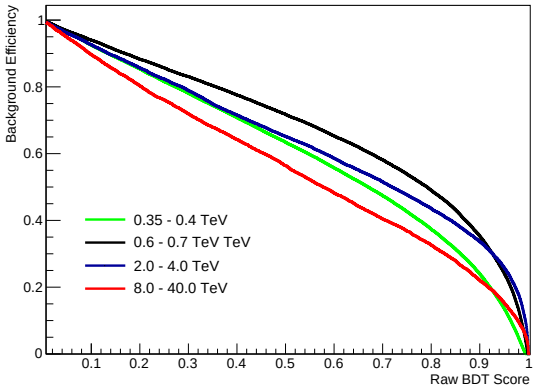

Figure 3.4: Monte Carlo proton cut efficiencies for several energy bands. These efficiencies were used to define an energy independent cut variable ζ_{BDT} based on the raw BDT event score.

Cut-set	ζ_{BDT} cut
ZetaBDT-Fit	0.79
ZetaBDT-Cut	0.95

Table 3.4: ζ_{BDT} cut values for the signal-background separation with the BDT analysis.

roughly at a level of 30 - 50 %. This level is of course too high for the background to be ignored in the extraction of the energy spectrum (but not for an anisotropy analysis, as will be shown in later chapters). The level of background therefore has to be estimated and subtracted. The background estimation does not happen with the help of off-regions in the FoV, but with the help of templates in the ζ_{BDT} space obtained from simulations. If the shape of the BDT distribution of both electrons and protons is known, both templates can be fit to the classified data set. Two conditions have to be met in order for this method to work:

- The background has to consist solely out of protons in the signal-like ζ_{BDT} regime. Figure 3.3 illustrates that this is the case. Gamma-ray events from known sources are rejected by the applied event selection cuts specified in Section 3.2.
- The protons in the data need to be described well enough by the hadronic interaction models. It is not known if this is the case, therefore two sets of interaction models have been used and compared to each other (Proton Set A and B) .

Simulating enough protons for the signal-like ζ_{BDT} regime is very demanding with respect to computation time. The simulation set described in Table 3.5 has been simulated on two serial throughput clusters and on clusters from the European Grid Infrastructure, using in total $\sim 450\,\mathrm{CPU} - \mathrm{Years}$. Electron simulations were carried out for multiple zenith angles due to a very large dependence of the ζ_{BDT} distribution on this parameter. For protons the distribution proved to be stable with respect to the zenith angle, therefore only one set at 20° was simulated. For the fitting procedure the zenith angle, azimuth angle and optical phase distribution of the data was reproduced by the simulated templates. Since the simulations were performed with a spectral index of 1.5/2.0 the ζ_{BDT} distributions had to be re-weighted

	MC Electrons	MC Proton Set A	MC Proton Set B
Source type	diffuse emission	diffuse emission	diffuse emission
Spectral index	1.5	1.5	2.0
Optical Phases	1b,1c	1b,1c	1b,1c
Zenith angles	0°, 10° , 20° , 30°	20°	20°
Azimuth angles	0°, 180°	0°, 180°	180°
No. sim. events	4.2e6	1.2e10	1.6e10

Table 3.5: Specifications of the simulation data set used for the generation of the ζ_{BDT} templates.

event-wise with the factor $(E_{true}/0.2\,\mathrm{TeV})^{1.5-2.7}$ for proton set A, $(E_{true}/0.2\,\mathrm{TeV})^{2.0-2.7}$ for proton set B and $(E_{true}/0.2\,\mathrm{TeV})^{1.5-3.0}$ for electrons. E_{true} is the energy of the simulated primary particle.

By fitting the electron and proton template to the classified data, a model m_i for the data counts d_i is determined for every ζ_{BDT} bin i. The model is given by:

$$m_i = r \cdot e_i + s \cdot p_i$$

Here e_i and p_i are the number of electron and proton template counts respectively. The two parameters to be found are the scaling factors r and s of the electron and proton template respectively. The fit is performed in the ζ_{BDT} range between 0.79 and 1 (as defined in Table 3.4 for the ZetaBDT-Fit analysis). The goodness-of-fit is evaluated with the χ^2 function defined in Equation 3.4.

$$\chi^2 = \sum_{i}^{i \leq N_{Bins}} \frac{(d_i - m_i)^2}{d_i + \sigma_m^2} \tag{3.4}$$

The model uncertainty σ_m^2 is determined by the fit routine. The MINUIT (James & Roos 1975) package is used for the fit. Since the parameters r and s are correlated the MINOS algorithm as part of the MINUIT package is used for the correct uncertainty determination. By rescaling the electron template with r and summing over all bins in the ζ_{BDT} cut range the number of electrons in the data set in a particular energy band N_{El} can be determined. The determined uncertainty $\Delta r/r \cdot N_{El}$ is used as statistical uncertainty, upper and lower uncertainties are treated individually.

In order to test the template fit method it was used on the known gamma-ray source PKS2155-304. Only PKS2155 runs that are part of the electron analysis data set were used, including the exceptional flare in July 2006 (Lenain et al. 2008). A circular signal region with a radius of 0.1 ° around the AGN was defined. The fitting procedure was performed in several energy bands. In Figure 3.5 example fits are shown for a low energy band and a high energy band. In both cases the fitted templates match the data distribution very well. As expected the ζ_{BDT} distribution of the protons is flat. However the level of contamination for the electron analysis will be much higher than for this strong gamma-ray source.

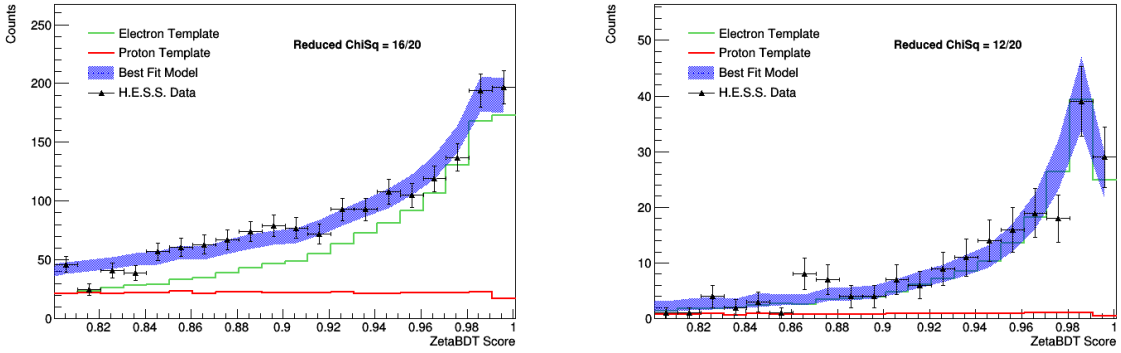

Figure 3.5: ζ_{BDT} template fits for events coming from a ring of 0.1 ° radius around the direction of PKS2155-304. *Left* : Energy band 0.3 to 0.4 TeV *Right* : Energy band 1.3 to 1.4 TeV.

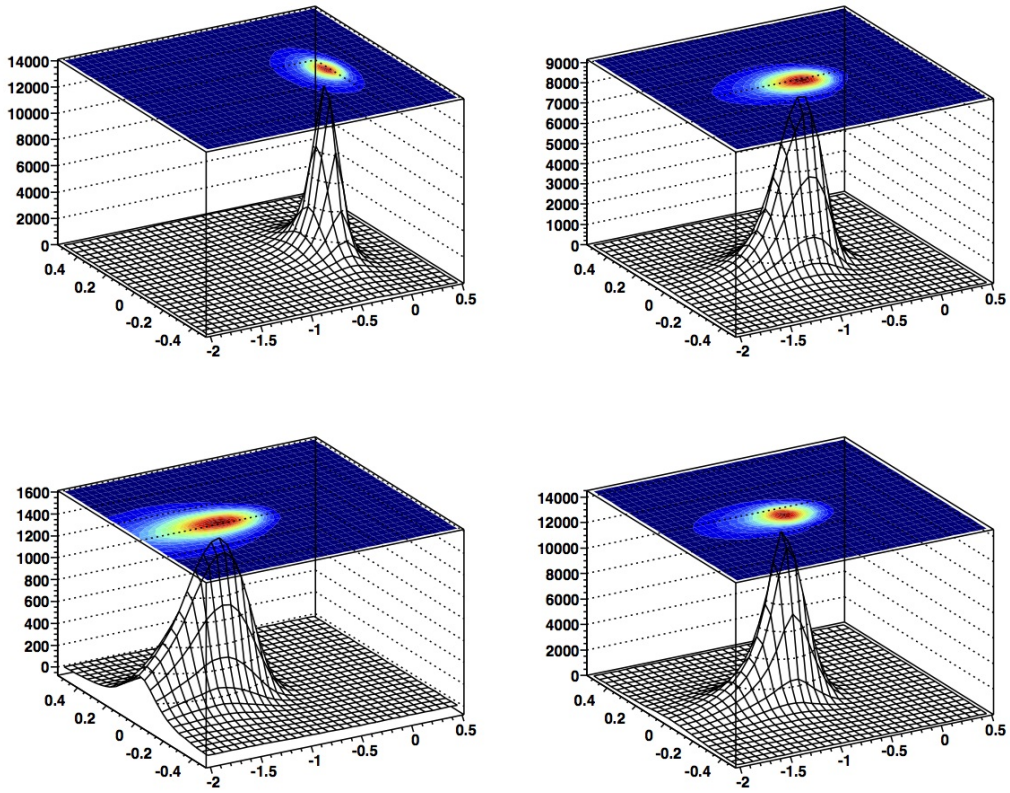

Figure 3.6: Camera image templates for a primary gamma-ray with an energy of 1 TeV at simulated core distances of 20 m (*top left*), 10 m (*top right*) and 200 m (*bottom left*) and with a shower maximum of 300 gcm^2. Additionally a template at 100 m core distance and X_{max} of 400 gcm^2 is shown in the bottom right plot. The x and y axis are camera coordinates in degrees, the z axis is given by the intensity. Image taken from Parsons & Hinton (2014).

Event Selection Cut	Allowed Range
Multiplicity	4
Telescope Local Distance	$\leq 0.525\,\mathrm{m}$
Telescope Size Value	$\geq 80\,\mathrm{p.e.}$
Core Distance	$\leq 150\,\mathrm{m}$
Offset	$\leq 1.5\,^{\circ}$
Energy	$\leq 40\,\mathrm{TeV}$
MSCW	[-2,0.9]
MSCL	[-2,2]

Table 3.6: Event selection cuts for the ImPACT-MSSG analysis.

3.4 Advanced ImPACT-MSSG Analysis Chain

The "Image Pixel-wise fit for Atmospheric Cherenkov Telescopes" (ImPACT) analysis chain for the HAP analysis package has been developed by Parsons & Hinton (2014) as an advanced event reconstruction technique. The ImPACT-MSSG analysis is based on the ImPACT analysis chain and was specifically developed to be comparable to the Model++ analysis (Holler et al. 2015a) from the PA chain in order to cross-check the results for the cosmic-ray electron spectrum. It will be shown in the next chapters that the ImPACT-MSSG analysis achieves a much better angular resolution and especially an increased proton-rejection power with respect to the BDT analysis. The event selection cuts for the ImPACT-MSSG analysis use the same cut parameters, but are in general more strict (see Table 3.6). The use of harder cuts is justified for this analysis, since with ImPACT-MSSG it was tried to achieve an as-low-as-possible proton contamination, without taking care about the electron cut efficiency. The energy threshold is higher with respect to the BDT analysis due to the slightly increased telescope size cut. The ImPACT-MSSG uses a less stringent 4/7 image cleaning level. The philosophy of the ImPACT-MSSG analysis is to suppress the proton contamination as much as posssible and accept the remaining background as part of the signal. This strategy is very similar to the ZetaBDT-Cut approach, however the residual background cannot be estimated directly with the help of classified data since no template fit method is applied. It has to be instead extracted with the help of simulated electrons and protons.

3.4.1 ImPACT Analysis

The main idea of the ImPACT analysis technique is to not reduce telescope shower images to image parameters like width and length but to compare recorded shower images to template images extracted from Monte Carlo simulations. These template images are generated with CORSIKA $+sim\_telarray$ simulations of gamma-ray events for different event parameters like offset and core distance (see Figure 3.6). The use of Monte Carlo simulations is the main difference to the Model++ analysis, which uses a semi-analytical model to generate the image templates.

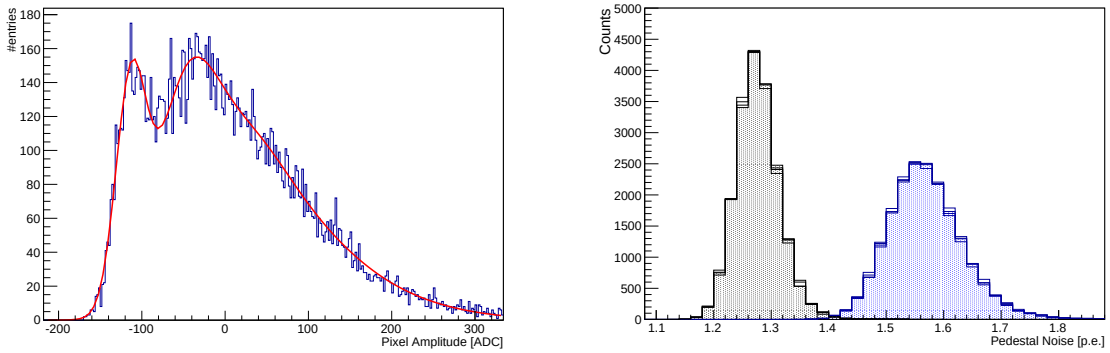

Figure 3.7: *Left* : ADC value distribution for a single PMT. The two visible peaks are the pedestal and the smeared out single-photoelectron peaks. The red fit curve is used to extract the width of the single-photoelectron peak. The single-photoelectron width has been extracted for all pixels individually. *Right* : Low-gain (black) and high-gain (blue) pedestal noise distributions for CT1-4. The noise and single-photoelectron values shown were extracted from Monte Carlo electron shower simulations for the optical phase 1b.

The core principle of the ImPACT analysis is to find the set of event parameters for which the template image fits best the recorded image of each single telescope. Event parameters to be found are the direction, impact distance, X_{max} and primary energy. In principle ImPACT is therefore an independent analysis chain with respect to the standard energy calibration and Hillas analysis. A disadvantage of the use of an ImPACT analysis for the cosmic-ray electron analysis is that the reconstructed primary energy is that of a gamma-ray since no electron templates exist. Therefore the reconstructed energy of the standard energy calibration is used. The other reconstructed parameters are not affected by the use of gamma-ray templates.

The likelihood function for the pixel-wise comparison between template and recorded image is given by Equation 3.5.

$$P(s|\mu,\sigma_p,\sigma_\gamma) = \sum_n \frac{\mu^n e^{-\mu}}{n!\sqrt{2\pi(\sigma_p^2+n\sigma_\gamma^2)}} \cdot \exp\left(-\frac{(s-n)^2}{2(\sigma_p^2+n\sigma_\gamma^2)}\right) \tag{3.5}$$

The likelihood $P(s|\mu,\sigma_p,\sigma_\gamma)$ for a single PMT and a measured signal s is given by the product of a Poisson distribution with n counts and expected signal μ and a Gaussian distribution of n centered at s, summed over all possible n. σ_p and σ_γ are the pedestal noise and the width of the single photoelectron peak respectively. In the original implementation of ImPACT the noise terms were approximated as constant for all pixels. One of the improvements of the ImPACT-MSSG was to extract the pixel-wise noise from Monte Carlo simulations for both high and low-gain channel, see Figure 3.7 for examples. The pixel log-likelihood value is then defined as:

$$\ln L = -2\ln P(s|\mu,\sigma_p,\sigma_\gamma) \tag{3.6}$$

By summing up the individual contributions of all pixels for all participating telescopes the log-likelihood value can be minimized with respect to the event parameters. In order to avoid local minima the event parameters reconstructed with the standard energy calibration and Hillas analysis are used as seed values. The minimization is performed using the MINUIT (James & Roos 1975) package. The minimization algorithm leads to an increased computation time per event with respect to the plain Hillas-based analysis. In order to minimize

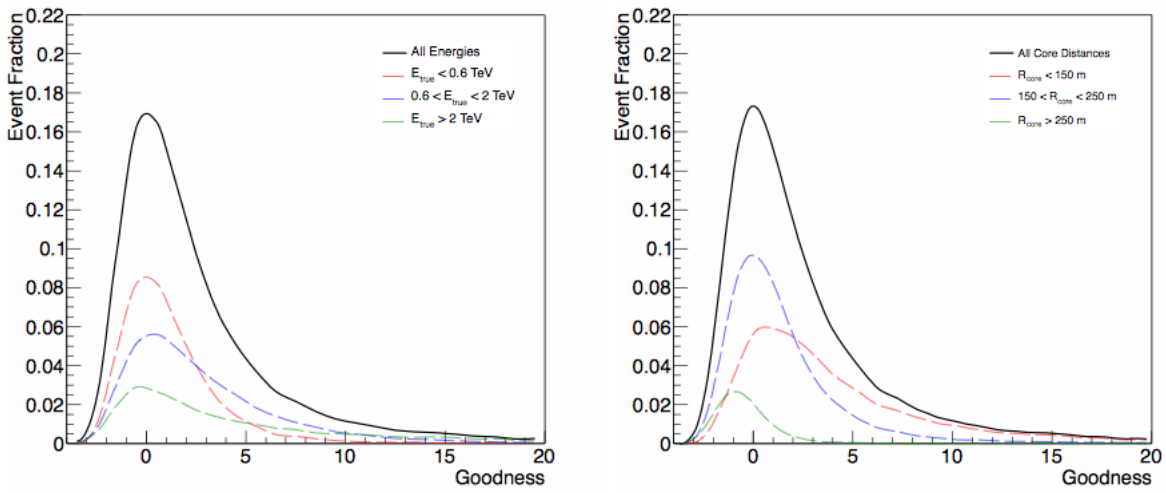

Figure 3.8: Goodness-of-fit distributions for gamma-ray Monte Carlo simulations. The simulated events have been split in energy (*left*) and core distance (*right*) bins to illustrate the dependence of the goodness-of-fit on these event parameters. The goodness-of-fit itself is therefore no suitable cut parameter (Parsons & Hinton 2014).

the computational effort, a preselection cut on MSCW and MSCL after the Hillas analysis is performed, see Table 3.6 for details.

In order to quantify the match between the best-fit template and the recorded telescope images the goodness-of-fit G is defined in Equation 3.7. Since the templates were generated with gamma-ray simulations, shower images of hadronic events will systematically fit worse to the templates. In contrast to the BDT analysis presented in Section 3.3 the whole image information is used.

$$G = \frac{\sum_i \left[\ln L(s_i|\mu_i) - \langle \ln L \rangle \,|_\mu\right]}{\sqrt{2 \text{ x } NdF}} \tag{3.7}$$

The pixel likelihood values are compared to the average likelihood value $\langle \ln L \rangle \,|_\mu$ for an expected signal μ. The number of degrees of freedom NdF is given by the number of participating pixels minus the dimension of the reconstructed parameter set. The goodness-of-fit G is defined in such way that it should be Gaussian with mean 0 for independent pixels, however it can be seen in Figure 3.8 that this is clearly not the case. There are systematical shifts of the mean with respect to energy and core distance and also a large tail towards high goodness-of-fit values. The goodness-of-fit itself is therefore not suited to be a background-rejection cut parameter as it would depend on the event parameters themselves. It will be shown in the next chapter that a reasonable scaling of the goodness-of-fit value leads to a very powerful background-rejection parameter.

3.4.2 Shower Goodness Scaling

The goodness-of-fit depends on event parameters like zenith and azimuth angle, offset angle, primary energy, core distance and optical phase. In this work all these dependencies were covered with a brute-force rescaling of the goodness-of-fit to a "Mean Scaled Shower Goodness" (MSSG). The rescaled goodness-of-fit $\text{MSSG}_{Phase\ x}$ for a specific optical phase x is defined in

Observation parameter	Simulated values
Source type	Diffuse electrons
Source power law index	1.5
Energy Range	[0.01,100]TeV
Mirror reflectivity (CT1/CT2/CT3/CT4)	70/70/70/70 (Phase1b)
	60/54/60/60 (Phase1c)
Azimuth angle	0° and 180°
Zenith angle	0°, 10°, 20° and 30°
Offset angle	$[0.0°, 0.7°]$, $[0.7°, 1.3°]$ and $[1.3°, 1.7°]$

Table 3.7: Observational parameters used for the simulation and generation of the goodness-of-fit scaling lookups.

Equation 3.8. This rescaling is identical to the one used in the Model++ analysis developed by Holler et al. (2015a).

$$\mathrm{MSSG}_{Phase\ x} = \frac{1}{\sqrt{N_{Tel}}} \sum_{i}^{i \leq N_{Tel}} \frac{G_i - \langle G \rangle_{i,Phase\ x}}{\sigma_{G,i,Phase\ x}} \tag{3.8}$$

N_{Tel} is given by the number of participating telescopes, G_i is the measured goodness-of-fit for a single telescope i and $\langle G \rangle_{i,Phase\ x}$ the average goodness-of-fit for the reconstructed event parameters over all telescopes. The error term $\sigma_{G,i,Phase\ x}$ is given by the uncertainty in the determination of $\langle G \rangle_{i,Phase\ x}$. The values for $\langle G \rangle_{i,Phase\ x}$ and $\sigma_{G,i,Phase\ x}$ are extracted from lookups that were produced for simulated electrons. An example lookup table for $\langle G \rangle_{i,Phase\ x}$ is shown in Figure 3.9 together with a slice of it at a fixed impact distance.The lookup layout with respect to the binning in event parameters is shown in Table 3.7. It is very similar to the one used for the standard energy calibration only that it has been generated with diffuse electron simulations and not with a point-like source. The lookup tables depend on the size value and impact distance of the telescope. The size value dependence covers the energy dependence of the goodness-of-fit.

In difference to the energy calibration lookup scheme the MSSG value is not determined for a fixed optical phase, but is interpolated between the simulation sets of the boundary optical phases using the run-wise optical efficiency determined with muon events. Since only simulations for 60 % and $\sim$ 70 % optical efficiency were generated for diffuse electrons this reduces the available data with respect to the BDT analysis. Details about the data sets for both analysis chains are summarized in Section 3.2.

The distribution of the resulting MSSG value is stable with respect to changing reconstructed event parameters. Of particular importance is the stability with respect to the energy shown in Figure 3.10, since cut efficiencies for the MSSG value should be energy independent. Like in the case of the BDT analysis the MSSG distribution of events coming from the signal region of PKS2155-304 was compared to Monte Carlo simulations of electrons and protons. The distribution in Figure 3.10 shows that the gamma rays from PKS2155-304 are correctly classified as electron-like events. Deviations between simulation and data could be due to the fact that gamma rays and electrons show slightly different MSSG distributions, or due to a

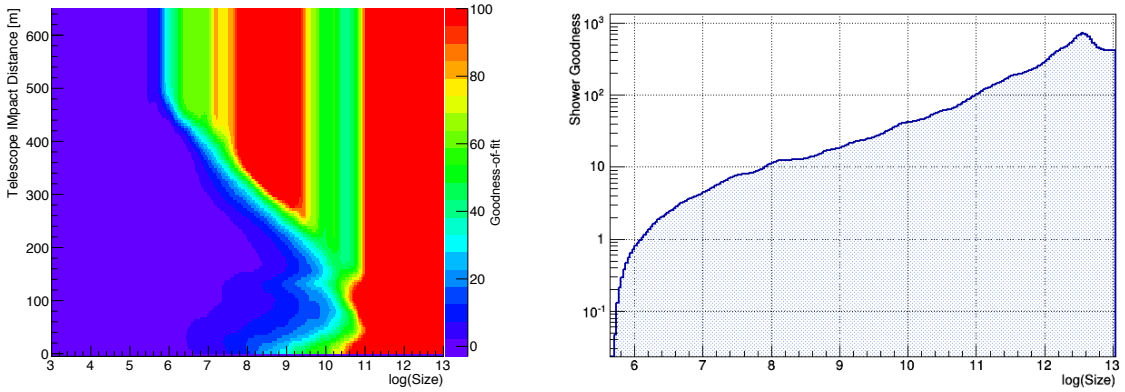

Figure 3.9: Goodness-of-fit scaling lookups for one specific zenith+azimuth+offset+phase combination (*left*) and a slice of it for a fixed impact distance of 200 m (*right*). The mean goodness-of-fit for specific event parameters is extracted by interpolating all dimensions. The biggest trend of the goodness-of-fit is that due to increasing size (energy).

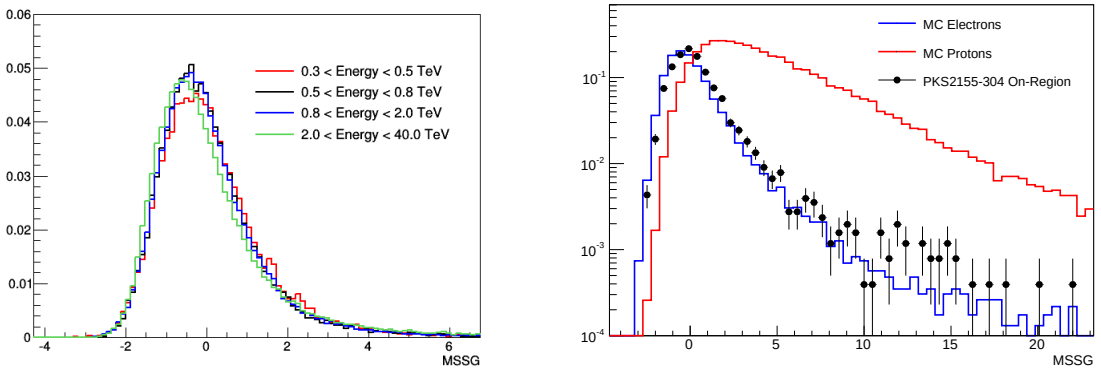

Figure 3.10: *Left* : MSSG distribution of simulated electrons split in several energy bands. *Right* : MSSG distribution of events coming from a ring of 0.1 ° radius around the direction of PKS2155-304 for energies between 0.4 and 40 TeV. The signal MSSG distribution is compared to the MSSG distribution of simulated electrons (blue) and protons (red).

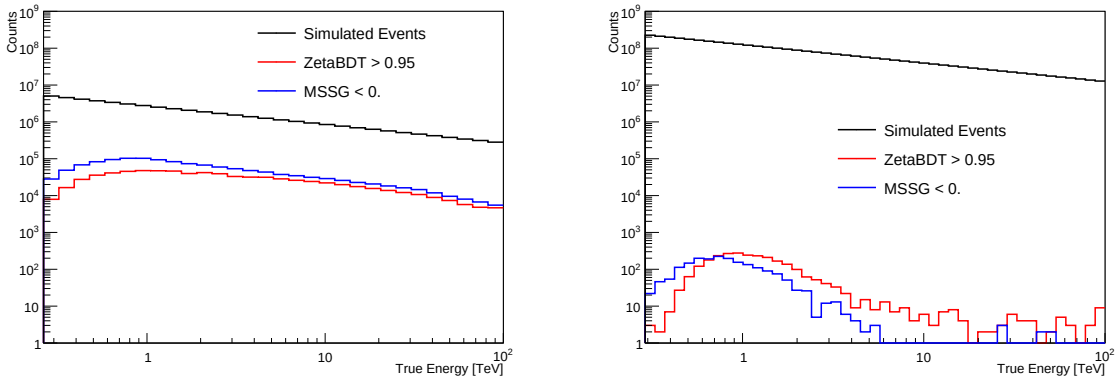

Figure 3.11: Cut efficiencies for Monte Carlo electrons (*left*) and protons (*right*). The MSSG analysis technique is compared to a hard cut on the ζ_{BDT} parameter for identical event selection cut.

small proton contamination.

3.4.3 Proton Contamination

In difference to the BDT analysis the proton contamination after the proton-rejection cut (MSSG < 0) cannot be extracted directly from the data themselves. It is therefore crucial to determine the expected proton contamination with simulated proton events. In Figure 3.11 the cut efficiencies of both simulated electron and proton events (data set specified in Table 3.5) are shown after the MSSG cut. Only cut efficiencies for proton Set A are shown here. Additionally the MSSG cut efficiency is compared to a hard cut on $\zeta_{BDT} > 0.95$. In order to directly compare both rejection methods the ImPACT-MSSG event pre-selection cuts, specified in Table 3.6, were used for both methods. It is observable that the MSSG method is superior to the ZetaBDT analysis with respect to both electron and proton cut efficiencies especially for energies > 1 TeV. All plots show the true energy on the x-axis, since not all simulated events have an assigned reconstructed energy (i.e. they are rejected in the image cleaning). The cut effiencies for electrons should be the same in reconstructed energies, the proton distribution should shift towards lower energies.

The proton contamination after the cut on MSSG < 0 in Figure 3.12 was estimated by assuming a factor of ~ 800 (extracted from the BESSII proton spectrum) at an energy of 400 GeV between the cosmic-ray electron and proton flux. The Monte Carlo simulations were carried out with a spectral index of 1.5, therefore both spectra had to be reweighted to an index of 2.7 and 3.3 for protons and electrons, respectively. The proton contamination for the MSSG cut is negligible for energies above a few TeV and $\sim 10\,\%$ for energies below. For reconstructed proton energies the proton contamination distribution shifts towards lower energies and can be estimated to be $\leq 15\,\%$. The ZetaBDT cut gives a higher proton contamination by roughly a factor of 2. The proton contamination shown here cannot be compared to the one achievable in the ZetaBDT analysis chain, since much looser event selection cuts were used. Both analysis chains show their best performance at $\sim 4 - 20$ TeV, above this energy the amount of misclassified proton events seems to rise. The achievable proton contamination of less than $15\,\%$ for the MSSG analysis shows that it is a very well suited analysis technique for the cosmic-ray electron spectrum. It is also much simpler than the ZetaBDT analysis since no modelling of the proton background has to be performed.

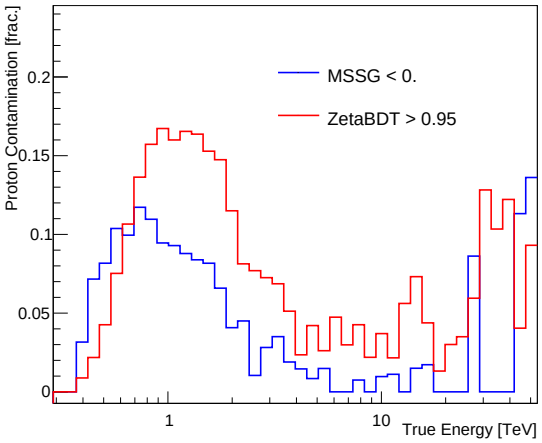

Figure 3.12: Proton contamination after the MSSG (blue) and ζ_{BDT} cut (red). A factor of 800 was assumed between the cosmic-ray electron and proton flux at an energy of 400 GeV. The simulated spectra with indices 1.5 were re-weighted to 2.7 and 3.3 respectively.

3.5 Energy and Direction Reconstruction Performance

Both analysis chains were characterized with respect to their energy and direction reconstruction performance with the help of Monte Carlo simulations of diffuse electron events. One of the most important figures of merit for an analysis chain is the energy bias, defined in Equation 3.9. For the majority of signal events the reconstructed energy should be close to the true energy. In Figure 3.14 the reconstructed energy is plotted against the true energy for a set of simulated electron events for the BDT analysis, the s.c. "energy migration matrix". Additionally the energy bias is shown. The reconstructed energy follows the true energy, no significant outliers are observable.

$$bias = \frac{E_{Reco} - E_{True}}{E_{True}} \tag{3.9}$$

In order to quantify the energy bias for a specific true energy, the energy distribution in a true energy slice of the energy migration matrix is fit with a Gaussian distribution. The extracted mean value is defined as energy bias for this energy band, the 68 % containment interval is defined as energy resolution. In Figure 3.14 and 3.15 the energy bias and resolution are compared between the different analyses and several zenith angle bands for the optical phase 1b. Differences in the energy reconstruction performance between the analysis chains are only due to different quality cuts, since all chains use the standard energy calibration technique. The ImPACT-MSSG analysis shows higher energy bias values for low energies due to the increased telescope size cut. This leads to a higher energy threshold of the analysis with respect to the TMVA analysis due to the fixed threshold defined as the energy at which the bias exceeds 3 % (see Section 3.2). As expected higher zenith angles lead to higher energy thresholds. The same effect would be observable for energy bias plots of phase 1c. Overall the energy bias is $\leq 3\,\%$ for the whole energy range used in this work and the energy resolution is $\sim 10\,\%$.

A bigger difference between the ImPACT-MSSG and the ZetaBDT analysis chain is visible in the directional reconstruction performance. The angular resolution is defined as the 68 % containment interval of the directional bias distribution. For a simulated point source this

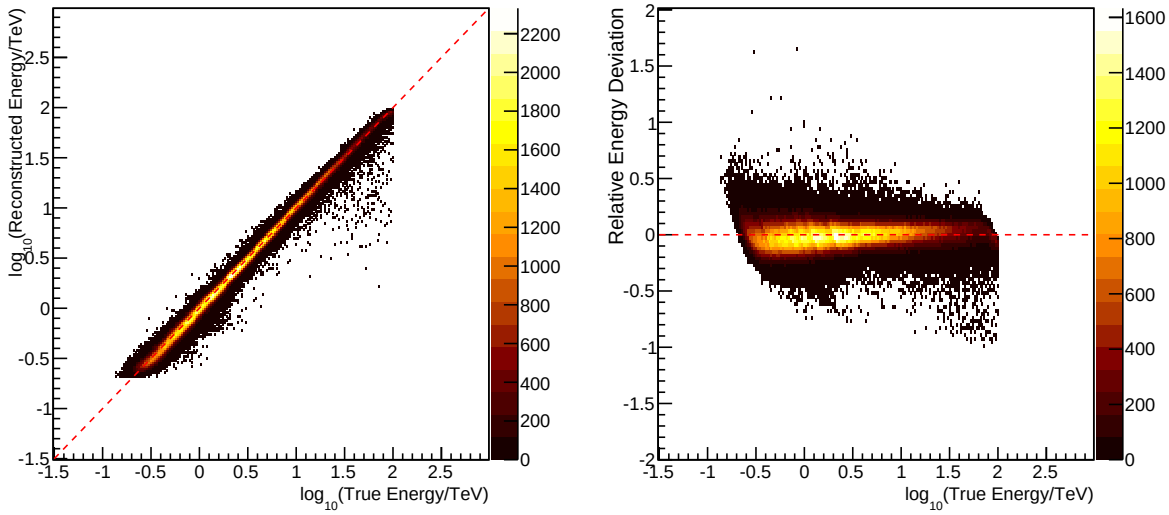

Figure 3.13: Energy migration matrix for diffuse Monte Carlo electron simulations and the ZetaBDT analysis chain (*left*). The energy bias distribution (*right*) is one of the the main figures of merit for characterizing the performance of an analysis chain.

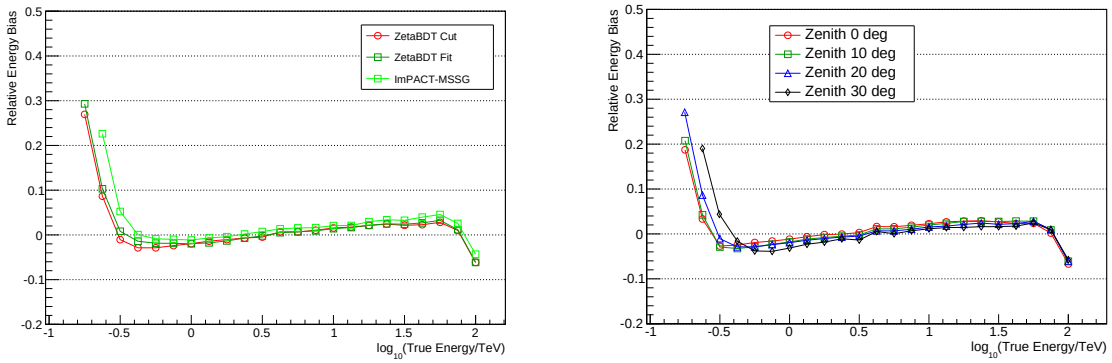

Figure 3.14: Mean energy bias for all analysis chains and optical phase 1b at a fixed zenith angle of 20 ° (*left*) and for the ZetaBDT-Fit analysis at several zenith angles (*right*).

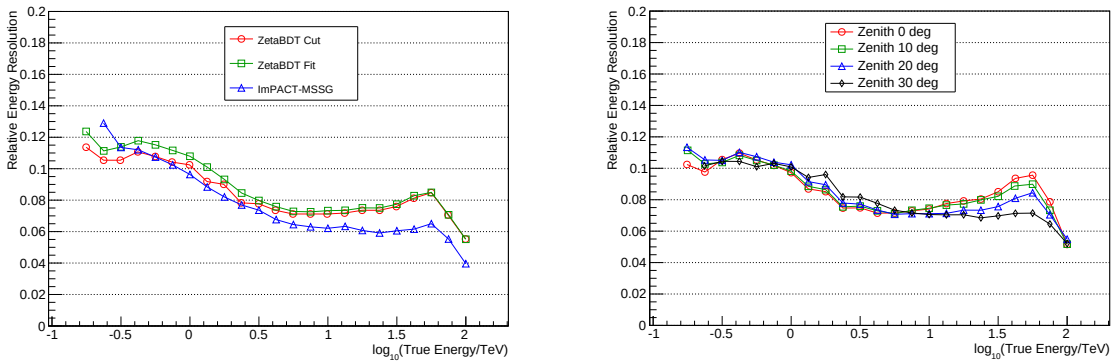

Figure 3.15: 68 % containment value for the energy bias distribution for all analysis chains and optical phase 1b at a fixed zenith angle of 20 ° (*left*) and for the ZetaBDT-Fit analysis at several zenith angles (*right*).

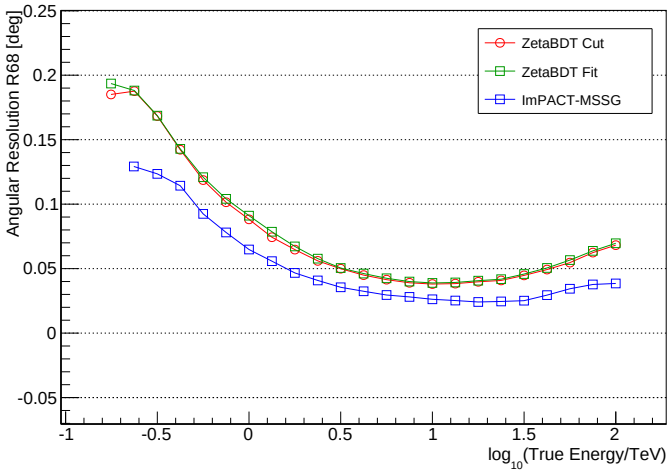

Figure 3.16: 68 % containment value for the directional bias distribution for all analysis chains and optical phase 1b at a fixed zenith angle of 20 °.

definition would correspond to the PSF. A good PSF is not essential for the analysis of diffuse emission, but it should be well enough to reject gamma rays coming from known sources. In Figure 3.16 the angular resolution is shown for all analysis chains. The directional reconstruction performance for the ImPACT-MSSG analysis is systematically better than the BDT performance. This is due to the advanced reconstruction technique with respect to the Hillas analysis.

3.6 Effective Area and Flux Determination

After the determination of the number of electrons in a specific energy band $N_{el}(E)$, the differential energy spectrum of cosmic-ray electrons can be calculated:

$$\frac{dF}{dE} = \frac{N_{el}(E)}{A_{eff}(E) \cdot \Delta E \cdot T(E) \cdot \Omega}. \tag{3.10}$$

It is defined as the number of electrons per unit time, unit area and solid angle within an energy bin of width ΔE. Here T is the energy-dependent livetime, Ω the solid angle and $A_{eff}(E)$ the effective collection area. The energy dependence of the livetime is introduced by the run-wise cut on the energy bias. $A_{eff}(E)$ is an energy-dependent product of the total collection area and the cut efficiency determined by the use of electron simulations:

$$A_{eff}(E) = \frac{N_{SEL}(E) \cdot A_{MC}}{N_{MC}(E)}. \tag{3.11}$$

$N_{MC}(E)$ is the number of simulated electron events and $N_{SEL}(E)$ the number of electrons passing all cuts at a given energy, A_{MC} is the area for which the simulations were generated. The effective areas were stored in lookup tables. For the electron analysis the effective areas were determined event-wise and averaged over all events passing the selection cuts in an energy band. The effective area lookup table layout is very similar to the one used for the energy calibration shown in Table 2.2, only that this time the effective area is also interpolated between the optical phases. Therefore additional simulations for the optical phase 1 (mirror

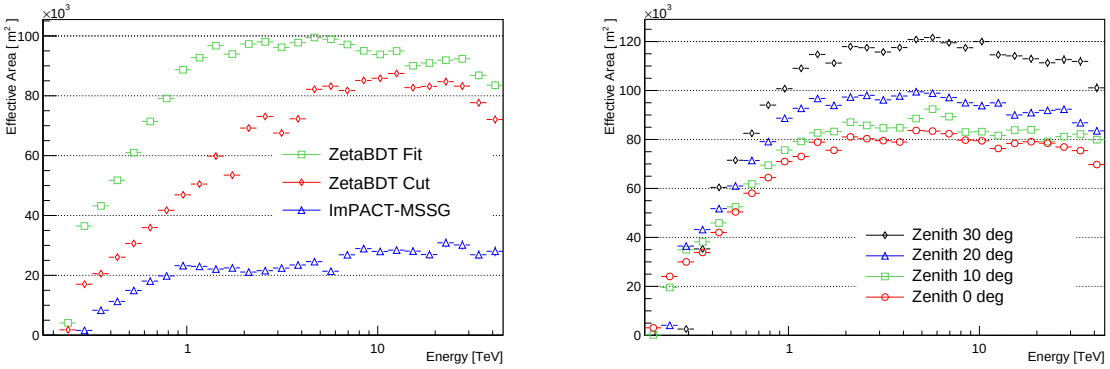

Figure 3.17: Effective collection areas for a pointsource at a zenith angle of 20 °, azimuth angle of 180 °, offset of 0.5 ° and optical phase 1b and all analysis setups (*left*). Additionally the effective areas for different zenith angle bands are shown for the ZetaBDT-Fit analysis for the same source parameters (*right*).

reflectivity 100/94/100/100) were carried out. The effective area is interpolated between the phases by using the run-wise optical efficiency determined with muon events. The effective areas had to be re-weighted with respect to the spectral index used in the simulation and the one expected for the electron energy spectrum (1.5 vs. ~ 3.3).

In Figure 3.17 the effective areas for a point source at a zenith angle of 20 °, azimuth angle of 180 °, offset of 0.5 ° and optical phase 1b are compared for the different analyses. The ImPACT-MSSG analysis shows a much lower effective area due to the very tight event selection cuts. This is mainly due to the multiplicity cut requiring four participating telescopes. The ZetaBDT analysis only differ in the tightness of the ζ_{BDT} cut, nevertheless a big fraction of low energy events is lost due to the tightened cut in the ZetaBDT-Cut analysis. Additionally, the effective area is compared for different zenith angle bands for the ZetaBDT-Fit analysis. As already observed from the energy bias plots, the effective area for higher zenith angles shows a higher energy threshold.

In order to test the accuracy of the effective areas the energy spectrum of simulated diffuse electrons was determined for all analyses (see Figure 3.18 for examples). This test was performed for multiple zenith angles, since the effective areas show the strongest variation with respect to the zenith angle compared to other event parameters. Additionally a combined Monte Carlo data set with equal weights for the zenith angle distribution was tested. For all tested analysis setups the reconstructed spectra showed a very good agreement with the simulated power law with spectral index 1.5.

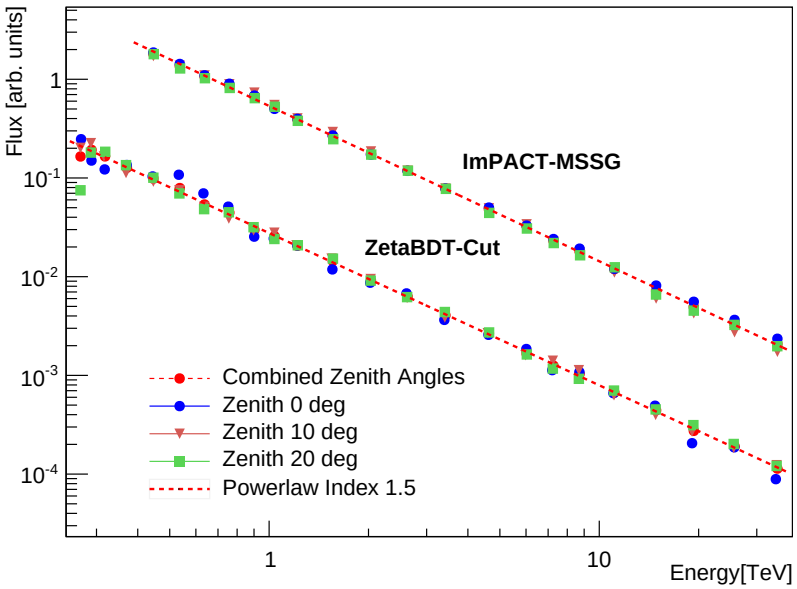

Figure 3.18: Reconstructed energy spectrum of simulated electron events for the ImPACT-MSSG and the ZetaBDT-Cut analysis for different simulated zenith angles and a combination of them. The normalization is chosen arbitrarily. Good agreement with the simulated power law spectrum with spectral index 1.5 is observable.

CHAPTER 4

The Cosmic-Ray Electron Energy Spectrum

The update of the H.E.S.S. cosmic-ray electron spectrum with respect to the publications in 2008 and 2009 started in 2014 as a simple re-analysis with an increased data set. Since then the task has evolved to one of the most intensively studied tasks in the H.E.S.S. collaboration. Not only systematic effects of the two H.E.S.S. analysis chains HAP and PA were analyzed in detail, but also the quality of the predictions of the hadronic interaction models was tested. Since a cross-check between both analysis chains is crucial for such a non-standard analysis, results from both analysis chains will be shown and discussed. On the PA side the cross-check was performed by Kerszberg (2017)

For this work the analyses $\mathbf{ImPACT-MSSG}$ and $\mathbf{ZetaBDT-Fit}$ will be used to extract the electron energy spectrum with the HAP analysis chain. The $\mathbf{Model++}$ analysis was used within the PA analysis chain. The energy spectrum is very interesting in itself, however for this work it was mainly determined as a verification of the BDT analysis later used in the anisotropy study. The energy spectrum together with the best-fit model is presented in Section 4.1, the extraction of the systematic error band will be explained in Section 4.2. A short interpretation, especially on the high energy part of the spectrum, will be given in Section 4.3. A detailed discussion of the results will follow in a later chapter together with the results of the anisotropy study, since both tasks are coupled to each other.

4.1 Energy Spectrum

The number of cosmic-ray electrons extracted with both ImPACT-MSSG and the BDT analysis are shown in Table 4.1. For the BDT analysis the number of electrons was determined by using the Monte Carlo template fit technique, for ImPACT-MSSG a simple cut on MSSG < 0 was used. The resulting χ^2 values for the comparison of Monte Carlo model and data for the BDT analysis are also stated. It is observable that for most energy bands the Monte Carlo templates describe the data very well. The template fits for every energy band are shown in Appendix A.3.

Energies [TeV]	Number $e^- + e^+$	Reduced χ^2
$[0.3, 0.338)$	1333	33/20
$[0.338, 0.407)$	12065	26/20
$[0.407, 0.489)$	20654	31/20
$[0.489, 0.598)$	16444	51/20
$[0.598, 0.69)$	12675	38/20
$[0.69, 0.83)$	11715	27/20
$[0.83, 0.98)$	7313	62/20
$[0.98, 1.1)$	3856	44/20
$[1.1, 1.35)$	5349	33/20
$[1.35, 1.8)$	3955	27/20
$[1.8, 2.3)$	1589	49/20
$[2.3, 3)$	951	29/20
$[3, 3.9)$	366	33/20
$[3.9, 5.5)$	310	42/20
$[5.5, 6.6)$	109	31/20
$[6.6, 8)$	89	36/20
$[8, 9.5)$	76	31/20
$[9.5, 13)$	93	27/20
$[13, 17)$	60	20/20
$[17, 22)$	40	13/20
$[22, 30)$	25	35/20
$[30, 40)$	8	12/20

Energies [TeV]	Number $e^- + e^+$
$[0.407, 0.489)$	4866
$[0.489, 0.588)$	5582
$[0.588, 0.691)$	4169
$[0.691, 0.831)$	3929
$[0.831, 0.98)$	2701
$[0.98, 1.1)$	1438
$[1.1, 1.35)$	1779
$[1.35, 1.7)$	1054
$[1.7, 2.2)$	557
$[2.2, 3.0)$	305
$[3.0, 4.0)$	104
$[4.0, 5.0)$	46
$[5.0, 6.7)$	42
$[6.7, 9.0)$	24
$[9.0, 15.0)$	17
$[15.0, 40.0)$	7

Table 4.1: Number of electrons as extracted in the energy bands by both the BDT (*left*) and the ImPACT-MSSG analysis (*right*). For the BDT analysis additionally the reduced χ^2 of the template fit is shown.

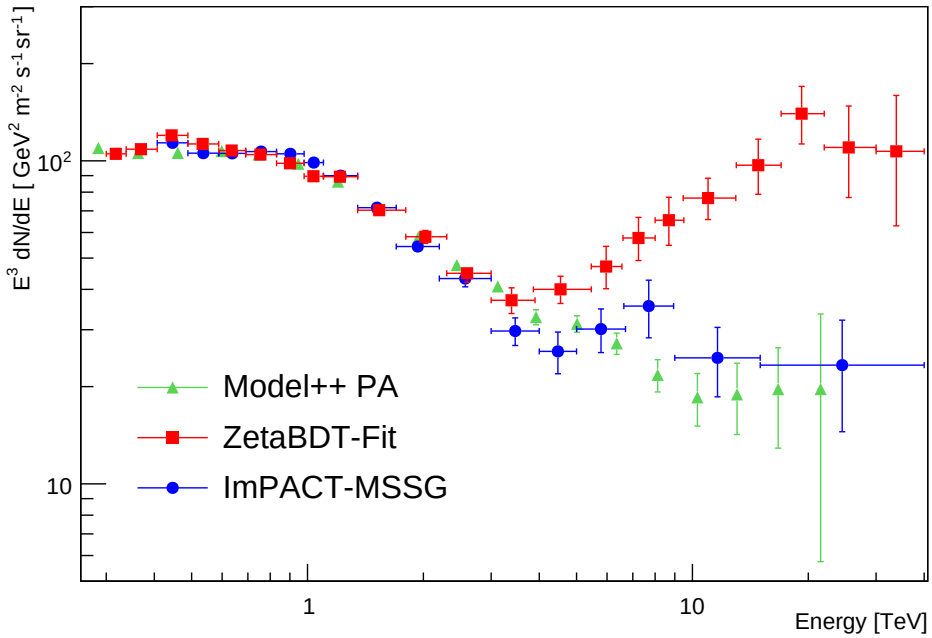

Figure 4.1: Cosmic-ray electron energy spectrum for the BDT and ImPACT-MSSG analysis with statistical errors only. Additionally the spectrum derived with the Model++ analysis is depicted.

The effective areas for the calculation of the cosmic-ray electron flux were determined as specified in Section 3.6. The resulting energy spectra for both the BDT analysis and the ImPACT-MSSG analysis are shown in Figure 4.1. Additionally the Model++ spectrum is plotted. The spectra shown use the reconstructed energy as true energy estimator, since it has been shown in Section 3.5 that the energy bias is negligible for the whole energy range. For energies close to the threshold of a run the quality of the reconstructed energy estimator is ensured by the 3 % energy bias cut. The achievable overall energy threshold is $\sim 300\,\mathrm{GeV}$ for the BDT analysis and $\sim 400\,\mathrm{GeV}$ for ImPACT-MSSG. The discrepancy between the spectra derived with the BDT and ImPACT-MSSG analysis will be discussed in Section 4.3.

The energy spectra of both the BDT and ImPACT-MSSG analysis were fitted with a smooth broken power law:

$$dN/dE = N_0 \cdot (E/E_{break})^{-\Gamma_1} \cdot \left(1 + (E/E_{break})^{1/\alpha}\right)^{-(\Gamma_2-\Gamma_1)\alpha} . \tag{4.1}$$

Here N_0 is the normalization, E_{break} the energy where the transition between the two spectral indices Γ_1 and Γ_2 occurs and α parametrizes the sharpness of the transition. The energy range of the fit was restricted to energies $< 4\,\mathrm{TeV}$ for the BDT analysis. The reasons for this choice will be discussed in detail in Section 4.3. Figure 4.3 shows the parameters of the best-fit model for both analysis techniques. Figure 4.2 shows the cosmic-ray electron spectrum derived with the BDT analysis and ImPACT-MSSG together with the best-fit models and the statistical plus systematic error band on the best-fit model. The determination method of the systematic error will be discussed in Section 4.2. Additionally the energy spectra of selected other experiments are depicted with statistical errors only. A zoom into the low energy regime is shown in Figure 4.4.

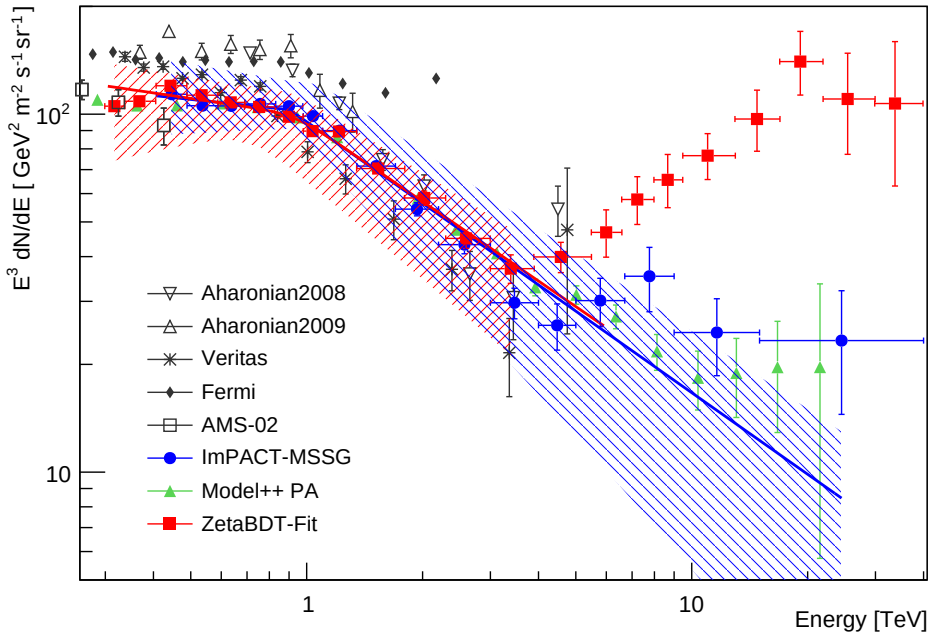

Figure 4.2: Cosmic-ray electron energy spectra for the BDT and ImPACT-MSSG analysis with their statistical errors and their systematic error bands as derived in Section 4.2. Additionaly, the spectra for Model++, AMS-02 (Aguilar et al. 2014), Fermi/LAT (Abdollahi et al. 2017b), VERITAS (Staszak 2015), and H.E.S.S. (Aharonian et al. 2008, 2009) are shown with statistical errors only. The uncertainty on the absolute energy scale is $\sim 15\,\%$ for H.E.S.S.

Impact-MSSG

Γ_1	= 3.11	±	0.04	$(stat)$	$^{+\ 0.06}_{-\ 0.12}$	(sys)
Γ_2	= 3.75	±	0.05	$(stat)$	$^{+\ 0.32}_{-\ 0.02}$	(sys)
α	= 5.0e-03	±	1.6e-6	$(stat)$	$^{+\ 3.2e-03}_{-\ 1.4e-05}$	(sys)
E_{break}	= 0.90	±	2.85e-5	$(stat)$	$^{+\ 0.21}_{-\ 0.00}$	(sys)
N_0	= 103.0	±	1.707	$(stat)$	$^{+\ 15.75}_{-\ 9.802}$	(sys)

ZetaBDT-Fit < 4 TeV

Γ_1	= 3.15	±	0.04	$(stat)$	$^{+\ 0.06}_{-\ 0.25}$	(sys)
Γ_2	= 3.74	±	0.09	$(stat)$	$^{+\ 0.12}_{-\ 0.15}$	(sys)
α	= 0.073	±	0.085	$(stat)$	$^{+\ 0.120}_{-\ 0.020}$	(sys)
E_{break}	= 0.93	±	0.11	$(stat)$	$^{+\ 0.01}_{-\ 0.22}$	(sys)
N_0	= 100.3	±	4.022	$(stat)$	$^{+\ 9.293}_{-\ 1.090}$	(sys)

Figure 4.3: Best-fit model parameters of the smooth broken power law model for the ImPACT-MSSG analysis $(left)$ and the BDT analysis $(right)$. The energy range for the BDT analysis was restricted to $< 4\,\mathrm{TeV}$. The reasons for this choice will be discussed in Section 4.3.

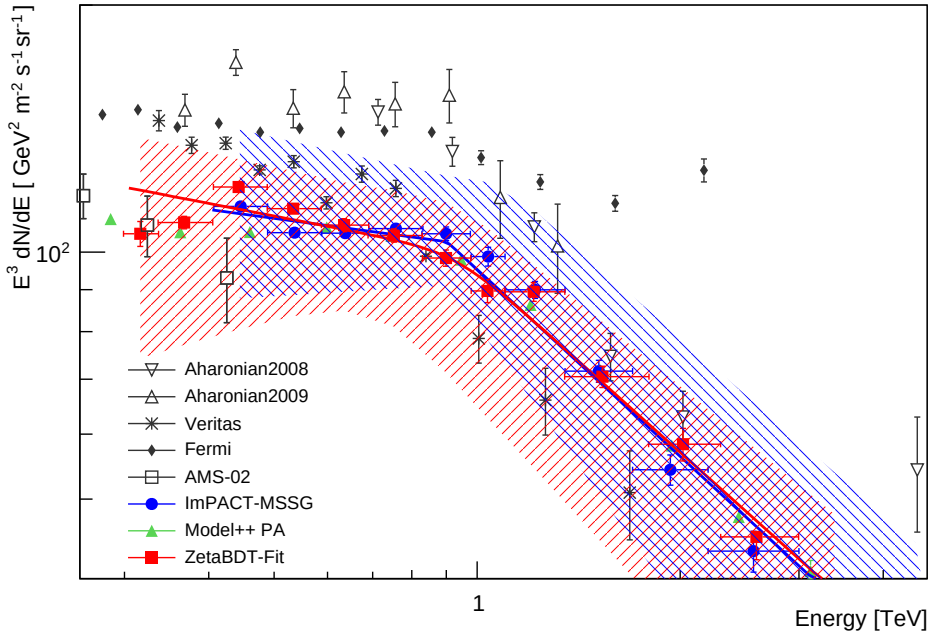

Figure 4.4: Zoom into the low energy regime of the cosmic-ray electron energy spectra for the BDT and ImPACT-MSSG analysis with their statistical errors and their systematic error bands as derived in Section 4.2. Additionally, the spectra for Model++, AMS-02 (Aguilar et al. 2014), Fermi/LAT (Abdollahi et al. 2017b), VERITAS (Staszak 2015), and H.E.S.S. (Aharonian et al. 2008, 2009) are shown with statistical errors only. The uncertainty on the absolute energy scale is $\sim 15\,\%$ for H.E.S.S.

4.2 Sources of Systematic Uncertainties

The determination of the systematic error for the electron analysis of an IACT is crucial, since the statistical error of the best-fit model is very small due to the high number of extracted electron events. The determination technique of the systematic error used in this work is the following:

- Systematic error is defined as the variation of the best-fit model parameters with respect to changing observational conditions.
- Observational conditions are changed by splitting the data set according to different observational parameters. The resulting model parameters for the two split data sets are compared to the best-fit model of the combined data set with respect to the absolute deviation.
- Upper and lower systematic errors on the parameters are treated independently. They are added in quadrature for the different data.
- The combined error band of both statistical and systematic error is given by the resulting envelope of the best-fit model.
- Parameters which directly influence the proton contamination stay fixed and are not altered (e.g. the impact distance or MSSG cut). After determination of the systematical errors it is tested if their variation is compatible with the systematic error band.
- The uncertainty on the absolute energy scale is assumed to be $\sim 15\,\%$ for H.E.S.S. (Aharonian et al. 2008).

The possible sources of systematic uncertainties differ for the BDT and ImPACT-MSSG analysis. The different data sets used for the BDT analysis are summarized in the following:

- The data set was split into optical phase 1b and 1c.
- The data set was split into runs with zenith angles $\leq 12.5\,^\circ$ and $> 12.5\,^\circ$.
- The energy spectrum derived with simulated proton events of Set A was compared to the spectrum derived with Set B.

The split into optical phases 1b and 1c directly tests the accuracy of the effective areas and especially the muon correction technique. Another measure of the accuracy of the effective areas is given by a split of the data in zenith angle bands. At low energies the effective areas strongly change shape with varying zenith angle (see Figure 3.17). Effects due to varying azimuth angles are much smaller. The energy spectrum determination with two independent hadron interaction models is specific to the BDT analysis technique since the template fit technique relies on the simulated proton template.
The data sets used for the ImPACT-MSSG analysis are:

- The data set was split into optical phase 1b and 1c.
- The data set was split into runs with zenith angles $\leq 12.5\,^\circ$ and $> 12.5\,^\circ$.
- The data set was split into events with offset angle $\leq 1.0\,^\circ$ and $> 1.0\,^\circ$.

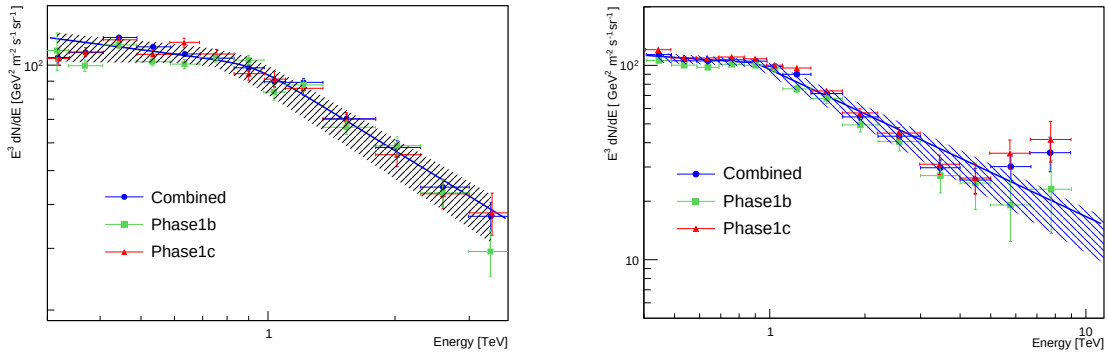

Figure 4.5: Cosmic-ray electron energy spectra for the data set split into the optical phases 1b and 1c for the BDT analysis (*left*) and the ImPACT-MSSG analysis (*right*). The resulting systematic error band is plotted in grey.

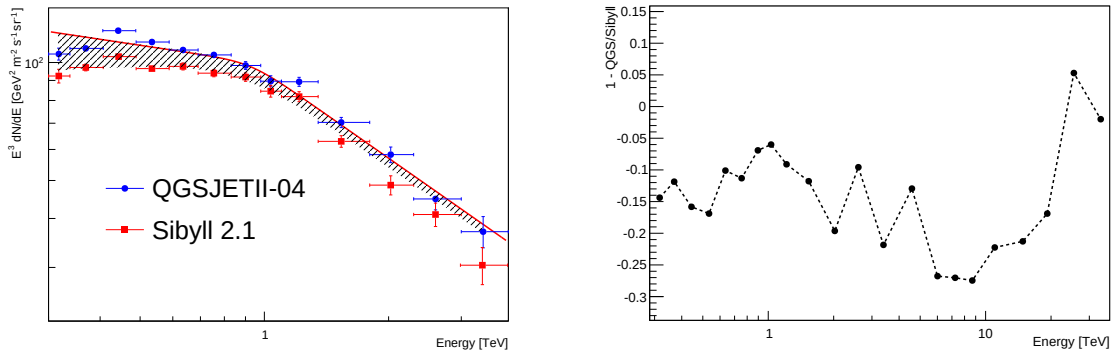

Figure 4.6: Cosmic-ray electron energy spectrum for the BDT analysis and two different hadronic interaction models (*left*). Additionally the relative flux difference in every energy band is shown (*right*).

Instead of comparing different hadronic interaction models like in the case of the BDT analysis, the data set was additionally split into two event offset bands for the ImPACT-MSSG analysis. This systematic test is not possible for the BDT analysis since the amount of Monte Carlo proton data necessary for the template fit technique could not be reached in individual offset bands.

The results of the split of the data into optical phases is shown in Figure 4.5. The error band plotted is given by the systematical error only. Whereas no systematic flux trend is observable for the BDT analysis, a systematically lower flux of $\sim 10\,\%$ is observable in the case of optical phase 1b with respect to 1c in the case of the ImPACT-MSSG analysis. The same observation was made for the split in zenith and offset angle. Overall the BDT analysis seems to be very stable with respect to the observational conditions. This is very likely due to the event classification not based on parameters proportional to the measured size value. In the ImPACT-MSSG analysis the measured size value is directly compared to a Monte Carlo template, which is very vulnerable to systematics in the event reconstruction chain. A direct consequence is the large systematical uncertainty on the flux normalization N_0.

Of particular importance for the anisotropy analysis with the BDT technique is the systematic uncertainty of the electron fraction with respect to different hadronic interaction models. In

Figure 4.6 the energy spectra for the BDT analysis determined with both protons of Set A (QGSJETII-04) and B (Sibyll 2.1) are shown. Additionally the relative flux difference is calculated for every energy band. It is observable that the flux is systematically $10\,\% - 15\,\%$ lower for Sibyll 2.1 than for QGSJETII-04.

4.3 Interpretation

The interpretation of the cosmic-ray electron energy spectrum as measured in this work is divided into a low-energy part (energy $< 4\,\mathrm{TeV}$) and a high-energy part.

Low energy part

The low energy regime of the cosmic-ray electron spectrum is very well described by a broken power law model for both analysis techniques. The determined parameters of the best fit of both techniques are in agreement with respect to their statistical and systematic errors. Both analysis chains predict a sharp break in the spectral index at a break energy of $\sim 1\,\mathrm{TeV}$. The observation that the normalization of the spectra for both techniques is in very good agreement despite the proton contamination of $\sim 10 - 15\,\%$ for the ImPACT-MSSG analysis can have different origins. Either the normalization is overestimated by the QGSJETII-04 interaction model, as suggested by the comparison with the Sibyll model, or the proton contamination for ImPACT-MSSG, estimated with the help of simulations, is overestimated at low energies.

The BDT analysis result of this work is not compatible with the results of the previous H.E.S.S. publications (HAP analysis with RFs instead of BDTs). The situation gets even more severe due to the fact that for the extraction of the previous H.E.S.S. electron spectra the Sibyll interaction model (version 1.7) has been used, which shows a tendency to lower electron fractions in the signal region (similar to the result shown in this work, see Figure 4.6). The reasons for these systematic differences are very likely to be found in the quality of the energy reconstruction and the determination of the effective areas. The energy reconstruction in the original analysis used only one optical phase and consequently a very large range of relative muon correction factors (between 20 % and 60 %) were used. For large muon correction factors the simple linear rescaling of the measured size value might not be applicable. In this work the relative muon correction is always smaller than 20 % (see Figure 2.9). The same argument applies to the determination of the effective areas.

The ImPACT-MSSG analysis is in very good agreement with its counterpart Model++ on the PA side. Model++ should show a similar proton contamination like ImPACT-MSSG. Given that both analysis have a completely independent calibration, reconstruction and classifying chain the agreement is excellent. The Model++ energy spectrum is within the systematic error band of the ImPACT-MSSG analysis. Given that the ImPACT-MSSG analysis chain is very new and has never been used before, the level of agreement is quite remarkable.

High energy part

The high energy part ($> 4\,\mathrm{TeV}$) of the electron spectrum is governed by a very large discrepancy between the BDT analysis and ImPACT-MSSG. The BDT analysis spectrum shows an

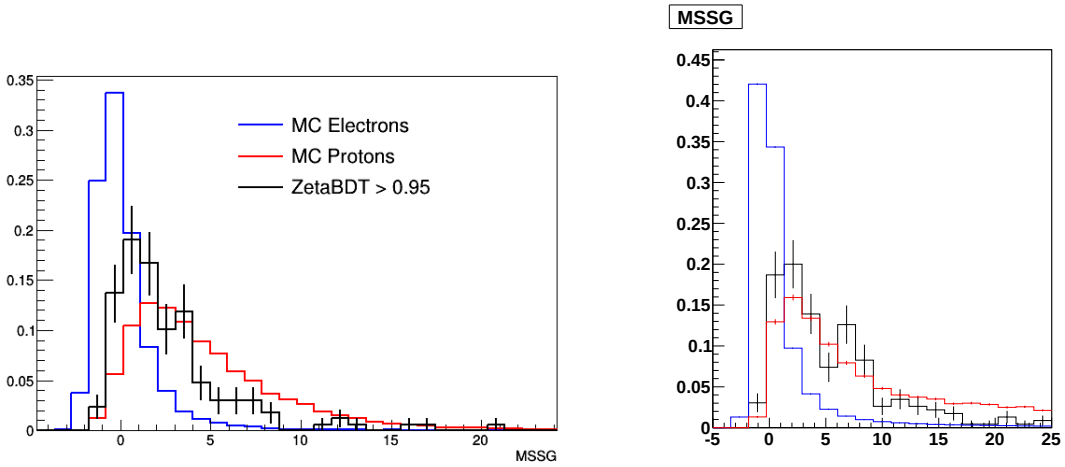

Figure 4.7: MSSG distributions for events with energies $> 10\,\text{TeV}$ and ζ_{BDT} values > 0.95 for ImPACT-MSSG (*left*) and Model++ (*right*) shown in black. The MSSG distributions of simulated electron and proton events are depicted in blue and red respectively.

upturn at a break energy of $\sim 4\,\text{TeV}$ with an spectral index of ~ 2.2. Furthermore beyond energies of 10 TeV there are hints of a flattening of the spectrum. This feature is however not significant, a spectral break is only favored with $0.8\,\sigma$. The ImPACT-MSSG spectrum on the other hand is compatible with the best-fit broken power law model up to highest energies. Two possible sources of the upturn will be discussed in the following, a real electron signal and a contamination of protons. A gamma-ray contamination can be excluded with the choice of the run and event selection cuts.

Real cosmic-ray electron signal

The spectral upturn combined with a possible flattening at highest energies fits very well to the scenario of a dominating Vela SNR/PWN (see Figure 1.6). However, if the spectral upturn of the BDT analysis is of astrophysical origin this would consequently lead to the conclusion that both MSSG analyses systematically reject electrons at high energies. Furthermore they have to be rejected in exactly these numbers that the resulting spectrum fits to the pure power law above 1 TeV. This is regarded as highly unrealistic. The behavior was not observed for simulated electrons and since the simulation of electrons is very accurate (no hadronic interactions) an astrophysical origin is at least disfavored. It can however not be excluded.

Proton contamination

The consideration that the spectral upturn of the BDT cosmic-ray electron spectrum is due to a proton contamination has an immediate consequence. It means that both hadronic interaction models used in this work predict a much too low number of very gamma-like proton showers ($\sim$ a factor of 5 too low). The ImPACT-MSSG analysis does not depend on these interaction models and seems to be able to reject these events that are classified as very gamma-like in the BDT analysis. In order to verify this assumption the MSSG distribution of events with energies $> 10\,\text{TeV}$ and ζ_{BDT} values > 0.95 was determined for both ImPACT-MSSG and Model++. The resulting distributions in Figure 4.7 show that only $\sim 15 - 20\,\%$ of these events survive the MSSG cut. For both MSSG analyses the majority of these events

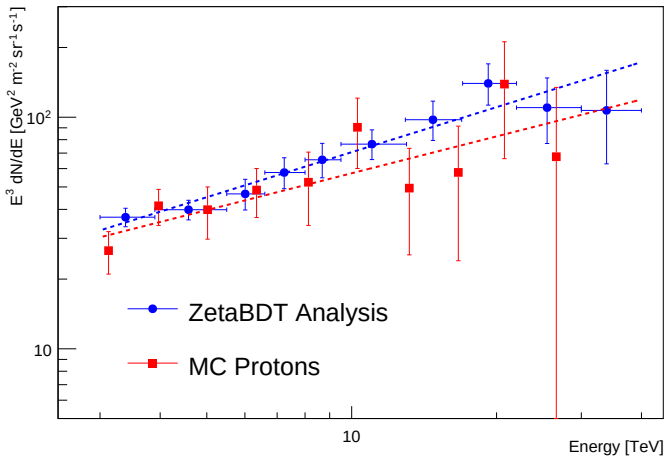

Figure 4.8: Simulated proton flux as reconstructed with the Model++ electron analysis for a simulated spectral index of 2.7 in red and the BDT electron flux in blue. The resulting proton spectrum shows a much harder spectrum than the simulated one and agrees very well with the BDT spectrum.

are therefore classified as proton-like and are rejected. It was also verified that no other event selection cut suppresses the spectral upturn in the MSSG analysis.

A hint towards a proton contamination is shown in Figure 4.8. Protons events with a spectral index of 2.7 were simulated for the Model++ chain in order to test the response of the analysis. The proton flux was determined using the same diffuse Model++ electron analysis technique as for the electron spectrum itself. These simulations were not done for the HAP chain since it requires a huge amount of CPU time to acquire enough statistics with this spectral index. The Model++ proton flux was then compared to the BDT electron flux above 4 TeV. Since the effective areas are constant above several TeV, the spectral shape should not depend on the used analysis chain. It is observable that despite being simulated with a spectral index of 2.7, the reconstructed index is much harder ($\sim$ 2.1). The spectral shape fits very well to the BDT upturn.

In summary the proton contamination scenario is regarded the most realistic one. The electron spectrum measured with ImPACT-MSSG and Model++ extends to energies that have not been accessible until now. It was shown that no anticipated spectral feature occurs in the TeV regime. Furthermore this work highlights that analysis methods based on image likelihood techniques are far superior to the classical Hillas analysis.

CHAPTER 5

All-Sky Cosmic-Ray Electron Anisotropy Analysis

Cosmic-ray electron anisotropy studies have not been accessible so far for IACTs due to the high degree of systematics involved and the fact that only a small fraction of the whole sky can be covered by a single IACT. In principle a very straightforward anisotropy analysis is possible by determining the electron flux for all covered directions using the associated effective areas. This method will be applied in Chapter 6. However, the systematic error of the effective areas is a priori unknown and furthermore usually regarded to be too large to constrain anisotropies on the %-level. This argumentation is not only true for IACTs, but for anisotropy studies in general (see Fermi/LAT analysis by Ackermann et al. (2010)). The usual approach for dealing with most systematics is to generate isotropic background maps directly from the data themselves by reshuffling event directions. These background maps answer the question of how a sky map would look like if the cosmic-ray electron flux was isotropic. This approach has proven to give good results at least for the Fermi/LAT analysis with its wide field of view.

It will be shown in the following that it is possible to use an adapted version of this method to constrain the dipole component of the cosmic-ray electron anisotropy by making use of the expected isotropy of cosmic-ray protons. It will be furthermore shown that, to a lesser extent, also anisotropies of smaller scale ($< 90\,^\circ$) can be studied. The focus in this work however lies in the dipole component. The method itself will be introduced in Section 5.1. The signal and background map generation method and necessary corrections that have to be applied to the data will be explained in the Sections 5.2 - 5.4. The method will be tested and explained in detail for the horizontal coordinate system in Section 5.5, the analysis results in the equatorial coordinate system will be shown in Section 5.6. The angles in the horizontal system are given by the zenith and azimuth angle, in the equatorial system they are given by the rectascension and declination. The analysis setup used for this anisotropy study is $\mathbf{ZetaBDT-Cut}$. Due to the fact that the BDT analysis has proven to not be reliable in the high-energy regime, an additional upper limit on the event energy of 4 TeV has been introduced.

5.1 Method

The data set used for this analysis is the one specified in Table 3.2 for the BDT analysis. The anisotropy analysis method used in this work is structured in the following steps. The individual steps will be explained in more detail in the corresponding sections.

- Events are classified with the BDT analysis and sorted into three energy bins [0.4,4.0], [0.5,4.0] and [0.64,4.0] TeV. They only differ in the lower energy threshold.
- Generation of signal sky maps filled with events that survive a ζ_{BDT} cut of > 0.95.
- Generation of isotropic background sky maps from ζ_{BDT} bands of gamma-like cosmic-ray protons.
- Determination of the electron fractions in both signal and background maps.
- Spatial integration of both maps with circular kernels and several radii (10 °, 30 °, 60 ° and 90 °). Every integration kernel is sensitive to a different anisotropy scale.
- Pixel-to-pixel comparison of integrated signal and background maps and anisotropy significance determination for all integration radii.
- Determination of the upper limits on the fractional excess for all pixels of the sky map. This has been done for an integration radius of 90 ° only.
- Determination of dipole amplitude upper limits for simulated dipole sources for the whole sky.

5.2 Signal and Background Map Generation

The most crucial part of the anisotropy analysis is the generation of the background or exposure maps. Due to the limited field of view of IACTs it is not practical to isotropize the signal data by themselves. In the case of satellite experiments this is usually done by a reshuffling of signal events. The event times and directions of randomly drawn events are successively interchanged. After many iterations all potential anisotropies are washed out and the resulting sky map effectively yields the exposure for all covered directions.

Another possibility of generating isotropic background maps is to fill them with a reference signal that is known to be isotropic. For IACTs the best option for this reference signal are gamma-like protons. The necessary condition to be gamma-like is due to the fact that only for these events the direction can be reconstructed with the Hillas method. Cosmic rays (and therefore also protons) are known to be isotropic in the high GeV/TeV range to a level of $\sim 0.1\,\%$ as measured by ARGO-YBJ (Di Sciascio et al. 2012), the Tibet Air Shower Array (Amenomori et al. 2017) or Icecube/HAWC (The HAWC Collaboration & The IceCube Collaboration 2015).

In order to use protons as isotropic reference signal, the BDT score variable is partitioned into a signal region S and two background regions B1/B2 as shown in Figure 5.1. The B1 sky map is generated to be compared to the signal map S, the B2 sky map will only be used for comparison against the B1 sky map. By searching for anisotropies between the isotropic maps B2/B1 potential systematics of the method itself can be evaluated. The widths of the

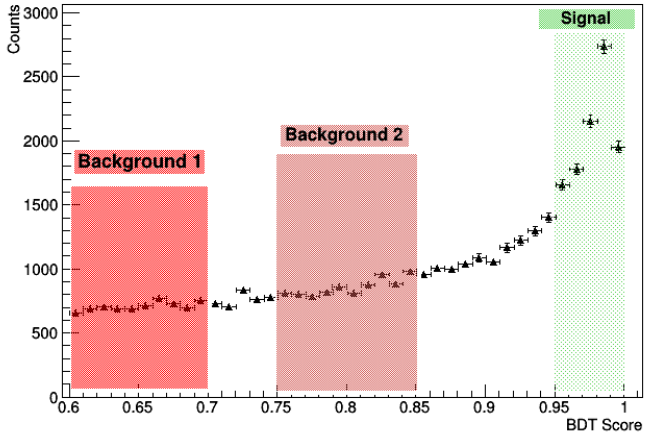

Figure 5.1: BDT score distribution with the signal region in green and the two background regions in red. The size of the background regions is chosen in such way that the number of event counts matches that of the signal region.

background regions are chosen in such way that the number of events in these regions match the one in the signal region. The edge values are stored in lookup tables with the following layout:

- Energy bins 0.4-0.5 TeV, 0.5-0.64 TeV, 0.64-1.04 TeV, 1.04-4.0 TeV
- Zenith angle bins $0 - 5\,^{\circ}$, $5 - 15\,^{\circ}$, $15 - 25\,^{\circ}$
- Optical phases 1b and 1c

In the actual filling process of the background sky maps the BDT score edges are evaluated for every event by interpolating between the lookups that fit the observation and event parameters best. It is then determined if the event lies in one of the predefined BDT regions. The strength of this exposure determination method is that signal and background maps have the same distribution of observational parameters in every pixel. Varying atmospheric conditions will influence both signal and background maps, effectively cancelling out atmospheric effects in every pixel. However the atmospheric quality will also systematically change from pixel to pixel, for example due to seasonal effects. In order to overcome these effects an atmospheric weight σ_{at} is assigned to both signal and background events according to the mean transparency coefficient of their run. This atmospheric weight determination technique is presented in Section 5.4.

Additionally to these atmospheric weighting also azimuthal north-south effects have to be corrected. The effective area differs by $\sim 10\,\%$ between north and south pointing directions at energies $< 1\,\text{TeV}$ due to magnetic field effects. This increased effective area induces a north-south anisotropy in the horizontal system, that could potentially induce an anisotropy in the equatorial system. In order to correct this unwanted anisotropy the north-south trend of the effective areas is extracted with the help of simulated electrons. Since only simulations for electrons coming directly from south and north were available, a linear trend between both directions was assumed. A weighting factor is then applied event-wise only to signal events, not to background events like in the case of the atmospheric correction. Simulated proton

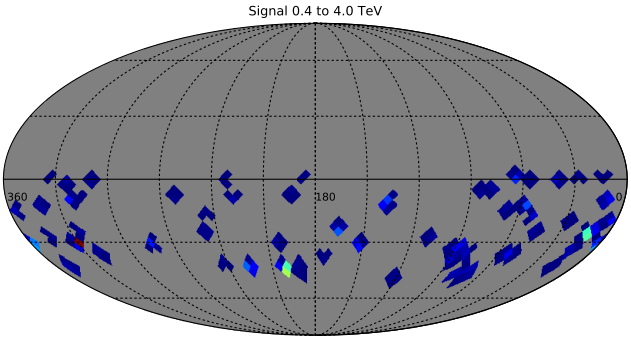

Figure 5.2: Signal sky map filled with electron candidate events that pass the $\zeta_{BDT} > 0.95$ cut in equatorial coordinates for the [0.4,4.0] TeV energy bin.

events did not show the same behavior and are therefore not corrected. Both the atmospheric and the azimuthal correction procedure have the side effect that the pixel event counts are not discrete any more after the correction.

The sky maps are pixelized using the python implementation of the HEALPix package (Górski et al. 2005) with the $NSIDE = 16$ option that determines the size of the pixels. This package discretizes spherical maps into pixels covering a constant solid angle. An example of a discretized signal map in equatorial coordinates with an energy threshold of 400 GeV is shown in Figure 5.2.

5.3 Determination of the Pixel Electron Fractions

The electron fractions in both signal and background maps are determined event-wise with the help of lookup tables. The tables are generated in zenith angle and optical phase bins with the Monte Carlo template fit technique introduced in Section 3.3.3. The lookup layout is identical to the one used for the background map generation. In Figure 5.3. example lookups are shown for all zenith angle bins of optical phase 1b. By interpolating between the lookups the electron likeliness of an individual event and the mean electron fraction for every sky map pixel can be determined. This method of determining the pixel electron fraction is inferior to a direct template fit for every individual pixel. However many pixels, especially for the highest energy threshold, lack the necessary statistics for a direct fit. The knowledge of the average electron fraction is not necessary for the search for anisotropies directly, but only for the determination of dipole amplitude upper limits. Therefore an estimate of the electron fraction using the lookup method is sufficient. Effects due to the choice of this method have to be taken into account for the determination of the dipole amplitude upper limits and will be discussed in later chapters. The electron fraction distribution for all sky map pixels and all energy thresholds is shown in Figure 5.4. The signal map electron fraction is well above 50 % for most sky map pixels. The B1 and B2 electron fractions are $\sim 3\,\%$ and $\sim 8\,\%$ respectively.

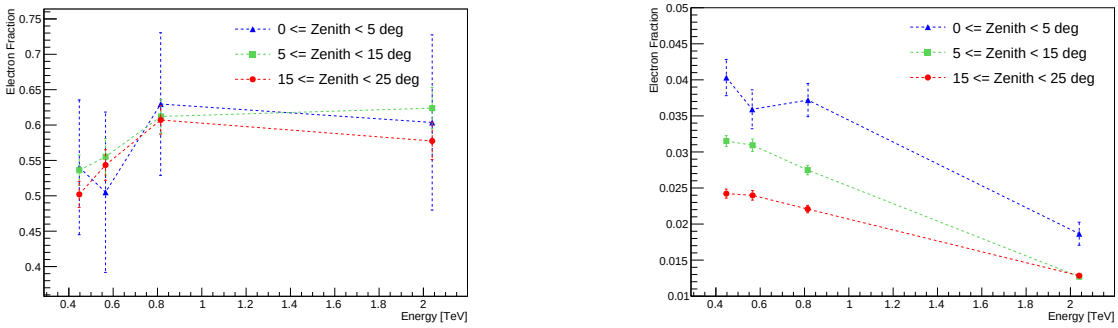

Figure 5.3: Electron fraction lookups for optical phase 1b for the signal region (*left*) and the background 1 region (*right*). The electron fractions for the signal region for phase 1c are $\sim 10\,\%$ lower. The electron fraction is determined using the Monte Carlo BDT template fit technique.

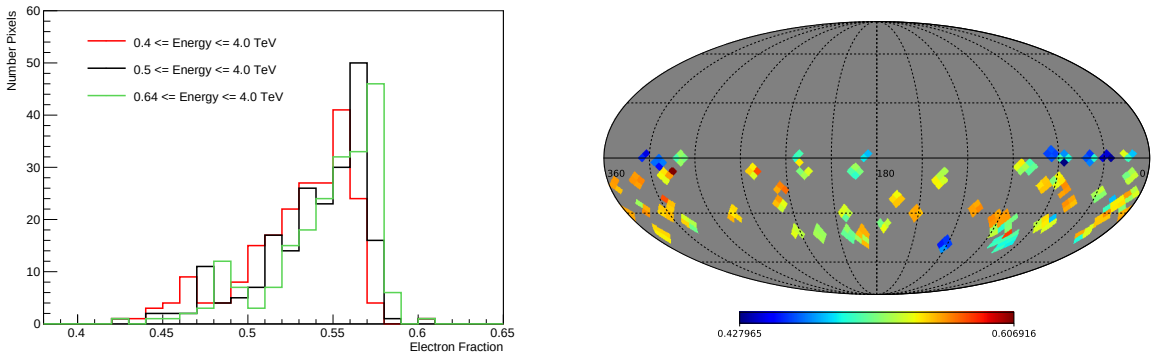

Figure 5.4: Mean electron fraction distribution for all signal sky map pixels and all energy thresholds (*left*). Additionally the electron fraction sky map is shown for the 0.64 TeV energy threshold (*right*).

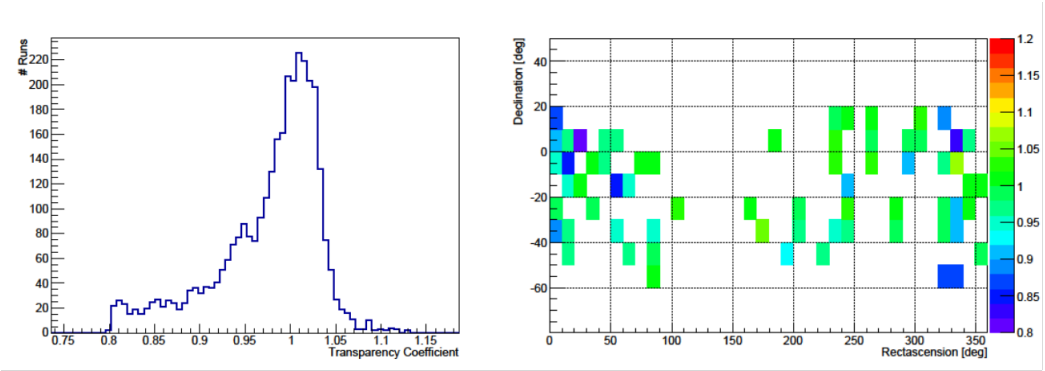

Figure 5.5: Runwise transparency coefficient distribution for the dataset used in the BDT analysis (*left*) and the average transparency coefficient for all sky map pixels in the equatorial system (*right*).

5.4 Optical Transparency Corrections

The transparency coefficient TC, introduced by Hahn et al. (2014) for the H.E.S.S. experiment as a hardware-independent measure of the atmosphere quality, is defined in Equations 5.1 and 5.2. The telescope transparency coefficients TC_i are calculated with the help of three run observables, the stereoscopic read-out rates R_i, the gain factors g_i and the muon efficiencies μ_i. The TC value for a specific run is then generated by summing over the telescope transparency coefficients of the N active telescopes. The normalization factors k_N make sure that the transparency coefficient peaks at a value of one for all combinations of active telescopes. The TC is based on the assumption that the read-out rates are dominated by cosmic-ray protons with a power law energy spectrum of index ~ 2.7 and that the normalization can be predicted for known g_i and μ_i.

$$TC_i = \frac{R_i^{-1.7}}{\mu_i \cdot g_i} \tag{5.1}$$

$$TC = \frac{1}{N \cdot k_N} \sum_i TC_i \tag{5.2}$$

The choice of the peak value of the transparency coefficient is arbitrary. The TC purpose is to quantify the quality of the atmosphere and deviations from a "'normal" atmosphere. The transparency coefficients for all runs used for this analysis are shown in Figure 5.5 together with the mean transparency coefficients for all sky map pixels in the equatorial system. It is observable that the distribution peaks at a value of one (as defined) and has some outliers towards smaller values. This justifies the approach of not correcting for atmospheric effects for the determination of the energy spectrum. However, the transparency coefficient distribution among the sky map pixels shows that single pixels and sometimes also several adjacent ones feature a transparency coefficient that is systematically lower than the average. The usual run quality selection uses a simple cut on the transparency coefficient as introduced in Section 3.2. However, in the following it was used to correct the measured cosmic-ray electron flux directly. According to Hahn et al. (2014) the measured flux depends on the transparency coefficient like:

$$F \propto T^{\Gamma-1}. \tag{5.3}$$

Here Γ is the spectral index of the signal energy spectrum. The measured fluxes were corrected event-wise with a weight $\sigma_{at} \propto \frac{1}{T^{\Gamma-1}}$. The weight values were stored in lookup tables

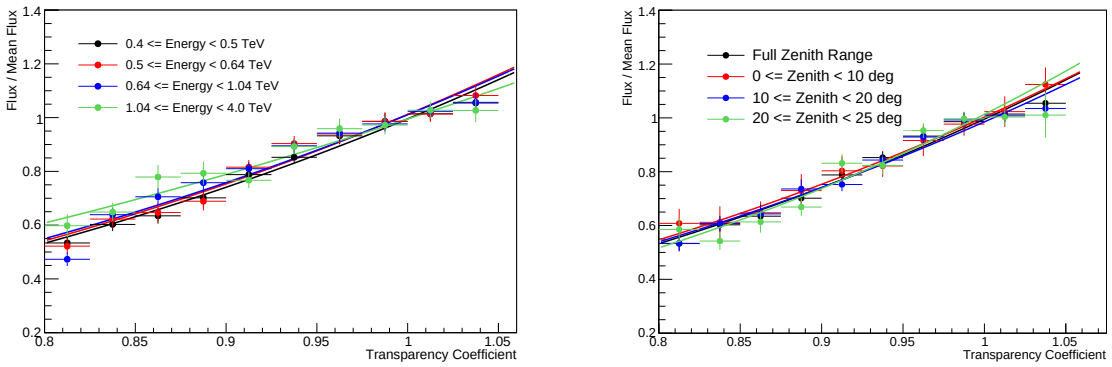

Figure 5.6: Transparency coefficient lookups used for the flux correction (*left*) and a data split in zenith angle bins for the lowest energy bin (*right*).

generated out of the measured signal flux dependence itself. A lookup layout only binned in energies ($0.4 - 0.5$, $0.5 - 0.64$, $0.64 - 1.04$ and $1.04 - 4.0$ TeV) was used. The signal events were filled in TC bins and the flux was calculated according to Equation 3.10. The flux-TC dependence was then fitted with a function according to Equation 5.3. In general it can be dangerous to correct atmospheric effects with the use of the signal flux itself, because potential anisotropies could be washed out. It was therefore checked very intensively that the flux dependence on the transparency coefficient is comparable for different zenith and azimuth angles and changing optical efficiencies. Examples for the measured flux-TC dependencies for data sets divided in energy and zenith angle bins are shown in Figure 5.6.

A direct correction of the measured signal flux only corrects for one effect of changing atmospheric conditions. In reality not the flux itself, but the energy reconstruction of an event is affected by atmospheric absorption. Events recorded during a high-absorption run will systematically show a too low reconstructed energy and will therefore be sorted into a lower energy bin. However their BDT score will differ from that of an average low energy event. Since the BDT score shape changes with energy, this will introduce systematic effects that cannot be corrected, at least for this analysis. The comparison of the two isotropic background maps B2/B1 has been introduced in order to be sensitive to these systematics. A proper treatment of changing atmospheric conditions would comprise a transparency coefficient-dependent energy calibration. The work on such an implementation is currently ongoing for the H.E.S.S. experiment.

5.5 Performance Tests in the Horizontal System

The anisotropy analysis method in this work was designed for the equatorial system. However the horizontal system offers the possibility to test the performance of this method. It has the advantage that atmospheric effects will be washed out, because the same zenith-azimuth angle combination can be recorded at different atmospherical conditions and is not bound to seasonal effects. Furthermore real electron anisotropies imminent in the equatorial system will be heavily suppressed. The number of pixels with exposure in the horizontal system is ~ 700.

The starting point for the anisotropy analysis is the pixel-wise significance calculation of

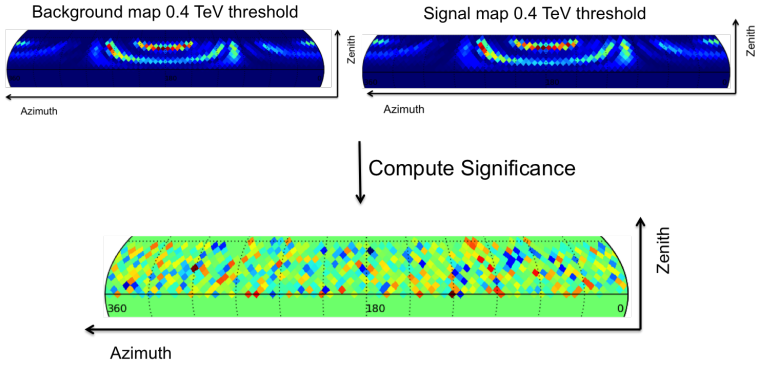

Figure 5.7: Illustration of the S/B1 significance map generation technique for the lowest energy threshold of 0.4 TeV in the horizontal system. The sky map pixel event counts can be treated as independent random variables.

Energy Threshold [TeV]	S/B1	B2/B1
0.4-4.0 TeV	$\mu = 0.017$	$\mu = -0.012$
	$\sigma = 1.12$	$\sigma = 1.07$
	$\chi^2 = 6.3/15$	$\chi^2 = 8.8/15$
0.5-4.0 TeV	$\mu = 0.008$	$\mu = -0.026$
	$\sigma = 1.07$	$\sigma = 1.06$
	$\chi^2 = 21/16$	$\chi^2 = 15/14$
0.64-4.0 TeV	$\mu = -0.017$	$\mu = -0.011$
	$\sigma = 1.07$	$\sigma = 1.08$
	$\chi^2 = 6.7/14$	$\chi^2 = 10/14$

Table 5.1: Parameters of the best-fit Gaussian models to the significance distributions of the uncorrelated S/B1 and B2/B1 comparison in the horizontal system. Here μ is the mean and σ the width of the Gaussian. Additionally the reduced χ^2 values are shown.

the difference in event counts for the signal and isotropic background maps. The pixel significances are calculatd for signal-background (S/B1) and background-background (B2/B1) maps after applying the azimuthal and atmospheric corrections described in the previous sections. The significance σ defined in Equation 5.4 was used as a measure for the pixel-to-pixel deviation between the two sky maps. For the S/B1 comparison with N_S^i signal and N_{B1}^i background counts in pixel i it is defined as:

$$\sigma_{LiMa}^i = \frac{N_S^i - N_{B1}^i}{\sqrt{N_S^i + N_{B1}^i}}. \tag{5.4}$$

One of the resulting significance maps is shown in Figure 5.7 for the example of the map produced with the energy threshold of 0.4 TeV. The pixels of the resulting significance maps are uncorrelated, the event counts in each pixel can therefore be treated as random variables. The significance distribution over the whole map should therefore be Gaussian distributed with zero mean and unit variance. The examples of the significance distribution of both S/B1 and B2/B1 for the 0.4 TeV and 0.64 TeV threshold are shown in Figure 5.9. The mean μ, variance σ and reduced χ^2 values of the best-fit Gaussian models are stated in Table 5.1.

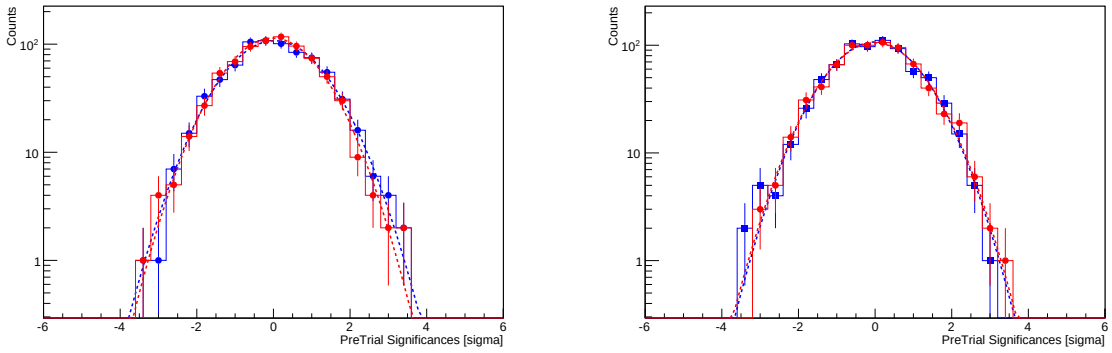

Figure 5.8: Significance distributions for the significance maps determined for S/B1 (blue) and B2/B1 (red) for uncorrelated pixels and the 0.4 TeV (*left*) and 0.64 TeV (*right*) energy threshold in the horizontal system. The distributions are fitted with a Gaussian distribution (dashed lines).

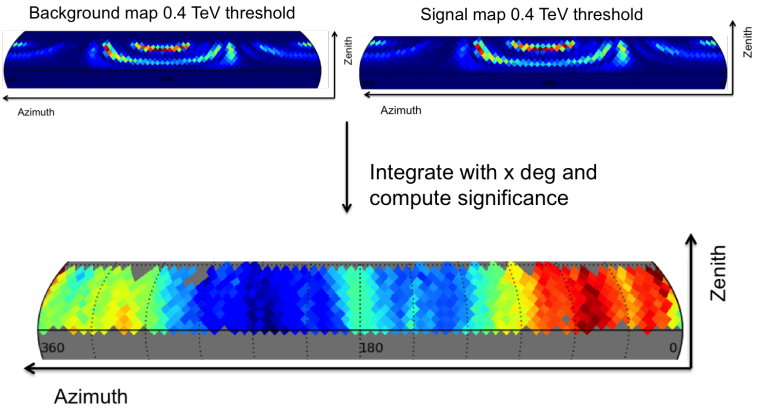

Figure 5.9: Illustration of the S/B1 significance map generation technique for the lowest energy threshold of 0.4 TeV and an integration radius of 90 ° in the horizontal system. The sky map pixels are now heavily correlated. The 90 ° integration radius is most sensitive to the dipole component of the cosmic-ray electron anisotropy

The significance distributions for the uncorrelated sky map pixels show a very good agreement with the Gaussian model function for both S/B1 and B2/B1. The σ values of the best-fit Gaussian models are systematically higher than the expected width of one. The measured widths are however comparable to the ones found in standard H.E.S.S. gamma-ray analyses and indicate that the background description is not perfect. This is very likely due to the coarse zenith angle binning in the lookup tables for the edges of the background regions in BDT-score space. Atmospheric effects play a minor role here, since seasonal effects are not present in the horizontal system. It can therefore be concluded, that in the absence of atmospheric effects the isotropic background can be estimated reasonably well with the presented method.

The comparison of the uncorrelated sky map pixels is very insensitive to large scale anisotropies in the order of tens of degrees due to the small size of the uncorrelated map pixels. The next step in the anisotropy analysis is therefore to correlate the pixels on scales of the expected anisotropy. For this analysis the event counts of both signal and background maps were integrated with a circular kernel of radius $10\,^\circ$, $30\,^\circ$, $60\,^\circ$ and $90\,^\circ$. The distance between two sky map pixels is given by the great-circle distance. An integration kernel of $90\,^\circ$ radius is therefore most sensitive to the dipole component of the potential cosmic-ray electron anisotropy. After the application of the integration routine, the significance maps are generated as in the case of the uncorrelated sky map pixels. The example of the S/B1 significance map with a $90\,^\circ$ kernel for the 0.4 TeV threshold is illustrated in Figure 5.9. Especially in this example remnants of the north-south effect are visible. This effect has an amplitude of $\sim 2\,\%$ and is therefore regarded to be negligible for the equatorial-system analysis.

The significance sky maps for the different integration scales can be reduced to a single quantity that measures the degree of anisotropy between signal and background map. For this work, analog to the procedure in the 2010 Fermi/LAT analysis (Ackermann et al. 2010), this quantity was the highest absolute significance value measured in a single pixel. Since more than one pixel is tested for anisotropy this significance has to be corrected for trial factors. In the case of uncorrelated pixels this trial factor is given by the number of pixels with exposure, in the case of correlated pixels this number will be smaller. The number of trials were not evaluated for the horizontal system, but only for the equatorial system. The trial factor estimation technique will be introduced in the next chapter. However, the significances shown for all integration radii and all energy thresholds in Figure 5.10 are already $< 5\,\sigma$ before trial correction and therefore not significant[1]. Besides the non-detection of a significant anisotropy for all integration radii and energy thresholds, it can be observed that the significance levels of S/B1 and B2/B1 are comparable. This is a hint towards a good isotropy estimation by the background maps and a negligible influence of systematic effects, at least in the horizontal system.

5.6 Anisotropy Analysis in the Equatorial System

Anisotropy Significance Extraction

The anisotropy analysis in the equatorial system was carried out in the same way as for the horizontal system. The S/B1 significance distributions and best-fit Gaussian models in Table

[1] In the IACT community a $5\,\sigma$ detection criterium is usually seen as appropriate and was therefore also used for this analysis.

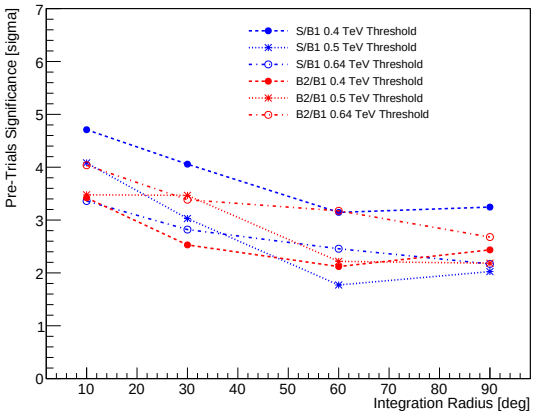

Figure 5.10: Pre-trials anisotropy significances for S/B2 (blue) and B2/B1 (red) as measured for the horizontal system. As a measure of anisotropy the highest absolute significance value of a single pixel was chosen.

5.2 and Figure 5.11 show a systematically larger variance than the ones for the horizontal system. It is furthermore observable that the distributions get wider with decreasing energy. The reason for that behavior can very likely be found in atmospheric effects since this is the biggest difference to the horizontal system with respect to systematics. The signal BDT score distribution is very much peaked towards +1 for high energies, whereas for lower energies the distribution becomes flatter. This effect is best visible in the BDT template fits for the determination of the energy spectrum in Appendix A.3. This change in the shape of the BDT distribution introduces systematics when event energies are misreconstructed to too low (or too high energies) as discussed in Section 5.4. This effect is not caused by the method itself, but by the rather naive energy calibration that neglects atmospheric variations. The B2/B1 significance distributions do not show this behavior. This is expected since in the BDT range of the background maps the BDT shape does not change. Atmospheric variations therefore affect only the absolute flux level of the background maps, which is corrected for by the method discussed in Section 5.4.

The difference to the analysis in the horizontal system is that the pre-trials significances resulting from the integrated anisotropy study were trial-corrected. The trial-factor determination technique introduced by Ackermann et al. (2010) was utilized. The post-trials probability P_{post} is connected to the pre-trials probability P_{pre} via an effective number of trials T_{eff}:

$$P_{post} = 1 - (1 - P_{pre})^{T_{eff}} \tag{5.5}$$

$$T_{eff} = \frac{\log(1 - P_{post})}{\log(1 - P_{pre})} \tag{5.6}$$

Values for T_{eff} have to be determined for every energy threshold and integration radius. In order to do this, fake signal and background sky maps were simulated. The probability density function $P(i)$ of the i-th pixel in both signal and background map is given by a continuous Poisson distribution with mean λ that is set to the number of events in the real data signal map. Both signal and background fake maps were therefore simulated according to the exposure of the real data signal map. The effective number of trials can then be determined by

Energy Threshold [TeV]	S/B1	B2/B1
0.4-4.0 TeV	$\mu = 0.008$ $\sigma = 1.44$ $\chi^2 = 27/19$	$\mu = 0.007$ $\sigma = 1.08$ $\chi^2 = 10/11$
0.5-4.0 TeV	$\mu = 0.027$ $\sigma = 1.33$ $\chi^2 = 11/16$	$\mu = -0.053$ $\sigma = 1.09$ $\chi^2 = 18/14$
0.64-4.0 TeV	$\mu = -0.016$ $\sigma = 1.17$ $\chi^2 = 17/13$	$\mu = -0.011$ $\sigma = 1.00$ $\chi^2 = 12/13$

Table 5.2: Parameters of the best-fit Gaussian models to the significance distributions of the uncorrelated S/B1 and B2/B1 comparison in the equatorial system. Here μ is the mean and σ the width of the Gaussian. Additionally, the reduced χ^2 value is shown.

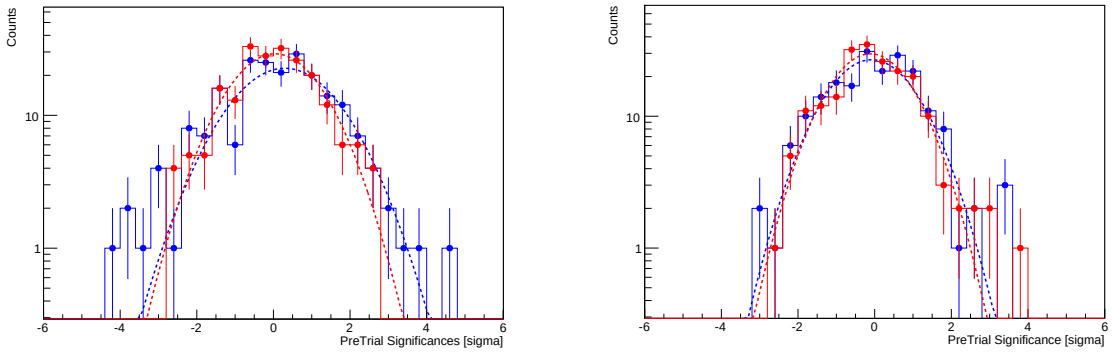

Figure 5.11: Significance distributions for the significance maps determined for S/B1 (blue) and B2/B1 (red) for uncorrelated pixels and the 0.4 TeV (*left*) and 0.64 TeV (*right*) energy threshold in the equatorial system. The distributions are fitted with a Gaussian distribution (dashed lines).

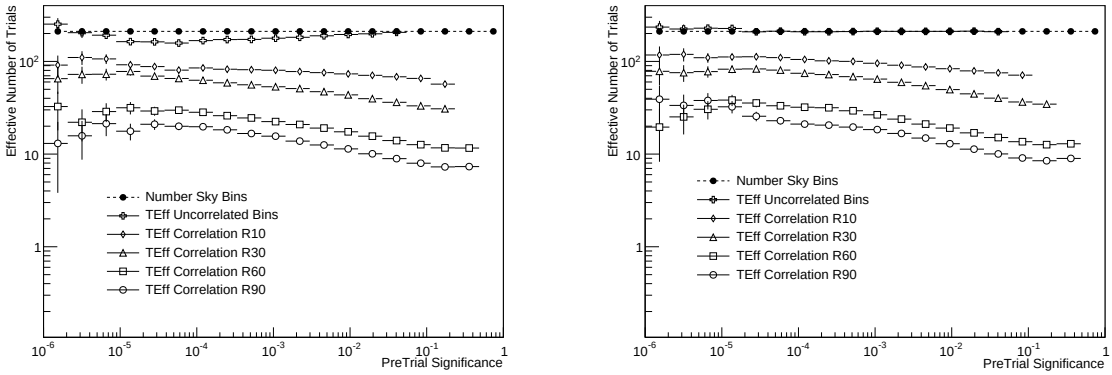

Figure 5.12: Effective number of trials for a pixel exposure given by the signal exposure (*left*) and for constant exposure (*right*) for the 0.4 TeV threshold.

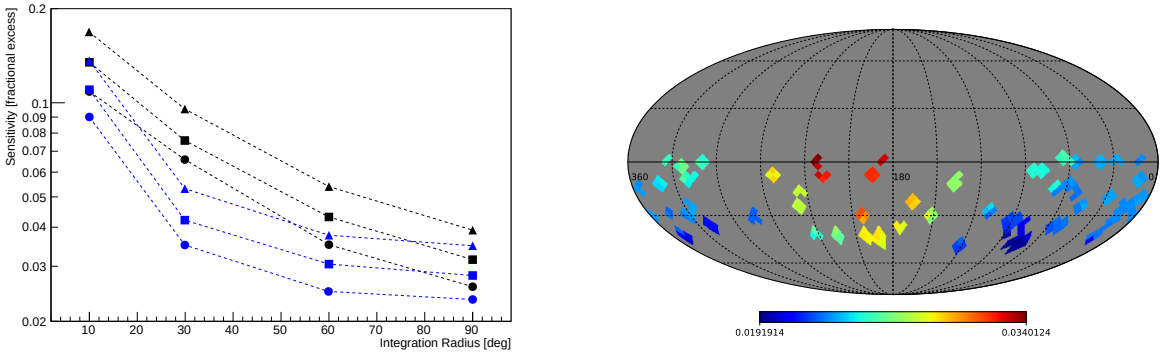

Figure 5.13: Pixel sensitivities (*left*) for a pixel with low (black) and a pixel with high (blue) exposure. The sensitivity is defined as the fractional excess that is needed for a post-trials detection significance of $5\,\sigma$. Additionally, the sensitivity sky map for a $90\,^\circ$ integral kernel and the 0.4 TeV threshold is shown (*right*).

simulating 100000 fake maps, generating the significance maps and counting the fraction of sky maps P_{post} that show at least one pixel with a probability smaller than P_{pre}. By scanning for all P_{pre} values, a T_{eff} lookup can be generated. An example of such a lookup is shown in Figure 5.12 for a 0.4 TeV threshold. Additionally, a T_{eff} lookup built with fake maps with a constant mean value of $\lambda = 1000$ was generated and is also depicted. It is observable that for uncorrelated pixels and a constant mean the effective number of trials is given by the total number of pixels with exposure, as expected. For the non-constant mean the number of trials shows deviations to this expected behavior. This is due to pixels with very low exposure. For larger integration radii the number of trials is decreased due to the increase in correlation among the pixels.

The connection between post-trials and pre-trials significance is solely determined by the knowledge of the effective number of trials. Therefore the pixel-wise fractional excess that is needed for a post-trials $5\,\sigma$ detection of an anisotropy in this pixel can be determined given a specific integration radius. The fractional excess f^i in the i-th pixel with N^i_{sig} signal events and N^i_{bkg} background events is defined as:

$$f^i = \frac{N^i_{sig} - N^i_{bkg}}{N^i_{bkg}} \tag{5.7}$$

Pixels with high exposure are more sensitive compared to ones with low exposure. This is shown in Figure 5.13 for the example of two pixels, one with low and one with high exposure. For anisotropies of $10\,^\circ$ angular scale the measured fractional excesses have to be in the order of $\sim 10\,\%$ in order to be detectable. For scales of $90\,^\circ$ a few percent are sufficient. The detectability of an anisotropy of small angular scale will therefore depend heavily on the position of the anisotropy. In the case of a dipolar anisotropy this is also the case, but not due to a low or high exposure of single pixels, but only due to the pointing pattern of the runs.

The post-trials anisotropy significances for both S/B1 and B2/B1 and all energy thresholds are shown in Figure 5.14. Two general statements about these result can be made:

- No anisotropy is detected for all integration radii and for all energy thresholds. Smaller integration radii and lower energies show a systematic increase in deviation from isotropy.

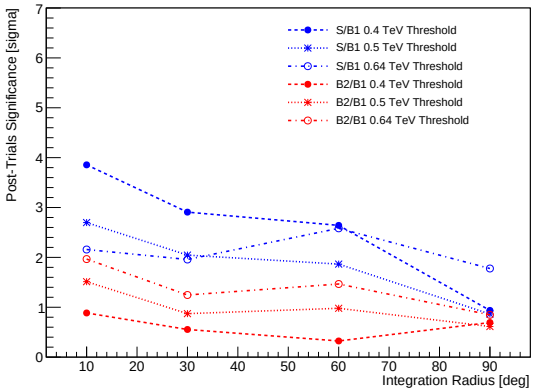

Figure 5.14: Post-trials anisotropy significances for S/B1 (blue) and B2/B1 (red) as measured for the equatorial system. As a measure of anisotropy the highest absolute significance value of a single pixel was chosen.

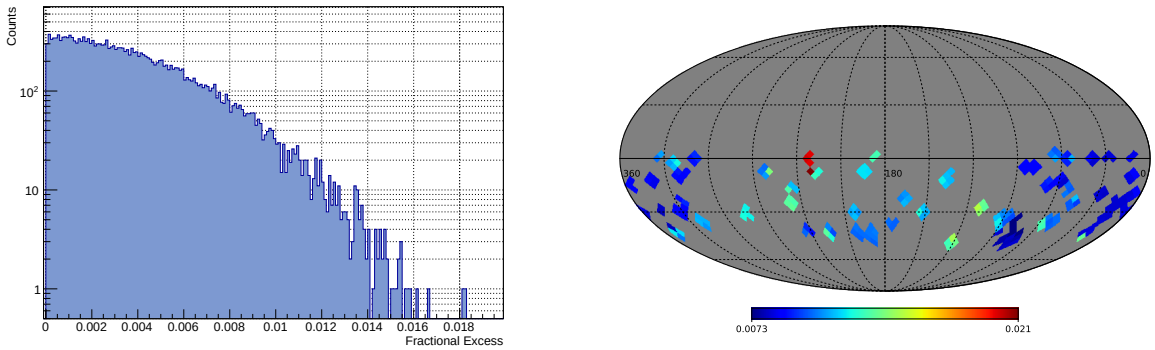

Figure 5.15: Fractional excess distribution for a single pixel as determined with simulated signal and background maps for the 0.4 TeV energy threshold (*left*). Upper limit sky maps on the fractional excess are determined as the 95 % quantile value (*right*).

This is either due to real anisotropies or due to imperfect background maps. Atmospheric effects, already visible in the significance distribution of uncorrelated pixels, could induce this level of systematics.

- The significance level of S/B1 is systematically higher than the one of B2/B1 in contrast to the results of the horizontal system. This effect is especially strong for small integration radii. This is a strong hint towards systematic effects that dominate for small integration radii. For large integration radii the atmospheric condition is similar for all pixels. It is therefore not recommended to use this analysis method for small scale anisotropies without an adapted energy calibration. The following steps of the analysis will concentrate on the dipole component of the anisotropy.

Since no anisotropy was detected, upper limits on the fractional excess for the 90 ° integration radius were determined. The upper limits are determined pixel-wise. They were determined by simulating signal and background maps like in the case for the trial factor extraction, only that this time the mean value of the Poisson probability distribution for signal and background maps were given by the real data signal and background map pixel counts, respectively. Upper limits can then be extracted by determining the 95 % quantile of the resulting fractional excess distribution in every pixel. An example of such a fractional excess distribution for one pixel and the resulting upper limit map for the 0.4 TeV threshold is shown in figure 5.15.

Determination of the Dipole Amplitude Upper Limit

An upper limit on the 90 ° fractional excess itself is not interesting from an astrophysical point of view. Due to the mixture of electrons and protons in the signal map and the very sparse coverage of the sky no immediate connection to a dipole component induced by a nearby astrophysical source can be drawn. The direction of the induced dipolar anisotropy is defined as the direction of maximum intensity. However, by utilizing a set of (rather strict) assumptions, the upper limits on the fractional excess can be translated to an upper limit on the amplitude of a dipolar anisotropy. The assumptions are the following:

- The cosmic-ray electron flux in the covered energy range is dominated by a single source. This is a well-justified assumption, because most astrophysical cosmic-ray electron models either predict a dominating Vela SNR/PWN or Monogem/Geminga. Monogem and Geminga are seen as one source in this analysis due to the coarse sky map binning.

- The electron fraction in every sky pixel is known. While the correct electron fractions are not known, the electron fraction lookups defined in Section 5.3 are expected to give good estimators. The absolute scale of the electron fraction has an uncertainty of $\sim 10\,\%$ that is extracted out of the difference between the two hadronic interaction models.

- Sky maps following a dipolar event distribution can be simulated with the same systematics as the real data maps. This is certainly not true for the simulation of atmospheric effects, but these effects are regarded negligible for an integration radius of 90 °. The biggest complication comes due to the fact that the edge lookups for the background maps were determined in zenith angle bins. The average pointing position and therefore the visible part of the potential dipolar anisotropy differs from bin to bin. This will ultimately lower the sensitivity to a dipolar anisotropy, because the background will

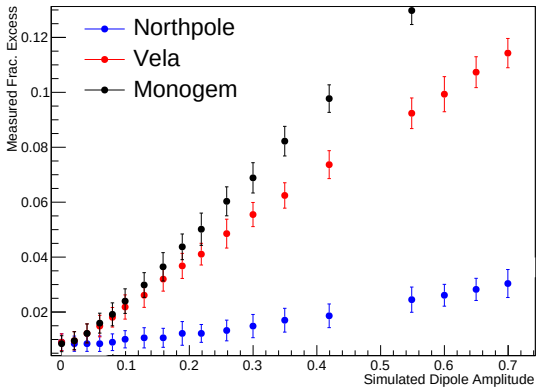

Figure 5.16: Calibration lookups for the dipole amplitude-to-measured fractional excess conversion for a single pixel and three source directions. The analysis is insensitive to dipole sources located in the vicinity of the poles.

partially follow the signal. This effect was taken into account for the simulation of both signal and background maps.

The basic idea of the translation technique is to simulate both signal and background maps in the presence of a perfect dipolar anisotropy. The event number in every pixel i is evaluated for a Poissonian probability distribution with mean λ^i_{sig} and λ^i_{bkg} respectively. The mean values are determined following Equations 5.8 and 5.9.

$$\lambda^i_{sig} = N^i_{sig} \cdot \left(1 + \delta \cdot \cos(\Theta^i) \cdot \epsilon^i_{sig}\right) \tag{5.8}$$

$$\lambda^i_{bkg} = N^i_{sig} \cdot \left(1 + \delta \cdot \cos(\Theta^i) \cdot \epsilon^i_{bkg} + \delta \cdot \cos(\Theta^i_{norm}) \cdot \epsilon^i_{norm}\right) \tag{5.9}$$

Here N^i_{sig} is the number of signal counts in the i-th pixel, δ the dipole amplitude, Θ^i the great-circle distance to the maximum of the dipole and $\epsilon^i_{sig}/\epsilon^i_{bkg}$ the signal and background electron fractions respectively. Θ^i_{norm} and ϵ^i_{norm} are given by the mean great-circle distance and electron fraction of the background normalization position in the equatorial system.

Dipolar anisotropies are simulated for all directions on the equatorial sky maps. The direction of a pixel is defined as the coordinate of its center. The anisotropies are simulated for amplitudes of $\delta = 2, 4, 6, 8, 10, 15, 20, 30$ and $50\,\%$. The significance maps are generated out of the simulated signal and background maps and the fractional excess in each pixel with exposure is evaluated. An example of the resulting dipole amplitude-to-fractional excess calibration curves for a single pixel is shown in Figure 5.16. A dipole direction is defined to be detected as soon as it induces a fractional excess that exceeds the $95\,\%$ confidence level value in a **single** pixel. With this technique dipole anisotropies can be detected even for directions without any exposure. The resulting all-sky upper limit maps are shown in Figure 5.18. The upper limits of the dipole amplitudes for the directions of Monogem/Geminga and Vela together with a comparison to the Fermi/LAT upper limits are shown in Figure 5.17. The shaded error band of the upper limit is due to the assumed $10\,\%$ error on the electron fractions. The Cygnus Loop direction is not tested here, because its contribution to the dipole anisotropy is expected to start at higher energies.

The all-sky upper limit maps in Figure 5.18. show a very inhomogeneous pattern. The analysis is insensitive at both North and South-pole and cannot constrain the dipole amplitude to

a meaningful value. This behavior is due to the pointing pattern of the runs. The very tight zenith angle cut of $\leq 25\,^{\circ}$ restricts the accessible part of the sky to a narrow band in equatorial coordinates. Dipole positions that are very close or inside this bands can be tested very efficiently, because the dipole is sampled at both its maximum and minimum position. This is not the case for dipole positions in the vicinity of the poles. A second experiment covering the northern hemisphere like VERITAS would very likely reduce this effect. Fortunately the most interesting source candidates are located very close to the covered sky band and can be tested efficiently. The resulting upper limits for both Vela and Monogem/Geminga can however not compete with the analysis performed with Fermi/LAT. Nevertheless the H.E.S.S. upper limits are the first derived from IACT data in this energy range and confirm the non-existence of any large dipole anisotropy. The second positive aspect is that the method presented has great capabilities to be used for higher energies. Energy ranges $> 4\,\mathrm{TeV}$ have not been tested so far. In order to achieve this the analysis chains ImPACT-MSSG or Model++ would have to be used. This is possible in principle, since the analysis method itself does not depend on the kind of input events. It only requires signal and background maps, the specific way of generating these maps is not important. However, this was not possible for this work due to time constraints.

In general this analysis has shown that it is possible for an IACT to do anisotropy studies without relying on the exact knowledge of the effective areas. Despite systematic disadvantages with respect to satellite experiments it is furthermore possible to constrain cosmic-ray electron anisotropies on the percent scale. The usability of the presented method is not bound to cosmic-ray electrons, but could in principle be used for anisotropy studies of diffuse gamma-ray background. Both gamma-ray and electron anisotropy analysis will be most interesting for the upcoming CTA experiment due to the large coverage of the sky by the CTA sites, situated at the northern and southern hemisphere.

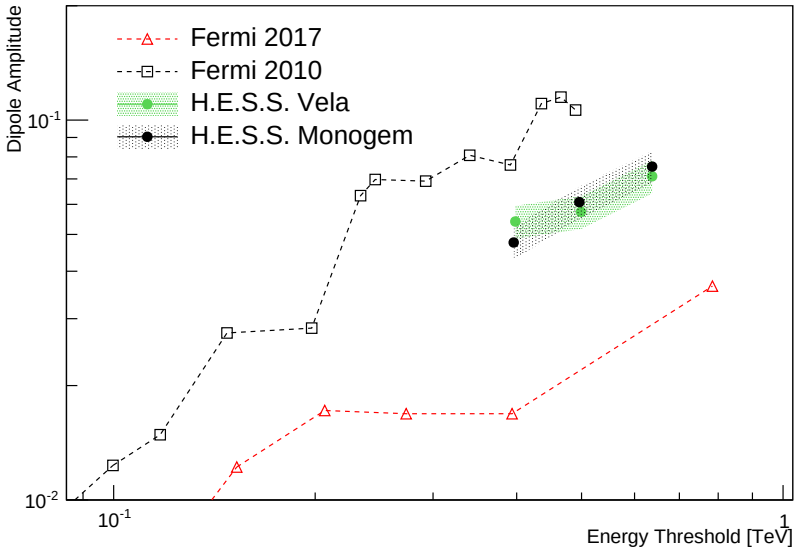

Figure 5.17: 95 % confidence level upper limit on the dipole amplitude for the direction of Vela and Monogem as extracted by this work. The shaded band reflects the uncertainty on the electron fraction in the signal region as determined by the difference between the two hadronic interaction models. Additionally the 2010 and 2017 upper limits from Fermi/LAT are shown (Ackermann et al. 2010; Abdollahi et al. 2017a).

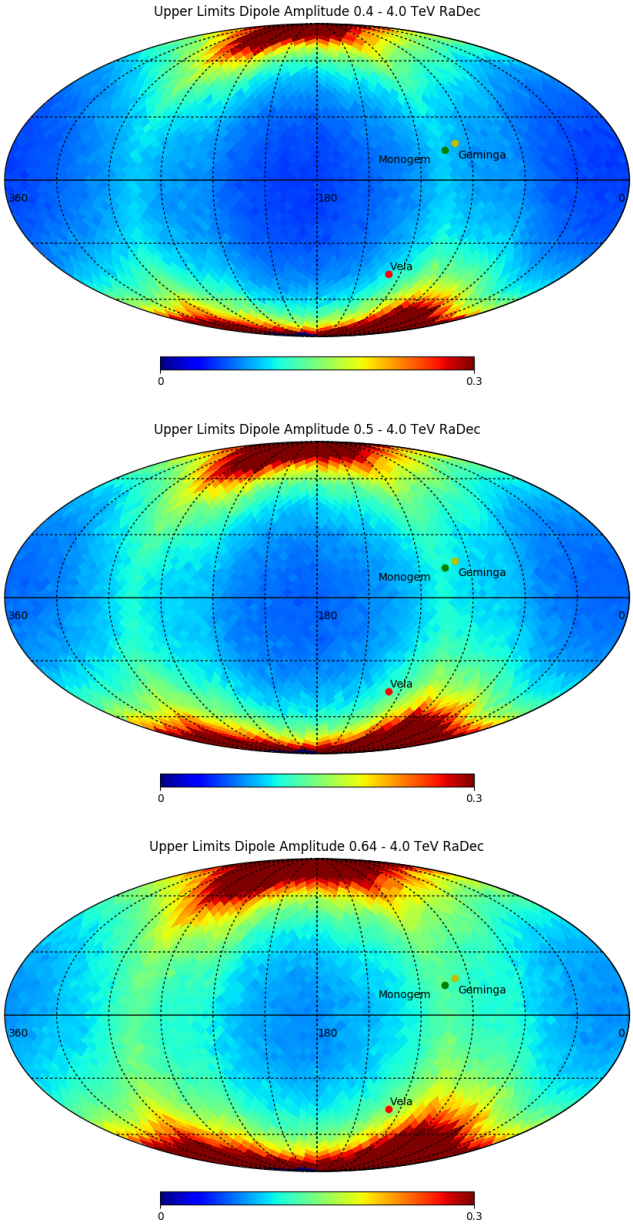

Figure 5.18: 95 % confidence level upper limit sky maps of the dipole amplitude for all three energy thresholds. The value in each pixel is the upper limit of the dipole amplitude assuming a source in the direction of the pixel center.

CHAPTER 6

Inspection of Local Cosmic-Ray Electron Emitters

The anisotropy analysis based on the generation of isotropic background maps has proven to work well for the study of dipolar anisotropies. This method was invented to overcome the necessity of the knowledge of the cosmic-ray electron effective areas. Nevertheless the topic of this chapter is the search for dipole anisotropies by using the usual Monte Carlo effective areas and calculating fluxes. The two anisotropy study methods shall then be compared with respect to the dipole amplitude upper limits. Anisotropies of smaller scales are not discussed here. The most important part of this study was the extraction of a reasonable systematic error on the measured electron flux. Only three specific dipole directions were tested (Vela, Monogem, Geminga) in this study since these are the most interesting source positions that are close to the covered coordinate band on the equatorial sky.

The method itself will be introduced in Section 6.1, followed by a discussion about the determination of the systematic error on the effective areas in Section 6.2. The dipole analysis results will be presented in Section 6.3. For this analysis **ZetaBDT − Fit** has been used. The cross-check results for Model++ for the dipole analysis are shown in the Appendix A.5.

6.1 Method

The dipole anisotropy analysis in this chapter can be separated in the following steps:

- Like in the case of the all-sky analysis, the analysis is carried out for three energy thresholds 0.4, 0.5 and 0.64 TeV. The upper energy limit is again 4.0 TeV.

- Circular regions with a great-circle radius of 20 ° are defined in the equatorial system. Each run is assigned to only one of those regions in an automated way. After all runs have been sorted into one of the regions, the mean rectascension and declination coordinate for each region is evaluated. The exact shape of the regions is therefore not important. The results of only one realization of the sorting routine is discussed here. It was checked that different realizations give compatible results.

- Events classified as signal-like ($\zeta_{BDT} \geq 0.79$) are filled into their associated sky regions. The same event-wise atmospheric flux correction is applied like for the all-sky analysis. The number of electrons in each region is determined using the BDT template fit technique. The big sky regions are necessary to achieve enough statistics for the fit. The cosmic-ray electron flux is evaluated using Equation 3.10. Only one hadronic interaction model is used here, because in first order they only differ on the absolute flux level.

- A dipole model is fit to the flux data points for source directions pointing towards Vela, Monogem and Geminga using a simple χ^2 minimization. Prior to this minimization the systematic error on the electron flux has to be determined.

- In the case of a non-detection of a significant dipole anisotropy, upper limits on the dipole amplitude were determined.

A possible advantage of this method with respect to the all-sky analysis is the direct determination of the number of electrons in each sky region by the fit technique. The electron fractions are therefore measured and not approximated by lookups.

$$\chi^2 = \sum_{i}^{i \leq N_{Regions}} \frac{\left(F_i - F_i^{model}\right)^2}{\sigma_{sys}^2 + \sigma_e^2} \tag{6.1}$$

The χ^2 function used in the minimization process is given by Equation 6.1. Here F_i is the flux measured in region i, F_i^{model} the flux predicted by the dipole model, σ_{sys} the systematic flux error and σ_e the flux error given by the minimizer (MINUIT+MINOS) itself. The dipole model for the electron flux is stated in Equation 6.2.

$$F_i^{model} = F_{mean} \cdot (1 + \delta \cos \Theta_i) \tag{6.2}$$

F_{mean} is the mean flux level for the whole sky, δ the dipole amplitude and Θ_i the great-circle distance of the region center i to the maximum of the dipole model.

6.2 Determination of the Flux Systematic Error

In order to perform the χ^2 minimization a reasonable value for the systematic flux error σ_{sys} has to be determined. The systematic error can only by evaluated with the help of the signal data itself. In principle another idea would be to determine σ_{sys} for gamma-like protons with $\zeta_{BDT} < 0.79$. Since it is not known a priori if the effective areas of gamma-like protons and electrons show the same trends with respect to changing observational conditions, proton simulations would have to be generated for several conditions. This was simply not doable within the time constraints of this work.

In order to use the cosmic-ray electron flux itself to constrain the systematic error, the data set was split into several parts depending on an observational parameter that is insensitive to a potential anisotropy. A split into zenith or azimuth angle bins would very likely be sensitive to the systematic flux error, however it might be possible that anisotropies are not completely washed out in the horizontal system. A better suited observational parameter is the year a particular run was taken. Even in the case of a strong anisotropy, the flux integrated over one year should be constant in time since the accessible part of the sky (in the equatorial system)

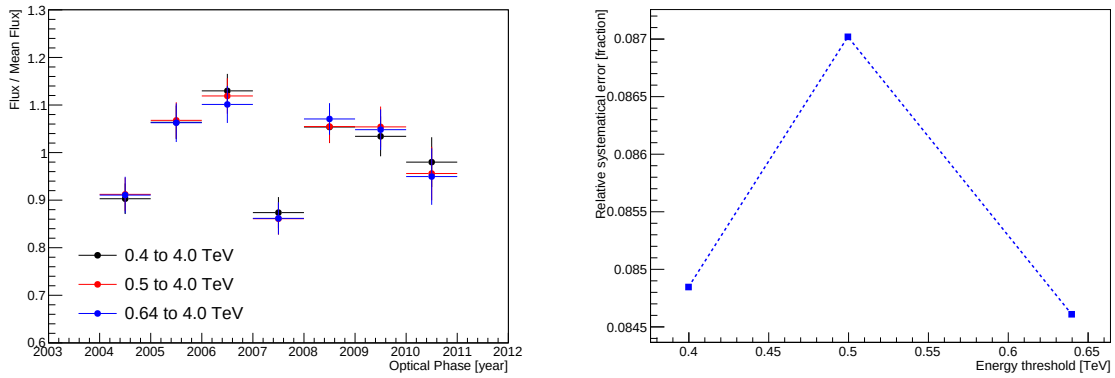

Figure 6.1: Measured cosmic-ray electron flux as a function of the observation year (*left*). The flux data was fit with a constant and the systematic error on the flux was increased until the data was compatible with the constant model. The resulting relative flux error is shown on the (*right*).

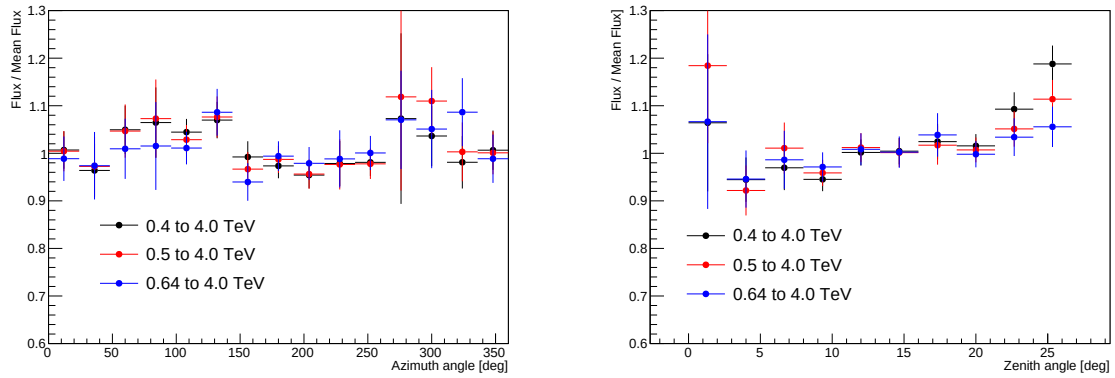

Figure 6.2: Measured cosmic-ray electron flux in zenith (*left*) and azimuth angle (*right*) bins. The flux varies within the $\sim 8\,\%$ systematic flux uncertainty determined with the yearly data split.

changes with a period of one year. It is assumed that the pointing strategy does not change from one year to another.

In Figure 6.1 the cosmic-ray electron flux as a function of the observation year, determined with the BDT template fit technique, for all energy thresholds is shown. The errors on the data points are the ones given by the minimizer. A strong variation exceeding the minimizer error is observable. Interestingly the electron flux seems to change monotonically within one optical Monte Carlo phase (1b: 2004 to early 2007, 1c: 2007 to 2011) and shows a huge variation in the last year of phase 1b. This is a distinct hint towards a non-perfect muon correction for the effective areas (and maybe even the energy calibration). The value of the systematic flux error has been determined by fitting a constant to the measured flux and increasing the collective relative systematic flux error until the constant model fits the data (reduced $\chi^2 == 1$). The resulting relative systematic errors for all energy thresholds are shown in Figure 6.1. The relative error value of $\sim 8\,\%$ is similar to the flux error determined for the first H.E.S.S. Crab Nebula publication (Aharonian et al. 2006). In Figure 6.2 the cosmic-ray electron flux in different zenith/azimuth angle bins is shown. The flux is compatible with a constant within the $8\,\%$ systematic error.

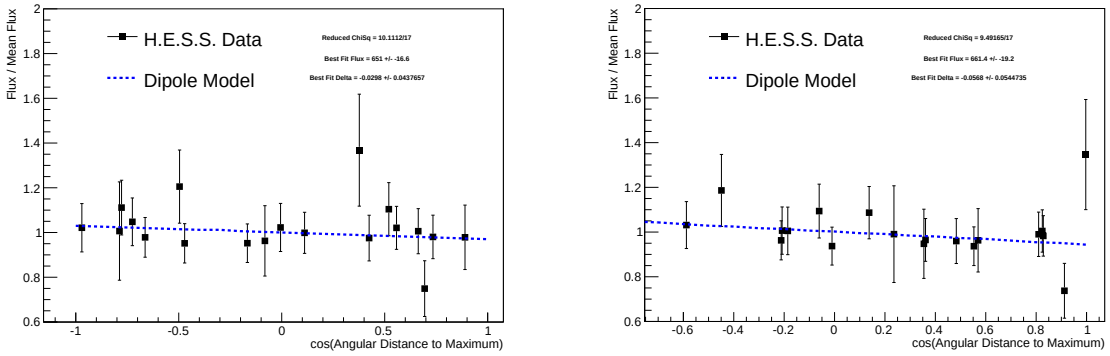

Figure 6.3: Best-fit dipole models for the 0.4 TeV threshold for the direction of Geminga (*left*) and Vela (*right*). The complete collection of dipole model fits can be found in Appendix A.4.

6.3 Dipole Analysis Results

The null hypothesis for the anisotropy analysis is given by a perfect isotropy of the electron flux. In order to determine the best-fit constant electron flux F_{mean}, the dipole amplitude δ has been fixed to zero. The flux model function F_i^{model} therefore had only one free parameter. The resulting minimum χ^2_{Iso} value was compared to the χ^2_{Dipole} value of the best-fit dipole model (two free parameters) in terms of a $\Delta\chi^2$-test. The $\Delta\chi^2$ value is defined as the difference in χ^2 values for a null and an alternative hypothesis (dipole model). The definition is shown in Equation 6.3. The $\Delta\chi^2$ should be distributed according to a χ^2 distribution with one free parameter for this particular case. The $\Delta\chi^2$-test does not take into account that data points are in general better described by models with more free parameters. Nevertheless if an alternative model is insignificant for the $\Delta\chi^2$-test it will also be insignificant for a more advanced statistical analysis method.

$$\Delta\chi^2 = \chi^2_{Iso} - \chi^2_{Dipole} \tag{6.3}$$

If the $\Delta\chi^2$ value is known the s.c. p-value can be determined. It is defined in Equation 6.4 as the probability that a particular measured value $\Delta\chi^2_{meas}$ is compatible with a statistical fluctuation of the null hypothesis assuming a probability distribution $P(\Delta\chi^2)$. In this case $P(\Delta\chi^2)$ is given by a χ^2 distribution with one free parameter. Small values of p will lead to a rejection of the null hypothesis.

$$p(\Delta\chi^2_{meas}) = 1 - \int_{-\infty}^{\Delta\chi^2_{meas}} P(\Delta\chi^2)\mathrm{d}\Delta\chi^2 \tag{6.4}$$

In Figure 6.3 an example for fits of the dipole model to the data are shown for the lowest energy threshold for the directions of Geminga and Vela. The complete results for the model fits can be found in Appendix A.4. The best-fit dipole amplitudes and corresponding p-values are summarized in Table 6.1 together with the values for χ^2_{Dipole}. Both models are in general in good agreement with the data for all tested directions and energy thresholds. The best-fit dipole amplitudes are always smaller than 6 %. The improvement in χ^2 from the isotropy model to the dipole model is insignificant for all sources and energies. Since no significant dipole anisotropies were detected, upper limits on the dipole amplitude can be derived. The upper limits were derived by increasing the amplitude δ from zero in the dipole model until

Source Name	Energy Threshold	Best-fit δ	p-Value	Upper Limit δ	Reduced χ^2_{Dipole}
Vela	0.4 TeV	-0.056	0.29	0.060	9.5/17
	0.5 TeV	-0.058	0.31	0.065	6.5/17
	0.64 TeV	-0.048	0.42	0.072	6.7/17
Geminga	0.4 TeV	-0.029	0.49	0.061	10/17
	0.5 TeV	0.024	0.60	0.070	7.2/17
	0.64 TeV	0.029	0.54	0.069	7.0/17
Monogem	0.4 TeV	-0.032	0.45	0.059	10/17
	0.5 TeV	0.027	0.55	0.067	7.2/17
	0.64 TeV	0.030	0.52	0.067	7.0/17

Table 6.1: Best-fit dipole amplitudes, p-values and upper limits for all tested directions and energy thresholds.

the $\Delta\chi^2_{Dipole}(\delta)$ reaches the 95 % containment level of its probability distribution function. See Equation 6.5 for a definition. The upper limit values are stated in Table 6.1 and are compared to the upper limits derived with the all-sky method for the directions of Vela and Monogem in Figure 6.4.

$$\Delta\chi^2_{Dipole}(\delta) = \chi^2_{Iso} - \chi^2_{Dipole}(\delta) \stackrel{!}{=} 3.814 \tag{6.5}$$

The comparison of the dipole amplitudes show a good agreement within both methods given the systematic uncertainty on the all-sky upper limits. The fit method seems to be performing very well in the case of a good coverage of the dipole model, as is the case for all three tested source positions. Source positions far of the covered sky coordinate band will suffer from the same pointing pattern effects as the all-sky method. In general one could therefore state that the two methods perform the same for the three tested directions with respect to sensitivity to a dipole anisotropy. However, it is not known, if the estimate of the systematic flux error is correct. Underrating this error would lead to a too restrictive dipole amplitude upper limit, overrating would lead to a reduced sensitivity. The fact that the systematic error is similar to the one determined for the Crab nebula analysis is however a hint towards a reasonable estimation.

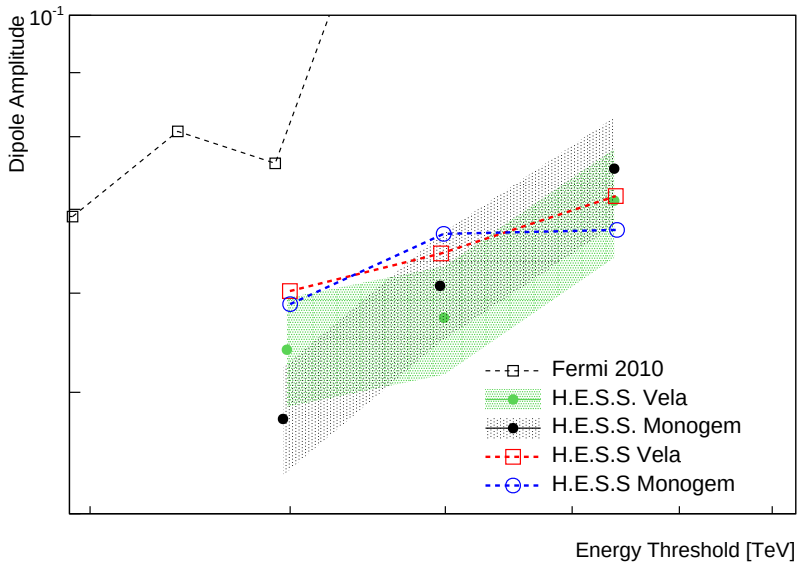

Figure 6.4: Upper limits on the dipole amplitude as determined by the all-sky and dipole fit method for the directions of Vela and Monogem. Additionally the 2010 dipole upper limits from Fermi/LAT are shown (Ackermann et al. 2010).

CHAPTER 7

Discussion

The interpretation of both the electron spectrum and the anisotropy results has to be separated into an astrophysical source scenario and a dark matter scenario since both scenarios can explain the rise in the positron fraction. The astrophysical source scenario will be discussed in detail in the following. The dark matter scenario will not be discussed in this work. The only possibility to distinguish between a dark matter scenario and an astrophysical source scenario is the detection of a sharp feature in the electron spectrum induced by an astrophysical source and/or a detection of a dipole anisotropy on the percent level. Since for a dark matter scenario and a PWN scenario very low amplitudes for the dipole anisotropy are predicted, the present knowledge about the electron anisotropy is not sufficient to distinguish between both scenarios. One of the measurements that could help to distinguish between both scenarios is an extension in energy of the positron fraction measurement. This measurement will very likely be provided by the satellite experiments DAMPE and CALET in the near future.

Under the assumption that the cosmic-ray electron flux in the GeV-TeV energy range is generated by astrophysical sources like SNRs or PWNe, the measured electron spectrum from this work will be compared to source models derived by Manconi et al. (2017). Electron spectrum models that predict an upturn in flux in the high energy regime, for example discussed by (Hinton et al. 2011) or (Kobayashi et al. 2004), are not discussed here since they are considered to be rejected by the measured H.E.S.S. spectrum. Three different source models are discussed by Manconi et al. (2017). All models have in common a secondary component of cosmic-ray electrons and positrons produced by spallation and a contribution from a far population of SNRs (source distances greater than 0.7 kpc) that determines the shape of the electron spectrum at GeV energies. The models were fit to the measured AMS-02 combined cosmic-ray electron spectrum and the positron spectrum in a combined fit. In the following the differences of the source models are discusssed.

1. The first model assumes a dominant role of the young Vela SNR for the shape of the electron spectrum at TeV energies. The contribution of this source is therefore treated as an individial component in the fit. The contributions of other SNRs with source distances smaller than 0.7 kpc are treated as a single “Near SNR” component in the fit, which is mainly determined by the powerful Cygnus SNR. A combined PWN component

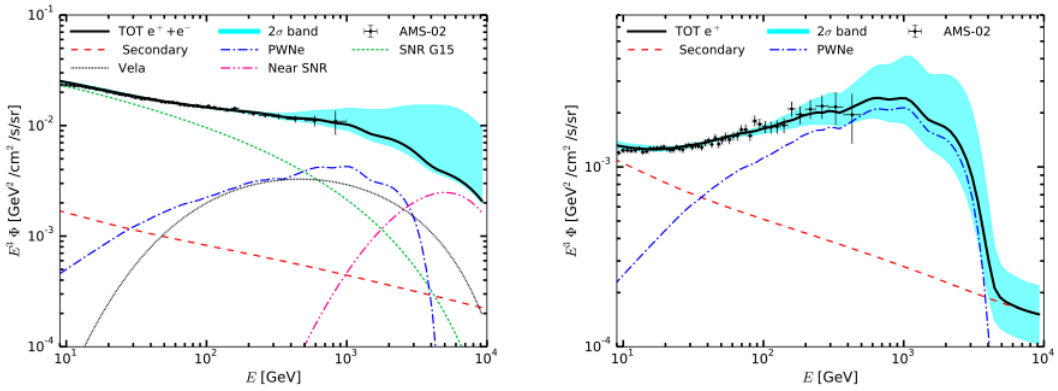

Figure 7.1: Combined source model fit to the AMS-02 electron plus positron (*left*) and positron (*right*) spectrum by Manconi et al. (2017). The model shown as dominating Vela SNR (black) and a near SNR component (pink) in the GeV-TeV range. The positron flux is explained by a PWN component (blue) and a secondary component (red). The low energy part of the spectrum is determined by a smooth, distant SNR component (green). Picture taken from Manconi et al. (2017).

with sources taken from the ATNF catalog is used to explain the measured positron spectrum.

2. The second model neglects all known SNRs with distances smaller than 0.7 kpc. Instead a very old SNR that is no longer visible in the electromagnetic bands, but which electrons still contribute to the measured flux at Earth, is responsible for the shape of the electron spectrum at TeV energies. A combined PWN component is again used to explain the measured positron spectrum.

3. The third model is similar to the first model and also assumes a strong role of the young Vela SNR by modelling its contribution as an individual component. However in this model it is assumed that a single PWN (Monogem or Geminga) dominates the PWN contribution to the positron spectrum and also determines the shape of the high energy part of the electron spectrum.

The injection spectra of all involved sources are modelled by a single power law with an exponential cutoff at 5 TeV. This rather low value for the cutoff energy, with respect to cutoff energies of 20 TeV discussed by (Kobayashi et al. 2004), is one of the reasons for the shift towards lower energies of the Vela SNR spectrum. Higher cutoff energies induce a flux upturn at high TeV energies when assuming a dominant role for the Vela SNR. A combined fit to the AMS-02 electron and positron spectra is exemplarly shown for the first source scenario in Figure 7.1. This figure is taken from Manconi et al. (2017).

In the following the best-fit models of all three scenarios are discussed in the context of the results of this work. The measured H.E.S.S. electron plus positron spectrum was compared to the best-fit models of all three scenarios. In addition the expected electron dipole anisotropy amplitudes derived by Manconi et al. (2017) for the three source models were compared to the upper limits derived in this work and with Fermi/LAT (Ackermann et al. 2010; Abdollahi et al. 2017a).

In Figure 7.2. the models for the combined electron plus positron spectrum for all three source scenarios are shown together with the measured AMS-02 and the H.E.S.S. electron spectrum.

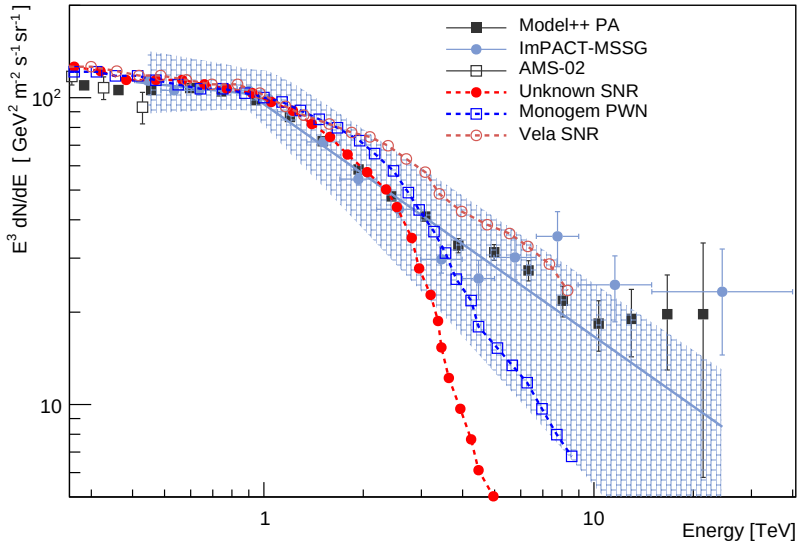

Figure 7.2: AMS-02 and H.E.S.S. electron spectra with the three source models derived by Manconi et al. (2017). The scenario of an unknown, old SNR without electromagnetic counterpart is disfavored by the measured H.E.S.S. electron spectrum.

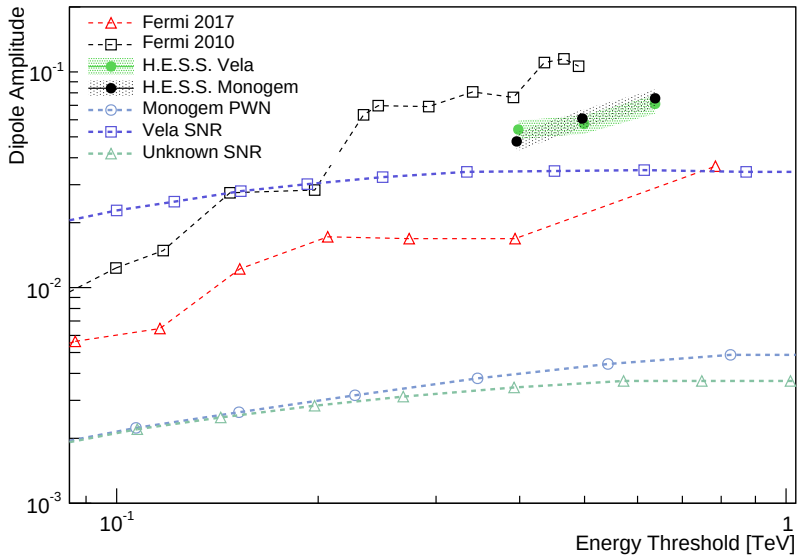

Figure 7.3: Measured H.E.S.S. and Fermi/LAT upper limits on the dipole anisotropy amplitude. Additionally the predicted dipole amplitudes as derived by Manconi et al. (2017) for all three discussed source scenarios are shown.

The name of the models refers to the source that mainly shapes the high energy part of the electron spectrum, for model 1 this is the Vela SNR, for model 2 the unknown SNR and for model 3 the Monogem or Geminga PWN. All three models are in excellent agreement with the H.E.S.S. electron spectrum for energies below the spectral break at 900 GeV. However, only the first and the third model describe the measured H.E.S.S. spectrum above energies of 1 TeV reasonably well. The scenario of Geminga as the dominant PWN leads to very similar results as the Monogem scenario. It is not possible to distinguish between scenario 1 and 3 given the large systematic error on the H.E.S.S. spectrum. Nevertheless the Vela model predicts a harder index after the spectral break and therefore fits better to the measured H.E.S.S. spectrum. In the scenario of a dominant unknown (and rather old) SNR the predicted flux shows a softer spectral index after the spectral break compared to the other scenarios due to the longer exposure to radiative cooling processes. The best-fit values for the source age and distance of this unknown SNR are 0.36 ± 0.06 kpc and 144 ± 9 kyr. In summary the H.E.S.S. electron spectrum favors the scenario of the Vela SNR shaping the TeV energy range of the electron spectrum, but also the PWN scenario is compatible with the measured spectrum.

A completely different picture arises when the resulting dipole anisotropies of all three models are compared to the upper limits on the dipole amplitude derived in this work and with Fermi/LAT. The first scenario of a dominant Vela SNR is disfavored by the very stringent upper limits from Fermi/LAT. For the Monogem/unknown SNR scenario much lower anisotropy amplitudes are predicted that are not within reach of current instruments. In summary the combined picture of spectrum plus anisotropy favors the Monogem/Geminga scenario. Given the low predicted dipole anisotropy values for the PWN scenario it is very unlikely that the current generation of satellite experiments or IACTs will be able to detect a significant anisotropy. However, given that with DAMPE, CALET and CTA three experiments sensitive to the detection of cosmic-ray electrons are planned for the near future, this statement could soon prove to be outdated.

Part II:

Characterization of a Readout System for the SST Cameras of CTA

Preface

Imaging air Cherenkov telescope (IACT) arrays like H.E.S.S., VERITAS and MAGIC have proven their scientific worth in the past with respect to detecting cosmic rays and gamma rays in the GeV to TeV energy range. In difference to satellite experiments like Fermi/LAT and AMS-02 they provide a large enough effective area to compensate for the steeply falling particle flux spectra. The IACT particle detection technique exploits the fact that cosmic rays and gamma rays induce air showers in the atmosphere, that can be detected by their emitted Cherenkov light. In order to reliably detect these nanosecond light flashes the camera of an IACT has to feature a very low exposure time and a fast photodetector signal readout. The basic working principle of such a camera can be reduced to simple photoelectron counting. One of the key performance indicators of the camera is thus given by the uncertainty assigned to the number of photoelectrons counted in each camera pixel. This performance can be quantified by the s.c. "charge resolution". The abstract value of the charge resolution is directly connected to the energy resolution of a Cherenkov event. For the standard energy calibration, introduced in Part 1 of this work, charge resolution and energy resolution are considered to be directly proportional. For more sophisticated and advanced energy reconstruction methods the connection is not that simple anymore, but the proportionality remains.

Besides external contributions like the Poisson-limit and contributions from the photodetector itself, the charge resolution of a Cherenkov camera is mainly determined by the performance of the readout system. The development of a high-performance and reliable readout electronics is in principle not very difficult since a huge variety of industrial components is available. The difficulty comes in the form of cost efficiency. Future IACT arrays like the upcoming Cherenkov Telescope Array (CTA) will consist of dozens of telescopes, each with hundreds of pixels. In order to be affordable, readout solutions specifically developed with a low cost per readout channel have to be developed. The TARGET 7 readout system, to be characterized in this work, is an example of a readout system that has been designed with cost efficiency in mind. This system is envisaged to be used for some of the CTA telescope cameras and will be analyzed in this work with respect to its charge resolution performance. The major goal of this characterization was to extract recommendations for the next TARGET generation.

The TARGET 7 characterization in this work is structured as following: In the first chapter, an introduction to CTA will be given and the requirements for a CTA readout system

will be stated. The second chapter will introduce the TARGET 7 readout system and the future TARGET generation. The third and fourth chapter are dedicated to the electrical performance and the charge resolution performance, respectively. A conclusion will be given in Chapter 5.

CHAPTER 1

The Cherenkov Telescope Array CTA

The Cherenkov Telescope Array (Acharya et al. 2013) will be the next generation ground based gamma-ray observatory in the very high energy regime. In contrast to the predecessor IACTs like VERITAS or H.E.S.S., the observatory will be split into two arrays of different size. The larger array will be located on the southern hemisphere near the Paranal Observatory in Chile and the smaller one will use the site of the Observatorio del Roque de Los Muchachos on the La Palma island in Spain. The CTA consortium, which main task is to provide the technology to built CTA and to define the science goals, is a multinational organisation with more than 1000 active scientists, technicians and project managers. Once CTA will be completed, the CTA Observatory GmbH will take over the responsibility of the routine operation and maintenance. CTA will be the first open, proposal-driven observatory for the gamma-ray astronomy. The data will be publicly available which will certainly boost the scientific output of CTA.

In Section 1.1 the general characteristics and layout of CTA will be introduced. Since all contributions from the consortium to CTA will be given as in-kind contributions, requirements on all components (telescope structure, camera, optical system) had to be provided by the observatory. The requirements for the cherenkov camera for small-sized telescopes will be stated in Section 1.2. These requirements had to be met with the readout electronics that was characterized in this work.

1.1 Characteristics and Layout of CTA

The general goal of the CTA concept (see Figure 1.1 for a possible realization) is the utilization of the experience of the IACT community to build an array that...

- is more sensitive than the existing IACT generation by roughly an order of magnitude.
- uses new technological advancements to improve operation. One example is the usage of silicon photomultipliers (SIPMs) instead of conventional photomultiplier tubes (PMTs).

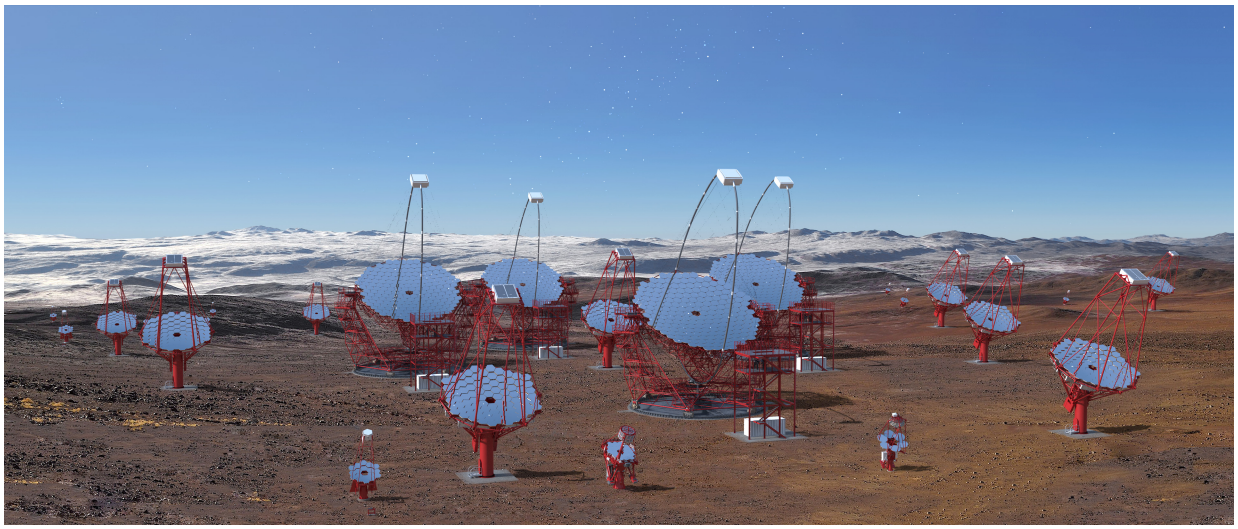

Figure 1.1: Illustration of a possible realization of the southern CTA array. Image credit: Gabriel Perez Diaz.

- extends the accessible particle energy range to both lower and higher energies.
- automates operation as far as possible.

In order to reach the goal of an extended energy range, three telescope types that differ in size were introduced. The telescope sizes were chosen in such way that their energy ranges overlap in order to cross-calibrate them. The telescope types are summarized in the following, the expected performance of the full CTA with respect to the flux sensivity is shown in Figure 1.2.

Large-Sized Telescopes (LSTs)

LSTs (Ambrosi et al. 2013) were designed to cover the energy range between 20-300 GeV. Cherenkov showers that are generated by gamma rays of this energy are very frequent, but show only a small Cherenkov photon intensity. While therefore only few telescopes are needed, the dish size of these telescopes has to be large. The LSTs are designed with a standard parabolic 1-mirror reflector. With a dish size of 23 m diameter and a focal length of 28 m, the LST concept is smaller than the large H.E.S.S. telescope CT5. One of the LST key science goals will be the detection of "Gamma-Ray Bursts", which makes a fast re-positioning necessary. The LST design aims for a re-positioning within 20 s. The LST camera has a 4.5 ° field of view. The 1855 camera pixels consist out of conventional PMTs.

Medium-Sized Telescopes (MSTs)

The MSTs (Pühlhofer 2017) will be the "work horses" for CTA. They will provide the necessary sensitivity in the core energy range of CTA between 100 GeV and 10 TeV. The size and structure of the MSTs are very similar to the existing IACTs of H.E.S.S., VERITAS and MAGIC. The MSTs concept is that of a Davies-Cotton telescope with a dish size of 12 m diameter and a focal length of 16 m. Two different camera concepts, NectarCAM (Glicenstein et al. 2013) and FlashCAM (Pühlhofer et al. 2013), are in development. In the most

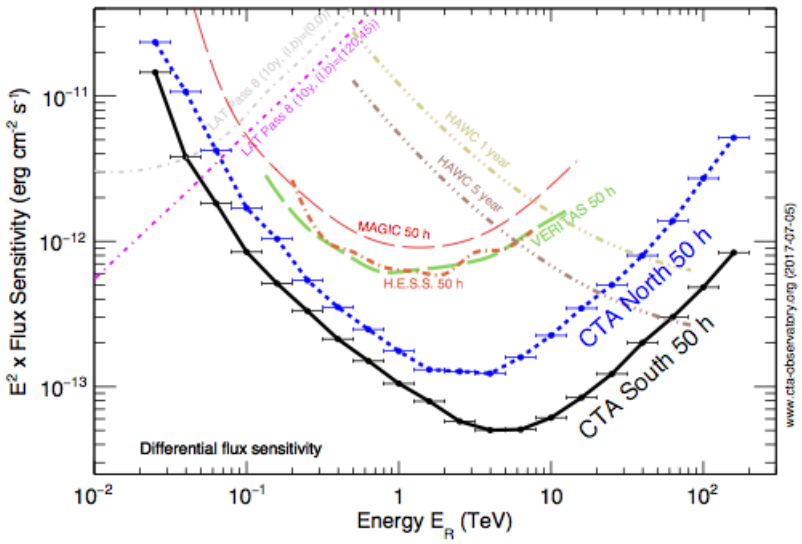

Figure 1.2: Expected flux sensitivity of both CTA arrays. The CTA sensitivity is compared to other instruments. For IACTs, an observation time of 50 h has been assumed. The goal of the CTA design was to outperform the current IACT generation by an order of magnitude (CTA Observatory homepage 2017).

likely scenario both concepts will be used for CTA, but they will be assigned to different hemispheres to ensure minimum calibration effort within one array. Both concepts show a 8 ° field of view, making the MSTs perfectly suited for survey operation. Both NectarCAM and FlashCAM are finely pixelated with ∼ 1800 conventional PMTs.

Small-Sized Telescopes (SSTs)

The highest energies (few TeV to 300 TeV) are the domain of the SSTs. Events in this energy range are very rare due to the steeply falling energy spectra of the anticipated sources. At the same time the photon yield of one of these events is very high. In difference to the LST concept, the SSTs were therefore designed to be numerous, but to have only a small photon collection area. Three different SST implementations are in development, it is not clear at the moment which of these concepts will be used in the final CTA layout. The different concepts are shown in Figure 1.3. Two of the SST concepts, GCT (Tibaldo et al. 2017) and ASTRI (Pareschi et al. 2013), utilize a new dual-mirror design, the SST-1M design (Niemiec et al. 2015) uses a conventional Davies-Cotton design. The dual-mirror designs consist out of a primary mirror with a diameter of ∼ 4 m, a secondary mirror with a size of ∼ 2 m and a focal length of ∼ 2 m. The single mirror for SST-1M has a diameter of 4 m, the focal length is 5.6 m. The camera concepts for the SST telescopes have a field of view of $8 - 9\,^{\circ}$ and the usage of > 1000 SIPM pixels in common. The usage of SIPMs instead of PMTs for Cherenkov cameras has been successfully tested by the First G-APD Cherenkov Telescope (FACT) (Anderhub et al. 2013). SIPMs yield the advantage to be operational under much brighter conditions than PMTs, extending the accessible part of an observation night. The readout electronics characterized in this work is foreseen to be used as part of one of the SST camera concepts, the Compact High Energy Camera (CHEC) (Daniel et al. 2013) for the GCT and ASTRI telescope structures.

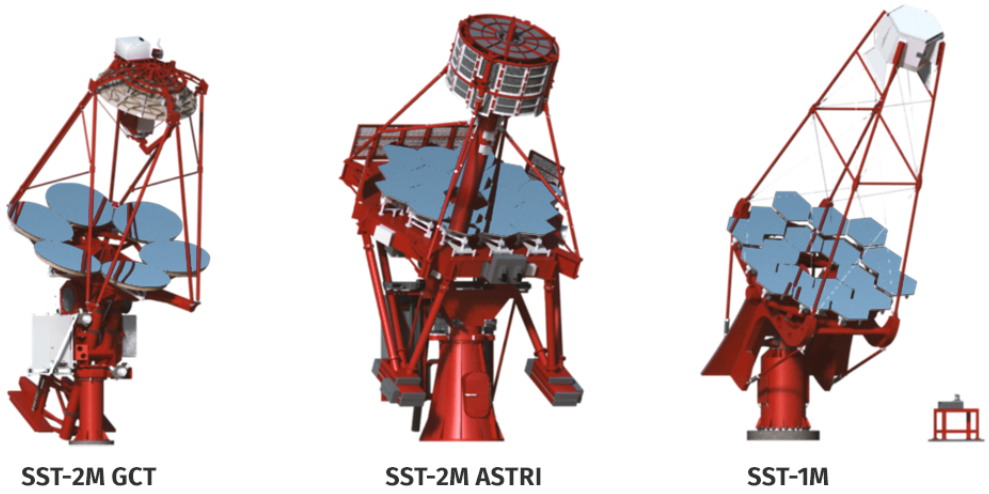

Figure 1.3: Illustration of the different SST implementations. Both the GCT and ASTRI telescopes use a dual-mirror design, the SST-1M uses the conventional Davies-Cotton design. In contrast to both LSTs and MSTs, all SST implementations use SIPMs in their Cherenkov cameras. (CTA Observatory homepage 2017).

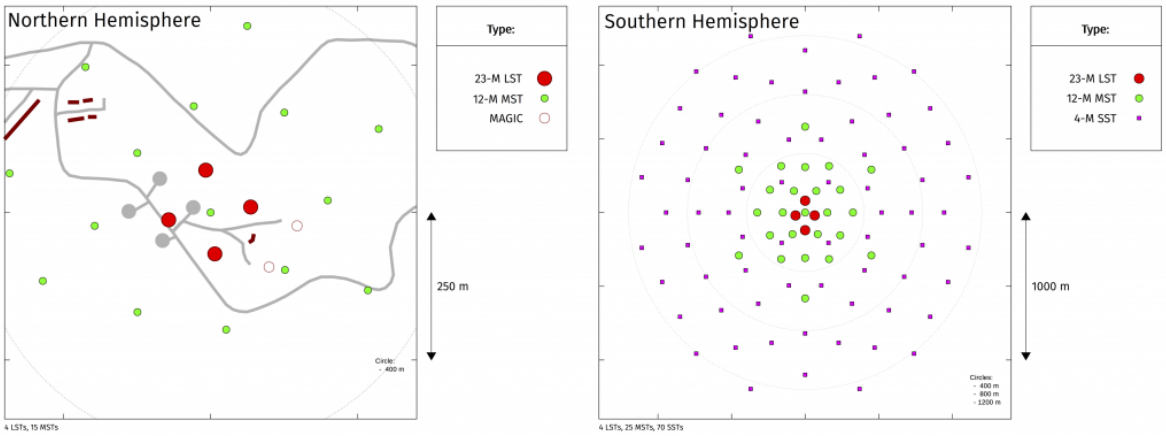

Figure 1.4: Illustration of possible layouts for both the southern and northern CTA array. The northern array is dimensioned much smaller with respect to the southern one, SSTs are completely missing. (CTA Observatory homepage 2017).

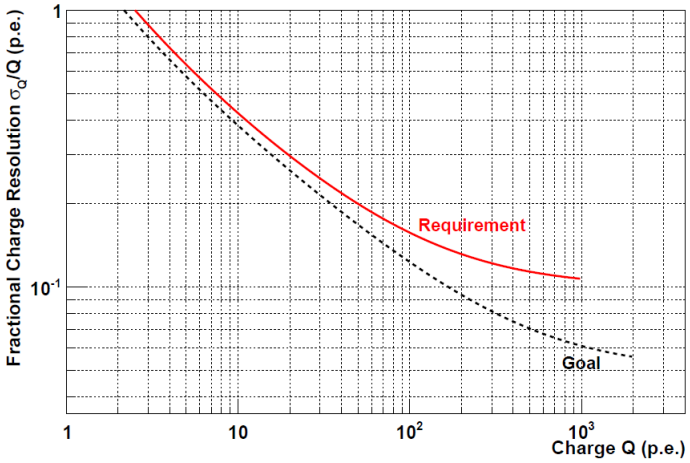

Figure 1.5: CTA requirement for the fractional charge resolution of a SST cherenkov camera in red. In addition a charge resolution goal is shown in black (Hinton 2013).

The exact layout of CTA has not been defined yet, one possible realization is shown in Figure 1.4. The array in the northern hemisphere is dimensioned smaller with respect to the number of MSTs. SSTs are completely missing on the northern hemisphere, they are only part of the southern array. With $\sim$ 70 planned telescopes, SSTs are the most numerous telescope type in the southern array. The reason for the different dimensioning of both arrays is given by the different science goals of the arrays. The southern array will see the central part of the galaxy in a very similar way as H.E.S.S. nowadays. One of the key science goals of CTA South is to search for PeV energy accelerators in the galactic plane. SSTs are mandatory for this task, since they provide the necessary sensitivity at highest energies. The northern array will be limited mostly to extragalactic sources. SSTs are not necessary for this task due to the gamma-ray absorption on the extragalactic background light.

1.2 Requirements for the SST Camera Readout Electronics

The Cherenkov cameras for the SST telescopes, like all other technical components, will be given as in-kind contributions from the consortium to the observatory. The task of the observatory is therefore to define performance requirements for the cameras. These requirements are formulated in such way, that the science goals of CTA can be achieved. Besides the definition of a cost range, the general requirements for the camera regard the operation within a window of predefined limits on observational conditions like temperature, humidity and background light. Most important for this work are the camera requirements that boil down to requirements for the readout electronics. The requirements that are discussed in the following were defined by Hinton (2013). The requirements for the camera readout electronics can be separated and assigned to two different parts of the electronics:

- Requirements for the trigger generating system of the readout electronics. A successful trigger in this regard is the activation of the trigger receiving system for a Cherenkov event which intensity exceeds a predefined trigger threshold. Requirements are given for the minimum intensity of a shower event that the readout has to be able to trigger on. The trigger system of the readout electronics characterized in this work will not be

analyzed, since a rework of this system is ongoing.

- Requirements for the trigger receiving system of the readout electronics. A successful received trigger inherits the sampling, digitization and charge calibration of a triggered Cherenkov event. The most important performance indicator for this part of the readout electronics is the **charge resolution**. The charge resolution quantifies the charge reconstruction performance of a readout system and shall be analyzed for the readout electronics discussed in this work.

The CTA requirement for the fractional charge resolution of a SST Cherenkov camera is shown in Figure 1.5. It is defined as σ_Q/Q with Q being the true pixel charge in photoelectrons (p.e.) and σ_Q the rms-spread of the charge distribution in one pixel. A SST readout system has to be able to reconstruct charges up to 1000 p.e.. The contributions to this charge resolution requirement will be discussed in detail in later chapters.

CHAPTER 2

The TARGET 7 Readout Electronics

The TeV Array Readout Electronics with GSa/s sampling and Event Trigger (TARGET) is based on the TARGET Application Specific Circuit (ASIC) (Tibaldo et al. 2015; Funk et al. 2016). It was designed as a readout electronics for the general use in IACT cameras, but specifically for the GCT cameras of CTA. It is not the main goal of the TARGET concept to achieve the best performance possible, but to fulfil the CTA requirements with an as-low-as-possible budget. Camera concepts for the SSTs have to feature low cost per SIPM channel due to the large number of SSTs in the southern array.

The TARGET readout system characterized in this work is based on the TARGET 7 ASIC, which will be introduced in Section 2.1. TARGET is not limited to the readout of SIPMs, but to any kind of photodetector. The TARGET readout system is partitioned into readout modules, each capable of reading out 64 photodetector channels at once. These modules will be introduced in Section 2.2. TARGET 7 will not be the TARGET generation used in the final CHEC implementation since work on a new generation (TARGET C + T5TEA) is already ongoing. The improvements towards this newest TARGET generation and implications for the characterization procedure of TARGET 7 for this work will be discussed in Section 2.3.

2.1 TARGET 7 ASIC

The TARGET 7 ASIC shown in Figure 2.1. has been developed as an affordable processing solution for photodetector signals of IACT cameras. Its functional block diagram is shown in Figure 2.2. The ASIC is separated into the "trigger path"and the "data path". The data path is responsible for the sampling and digitization of the triggered event. The input signal coming from the photodetector is split to both circuits. One ASIC consists out of 16 independent data paths and is therefore able to sample and digitize 16 channels in parallel. Each of the four trigger paths processes the analogue sum of four channels. Operational values are adjustable and stored in 12-bit registers, the register values used in this work are summarized in Appendix A.6. In the following, only the data path will be discussed since

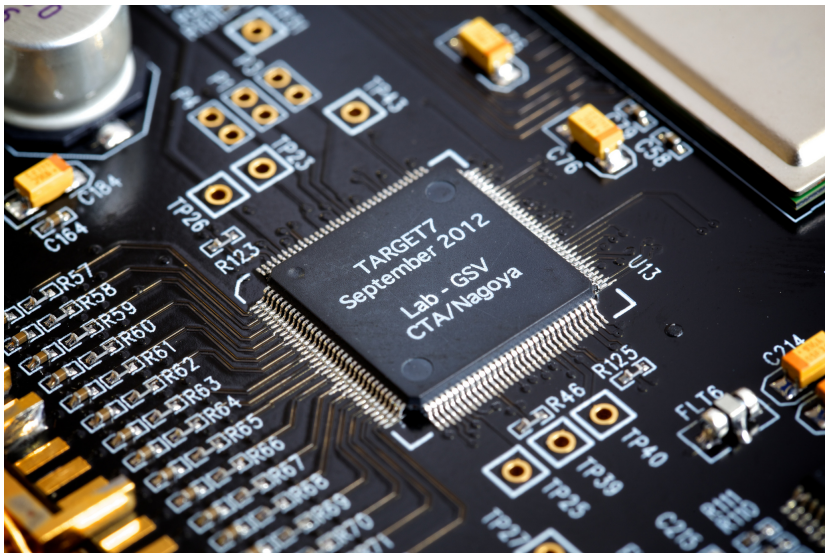

Figure 2.1: TARGET 7 ASIC on board of a TARGET 7 readout module. Credit: Akira Okumura.

this is the part of the readout that was characterized in this work.

The current signal from the photodetector is converted to a voltage signal with the help of a 1 kΩ termination resistor. The voltage signal is capacitively coupled to the input channels. This signal is transferred to a switched-capacitor array consisting out of two blocks of 32 cells, operated in a ping-pong fashion: While one block is sampling the input signal, the other block transfers the sampled voltage signal to a large storage array. This technique ensures a continuous sampling and a dead time free operation. The large storage array is a ring sampler consisting out of 16384 cells partitioned into 512 blocks of 32 cells. The timebase generator defines the hold-time of the capacitors in the sampling array which is usually chosen to be 1 ns for a sampling rate of 1 GSa/s. In this configuration the total buffer time per channel is $\sim 16\,\mu$s.

The samples buffered in the storage array can be randomly accessed in blocks of 32. The full 16 μs history of each channel can be selected. The number of blocks to be read out can be arbitrarily chosen between one and 14 (32 to 448 ns readout window). In the case of a readout signal from the trigger path or an external trigger source the chosen blocks are digitized by a Wilkinson analog-to-digital converter (ADC). An adjustable voltage ramp is generated and a 12-bit counter is started. The digitized signal (the ADC values) corresponds to the number of time steps that were needed by the ramp signal to exceed the analogue voltage stored in the buffer cell. The response characteristic of a specific cell to an applied voltage signal will be unique to this cell and has to be calibrated with respect to differences between the individual capacitors. One block for all 16 channels can be digitized in parallel. The digitization clock has a speed of 208 MHz, the digitization time of one event depends on the size of the signal and the number of read-out blocks. The achievable maximum trigger acceptance rate of the digitization block will be analysed in Section 3.4.

The strength of the TARGET ASIC and the difference to conventional peak-detector circuits is the capability to record the full waveform of a PMT/SIPM event. The TARGET concept furthermore features a dead time free operation and a very large storage array. The large storage array offers the possibility of a slow digitization block, which is usually the most

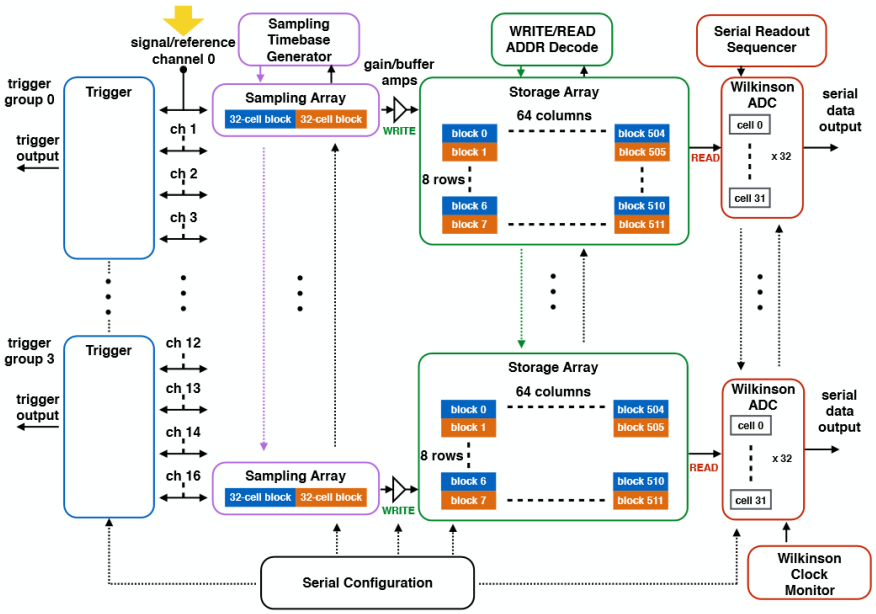

Figure 2.2: Functional block diagram of a TARGET ASIC. The ASIC is separated into a trigger path (blue), the sampling array (purple), the large storage array (green) and the digitization block (red). Samples stored in the buffer can be randomly accessed and digitized in blocks of 32. Image taken from Tibaldo et al. (2015).

cost intensive part of a readout system.

2.2 TARGET 7 Module

A TARGET 7 readout module (e.g. shown in Figure 2.3) is split into two printed-circuit boards. The top board hosts the signal amplifiers and the shaping circuits for each of the 64 input channels. The signal amplification happens in two stages, the total amplification factor is ~ 28. The shaping circuit has been optimized for SIPM signals which usually exhibit a fast rising edge of a few ns and a slow trailing edge of 100 ns to 1 μs. These long signals are shaped to Gaussian-like signals with a FWHM of ~ 15 ns. The shaped and amplified signals are routed to the bottom board which hosts four TARGET 7 ASICS. The TARGET ASICs are controlled by a single Field Programmable Gate Array (FPGA), all operational values for the TARGET ASICs and the slow signal components are settable by this interface via digital-to-analogue converters (DAC). A voltage offset (called Vped) common to all inputs can be applied to the input signals in order to shift the signals to an appropriate working point. In the standalone operation of one single module the trigger signals from the trigger path are routed to the FPGA. The FPGA then triggers the digitization and readout of the specified blocks. Additionally to this trigger mode the FPGA is capable of generating trigger signals by itself. These signals can be chosen to be synchronous to the timebase generator to access a specific storage array block for calibration or testing purposes. This trigger mode is however not resembling the normal operation mode since real trigger signals from the trigger path will be asynchronous. For the charge resolution performance tests in this work, an asynchronous operation mode was therefore chosen.

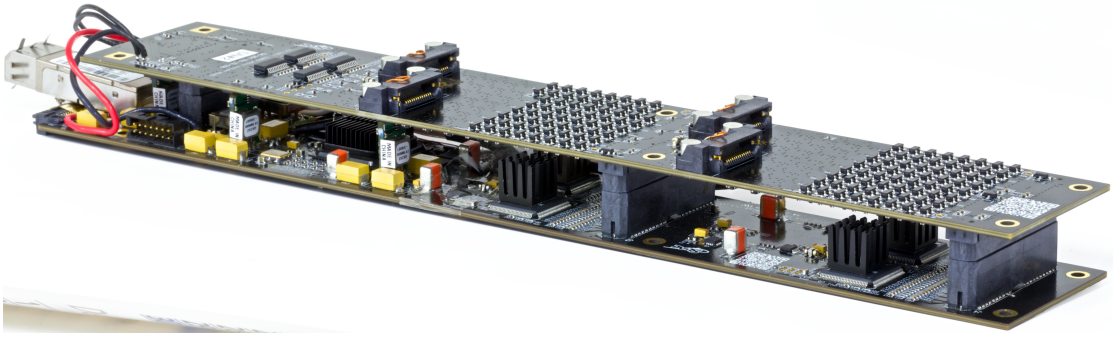

Figure 2.3: Picture of a TARGET 7 readout module. The top board hosts the amplification and shaping circuits, the bottom board the four TARGET ASICs and the FPGA. Credit: Akira Okumura.

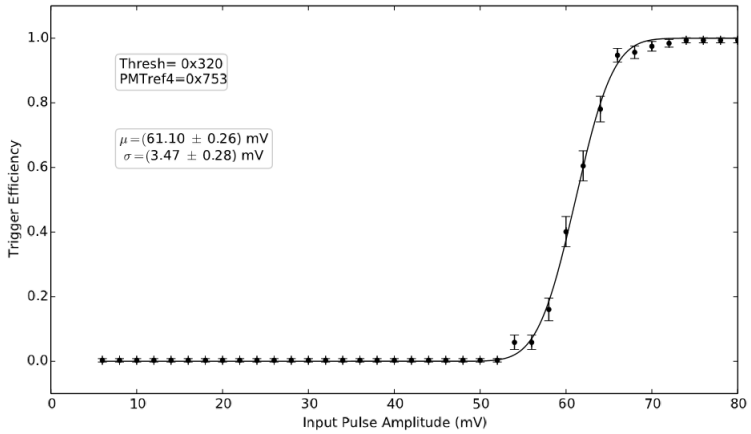

Figure 2.4: Trigger performance of the TARGET 7 trigger path measured by Stahl (2014). The achievable trigger threshold of $\sim 60\,\mathrm{mV}$ is too high to fulfill the CTA requirements. This has been addressed in the latest TARGET generation.

2.3 TARGET C + T5TEA

In the latest generation of TARGET, the data and trigger path have been split to dedicated ASICS, TARGET C and T5TEA. The reason for this redesign is the fact that the trigger path of TARGET 7 did not meet the trigger performance requirements of the CTA observatory. In an internal study by Stahl (2014) it was shown that the trigger threshold for a single channel is $\sim 60\,\mathrm{mV}$ (see Figure 2.4). Depending on the chosen SIPM gain this would correspond to a trigger threshold of more than 10 photoelectrons (p.e.). By splitting the sampling and trigger circuit to two dedicated ASICs the trigger threshold could be reduced to $\sim 3 - 5\,\mathrm{mV}$ (Funk et al. 2016).

The TARGET C ASIC is, for the most part, identical to the data path of TARGET 7. ASIC characteristics analyzed in this work will therefore very likely transfer to TARGET C. The module layout will however change from TARGET 7 to TARGET C, since shortcomings of the TARGET 7 modules identified in this work were eliminated. All identified issues of the TARGET 7 modules and the associated fixes for the TARGET C modules will be discussed in the corresponding chapters in the following.

CHAPTER 3

Electrical Performance of the TARGET 7 Module

In this chapter, the foundation for the charge resolution characterization of the TARGET 7 modules shall be laid by analyzing the electrical performance of the modules. The uncalibrated ADC noise will be analyzed in Section 3.1. Calibration is in the following defined as the step from digitizer ADC to a voltage value. The ADC value will differ from capacitor to capacitor due to fabrication tolerances. In contrast to this, the calibrated voltage is defined to be constant for different storage capacitors. Two calibration techniques are introduced in Section 3.2 and their performance is evaluated. The crosstalk between channels of the same ASIC is analyzed in Section 3.3, the trigger performance is characterized in Section 3.4. Trigger in this case means the successful readout of the specified storage blocks. The trigger signal does not come from the trigger path of the ASIC, but is generated by the FPGA. The full electrical characterization was performed for all four ASICs of one module, it was checked that other modules showed similar behaviors. The ASICs of one module have the identifiers 0-3, the channels within one ASICs are numbered 0-15.

3.1 Uncalibrated ADC Noise

The ADC noise characterization was performed without an external signal source, only direct current (DC) offsets were applied by changing the value of Vped. By using the synchronous trigger that is provided by the FPGA, specific blocks of the storage array could be addressed and read out. In Figure 3.1. an example baseline for three channels for an applied Vped value of 2500 is shown. The maximum number of 14 blocks was read out. This measurement was carried out 10000 times, the resulting ADC value distributions for single cells are shown in Figure 3.1. In this measurement, two characteristics of the TARGET 7 ASICs are imminent. The first block shows systematically higher ADC values than the rest of the storage array. Furthermore, the edge cells of each block (the 32nd cells) show a huge drop in ADC value. After the calibration process these effects vanish. The ADC value distributions for single cells are very narrow with rms-values of ~ 3 ADC values. This rms-value was defined as the single cell ADC noise.

One of the most important performance tests was the ADC noise homogeneity analysis across

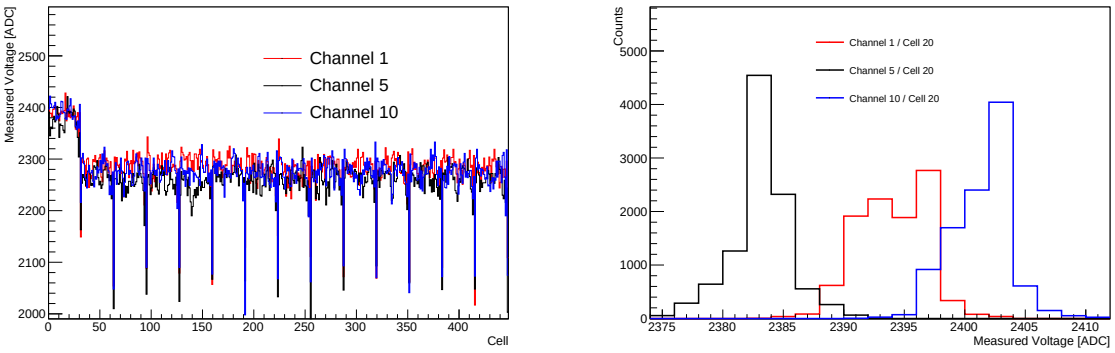

Figure 3.1: *Left* : Uncalibrated baseline for an applied DC offset of Vped=2500 for three channels and the first 14 blocks of the storage array. *Right* : ADC value distribution for single cells and 10000 measurement repetitions.

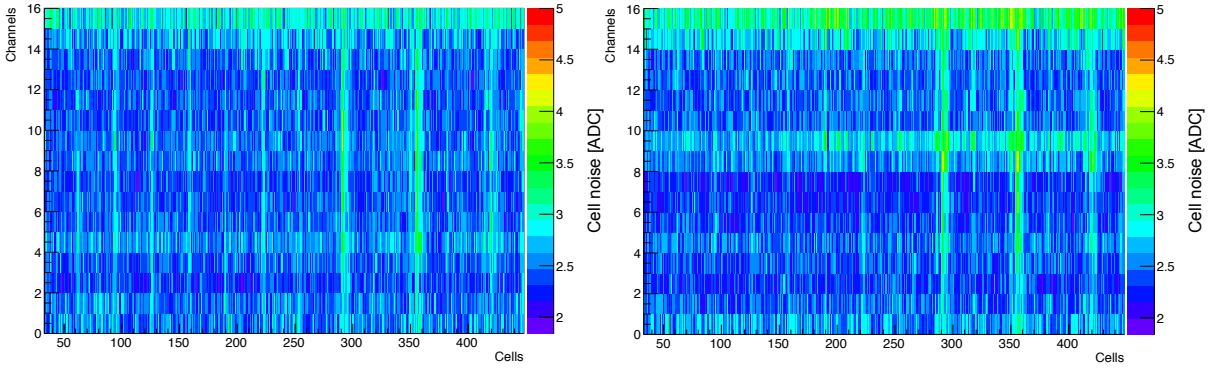

Figure 3.2: ADC noise distribution for ASIC 0 (*left*) and ASIC 1 (*right*) for all channels and the first 14 blocks of the storage array. After the removal of the peltier-element circuit the ADC noise is stable with respect to channel-to-channel variations.

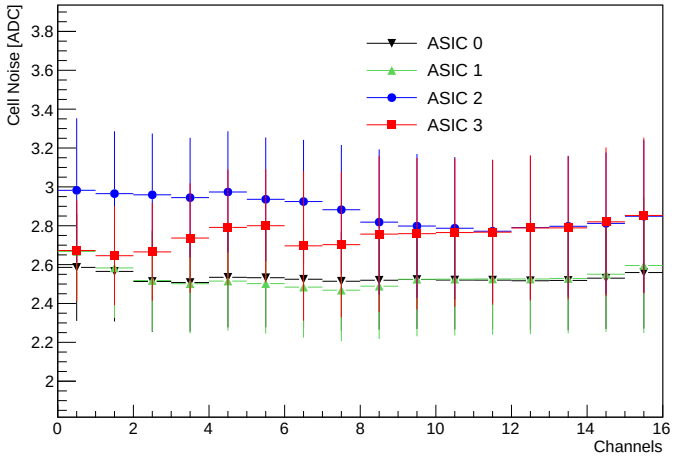

Figure 3.3: ADC noise for all channels and ASICs averaged over the first 14 blocks of the storage array. The error bars are given by the rms-value of the cell ADC noise distribution within one channel.

the cells and channels of a single ASIC. The ADC value of a fixed Vped value of 2500 was recorded 10000-times for all channels and the first 14 storage array blocks. The unmodified TARGET 7 modules showed a very high common noise level of $\sim 4-6$ ADC counts and a systematically increased noise for the channels 10-12. This was traced down to the peltier-element controller that is part of the SIPM cooling circuit. In the final CHEC design, the SIPMs will only be passively cooled, therefore no peltier element is needed. After the removal of this component the ADC noise of the tested storage array blocks showed a very homogeneous distribution between 2 and 3.5 ADC values for all ASICs and channels. The ADC noise for the ASICs 0 and 1 for the first 14 blocks is shown in Figure 3.2. The remaining 498 blocks of each channel showed no systematic deviation from the behavior of the first 14 blocks. In Figure 3.3. the ADC noise is averaged over the first 14 blocks of each channel and depicted for all channels and ASICs. The error bars are given by the rms-value of the cell ADC noise distribution within one channel. The common noise level is in the range of 2.5-3 ADC counts. The channel-to-channel differences are most likely due to variations in the production process. The ADC noise does depend only weakly on the chosen Vped value, a more detailed investigation will happen in Section 3.2.

Cherenkov cameras for CTA are required to be operational in the ambient temperature range of $-15\,^\circ$ to $25\,^\circ$ with an air temperature gradient of $< 7.5\,^\circ$/h (Hinton 2013). The temperature inside the camera is expected to be rather stable within a few degrees, but performance changes due to temperature variation might nevertheless occur. In order to quantify the impact of temperature variations on the ADC noise level, the measurement shown in Figure 3.3 was performed for different temperatures in the range of $2.5-40\,^\circ$. The FPGA on the module was only specified down to $0\,^\circ$, therefore no measurement below $0\,^\circ$ has been performed. The measurements were performed in a temperature chamber, the temperature was increased in steps of $2.5\,^\circ$. Between each temperature step the measurement was paused until the on-board temperature sensors showed a stable read-back. The temperature dependence of the ADC noise is exemplary shown for three channels in Figure 3.4. The ADC noise has been averaged over the first 14 blocks, the error bars are given by the rms-value of the cell noise distribution within one channel. No significant trend is observable, the noise seems to be constant with respect to temperature variations.

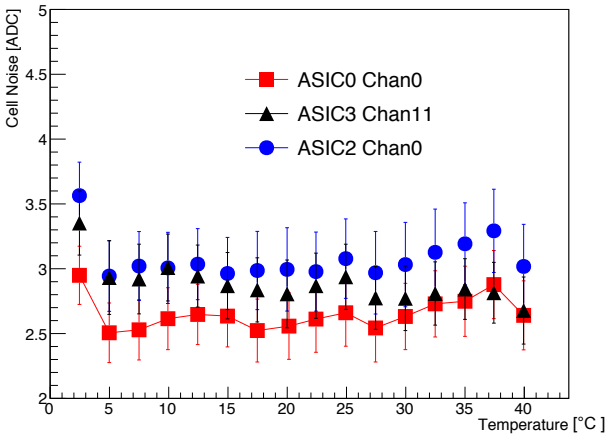

Figure 3.4: ADC noise for three channels and ambient temperatures $2.5 - 40\,°\mathrm{C}$ averaged over the first 14 blocks of the storage array. The error bars are given by the rms-value of the cell ADC noise distribution within one channel.

In summary, the ADC noise of single cells has shown to be very stable with respect to channel-to-channel variations and for different ASICs. The modifications necessary to achieve this high homogeneity were adopted for the whole TARGET 7 module generation.

3.2 Calibration Techniques and their Performance

In order to perform the calibration from ADC value to a voltage value in mV, the s.c. "transfer function" of all capacitors in the storage array has to be known. The transfer function differs from cell to cell and also depends on the cell position in the readout window. The transfer functions will furthermore be influenced by the ambient temperature. The transfer function of every cell can be recorded by sweeping through all possible Vped values (12-bit = 4096 DC offsets) and recording the cell response, the maximum value of Vped is given by $4095 = 2.5\,\mathrm{V}$. Example transfer functions for a single cell recorded at different temperatures are shown in Figure 3.5 together with their relative deviation for different temperatures. The x-axis values are given by the set Vped values, the y-axis is given by the measured ADC response. Only small deviations of $\leq 1\,\%$ are observable for the large temperature range of $5 - 30\,°\mathrm{C}$. The Vped values can be translated to mV:

$$\mathrm{Vped}_{mV} = \mathrm{Vped}_{DAC} \cdot \frac{2500\,\mathrm{mV}}{4096\,\mathrm{DAC}} \tag{3.1}$$

The dynamic range of a channel is given by the interval of ADC values where the transfer function shows a quasi-linear slope. For TARGET 7 this is evaluated to be $\sim 1.9\,\mathrm{V}$ when choosing a DC offset of Vped $= 700\,\mathrm{DAC}$. For the Vped $= 1144\,\mathrm{DAC}$ value used in this work, the dynamic range is $\sim 1.5\,\mathrm{V}$. Signal amplitudes above this dynamic range will show saturation effects. A big part of the charge extraction technique discussed in this work will deal with the charge estimation of large, saturated pulses.

Two different calibration schemes were evaluated in this work:

- **Full calibration method:** The simplest calibration method uses individual transfer

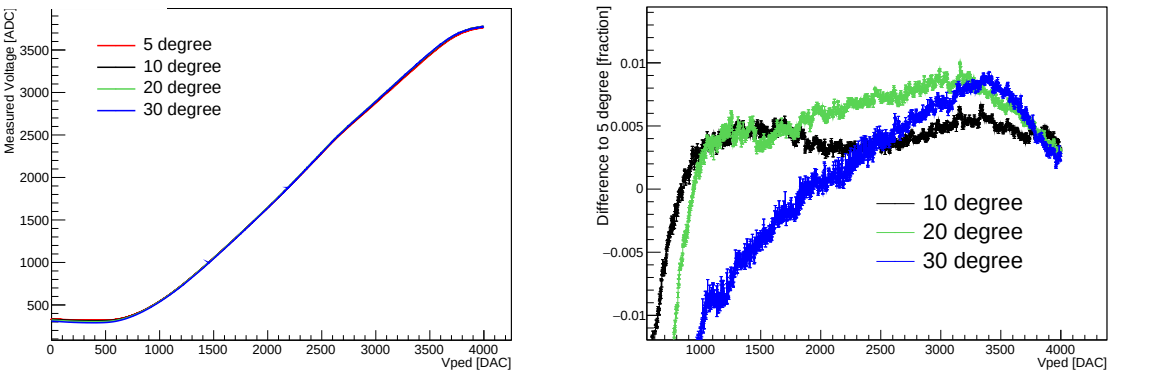

Figure 3.5: *Left* : Storage array transfer functions for one cell and different ambient temperatures. *Right* : Fractional deviation of the transfer function taken at $10 - 30\,^{\circ}\mathrm{C}$ compared to $5\,^{\circ}\mathrm{C}$.

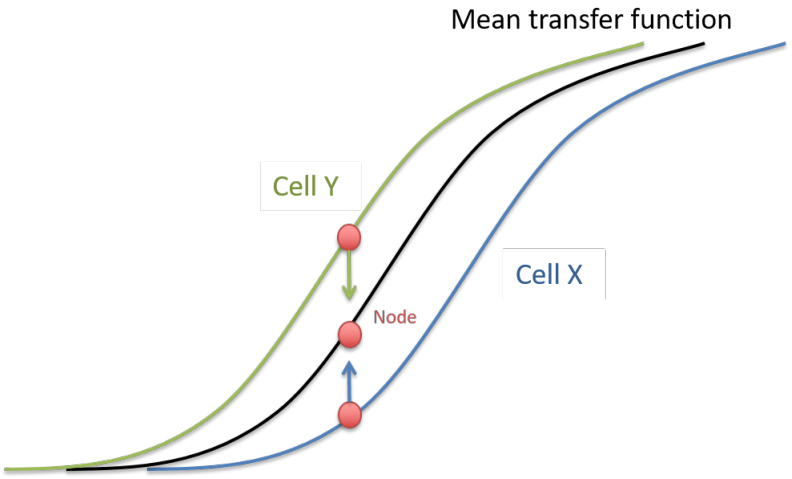

Figure 3.6: Illustration of the pedestal calibration method. For every cell in the storage array an average transfer function is applied according to its position in the readout window. In order to account for cell-to-cell variations, the transfer function is shifted by a constant offset based on the measured deviation at one node.

Vendor	Keysight
Model name	33611A
Signal shape	Triangular
Rise time	1.9 ns
Fall time	1 μs

Table 3.1: Frequency generator model and standard input values for the injected SIPM-like signals used in this work.

functions for every cell and all readout starting positions. The starting position is defined as the first cell of the readout window. The SST camera requirements suggest a likely readout window of 80 ns (Hinton 2013), therefore three blocks were read out and three readout starting positions had to be recorded for each cell. This method is the best calibration method with respect to minimized calibration uncertainties. The biggest downside is that for each single module 1-6 GB of transfer function data has to be stored depending on how fine the Vped sampling is chosen.

- **Pedestal method:** This method assumes that in first order only the cells of the sampling array are important for the shape of the transfer function. Therefore a mean transfer function for every sampling cell is determined. The sampling cells can then be mapped to the storage cells in the readout window. The cell-to-cell difference in the storage array is supposed to only show itself as a constant shift in DAC values of the transfer function. This shift is measured by recording the ADC value of a fixed Vped value and shifting the mean transfer function by the difference of the mean to the cell ADC value. The node for the transfer function shift was chosen to be the baseline value used for the charge resolution measurement (Vped = 1144). This leads to a size of the calibration data for one module of a few MB. The method scheme is illustrated in Figure 3.6.

In Figure 3.7. the comparison of an uncalibrated to a calibrated baseline and a calibrated sinusoidal input signal is shown for the full calibration method. The voltage drops in the 32nd cells are successfully corrected by the calibration method. In Figure 3.8 the DC noise of a single calibrated cell and for one channel averaged over two blocks is shown for a sweep through the whole quasi-linear Vped range. The single cell shows very low noise, since no cell-to-cell calibration uncertainties are included. The noise level averaged over two blocks depends on the chosen calibration method. The full calibration method shows a quasi-constant calibration uncertainty for the whole Vped range and a resulting DC noise of 2-3 mV. The pedestal method shows an increased calibration contribution to the DC noise. The lowest noise is achieved where the Vped node is located and a rise in noise is observed for higher Vped values. For the whole following work the full calibration method has been used since this method performs much better than the pedestal method. Since the transfer functions only show a negligible temperature trend of $\leq 1\,\%$ (see Figure 3.5) the transfer functions were recorded for only one temperature of 20 °C.

In Figure 3.9 calibrated signal pulses from a frequency generator are shown for three different input amplitudes, the highest amplitude is chosen to be in the saturated range. As expected, the saturated input pulse shows a plateau-like shape. The standard input values for the

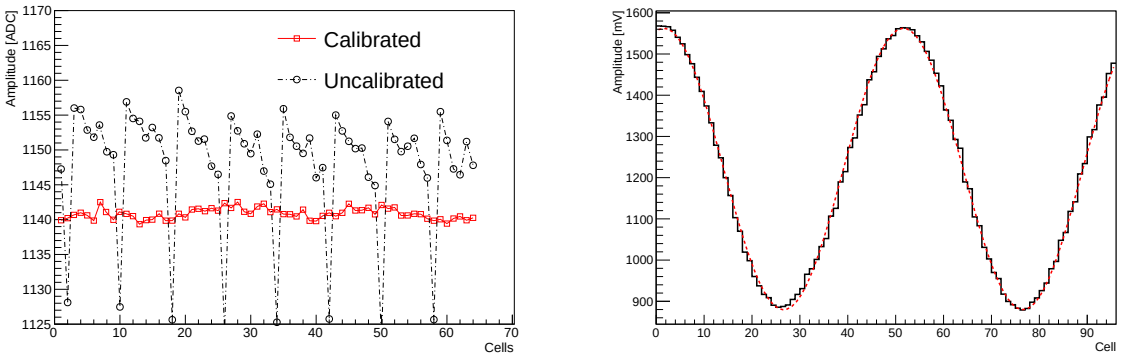

Figure 3.7: *Left* : Baseline before (black) and after (red) applying the full calibration algorithm. The voltage drops in the 32nd cells are calibrated out. *Right* : Calibrated sinusoidal waveform in black and best-fit model in red for the full calibration technique.

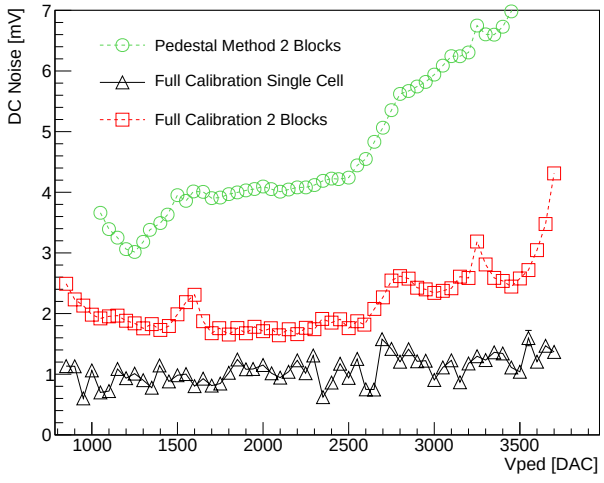

Figure 3.8: Comparison of the achieved DC noise after applying the calibration routines averaged over two blocks (green/red) and for a single cell in black. The pedestal method shows a much higher noise compared to the full calibration method and was therefore not used in this work.

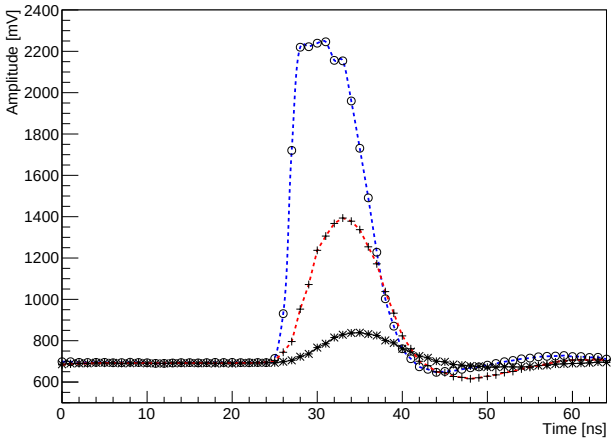

Figure 3.9: Calibrated SIPM-like input signals for three different amplitudes. The highest amplitude in blue shows saturation effects. The shaping circuit on the module induces an undershoot after the signal waveform.

SIPM-like input pulses are summarized in Table 3.1. These values stayed the same for all measurements shown in this work. It has to be noted that the fall time for the input signal is exaggerated, expected signals from a SIPM have fall times of $\sim 100\,\text{ns}$. It is observable that the shaping circuit nicely converts the very long input signals to gaussian-like pulses with a FWHM width of $\sim 12 - 15\,\text{ns}$. After the signal peak, an undershoot of $\sim 20 - 30\,\text{ns}$ is observable that changes its shape with increasing signal amplitude, but stays the same for a fixed amplitude. Therefore the presence of the undershoot has no impact on the charge resolution characterization.

3.3 Crosstalk between Channels

One of the most dangerous effects than can influence the charge resolution performance is a potential crosstalk between channels. Two different sources of crosstalk have to be distinguished. Crosstalk can take place inside the ASIC itself and it can be induced by the layout of the module. In order to test for inter-channel crosstalk, pulses of different amplitudes were injected in a single channel and the response of all other channels (the receiving channels) was recorded. This measurement was repeated for each input channel and signal amplitude for 10000 times and the crosstalk $X^i_j(\text{mV})$ from channel i to channel j defined in Equation 3.2. was evaluated. The crosstalk was evaluated comparing the mean highest amplitude in the three block readout window of channel j with and without an injected signal into channel i.

$$X^i_j(\text{mV}) = \frac{\langle Input_j(\text{mV})\rangle - \langle NoInput_j(\text{mV})\rangle}{\langle Input_i(\text{mV})\rangle} \tag{3.2}$$

The fractional crosstalk is exemplary shown for input channel 2 in Figure 3.10. The amplitude on the x-axis is given by the amplitude as set on the frequency generator in mV. The crosstalk is $\leq 1\,\%$ for most receiving channels. This amount of crosstalk is expected within the ASIC itself. The very large crosstalk from channel 2 to channel 0 and partially channel 1 is unexpected. Similar crosstalk patterns arise for other input channels. For one input channel only a few channels are affected by crosstalk. Furthermore the crosstalk keeps rising

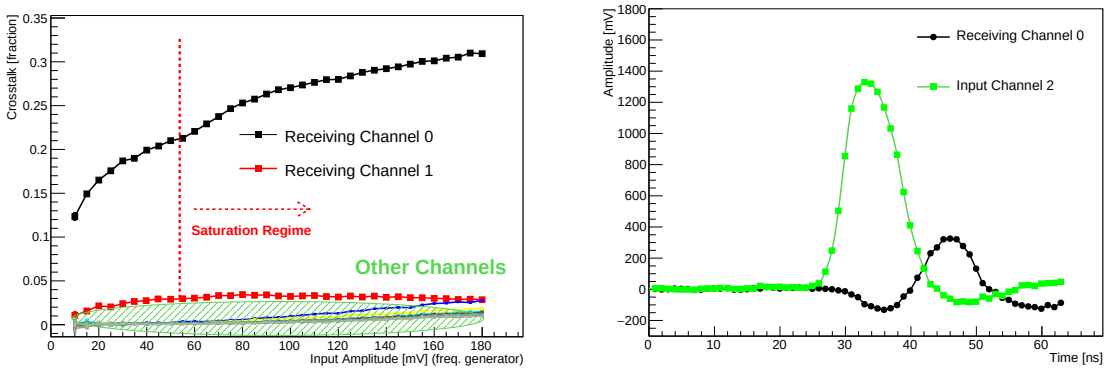

Figure 3.10: *Left* : Measured crosstalk for all receiving channels of one ASIC for input channel 2. *Right* : Injected crosstalk waveform in channel 0 for a signal input in channel 2. The time delay between signal and crosstalk is stable and can be traced down to the amplifying circuit on the module.

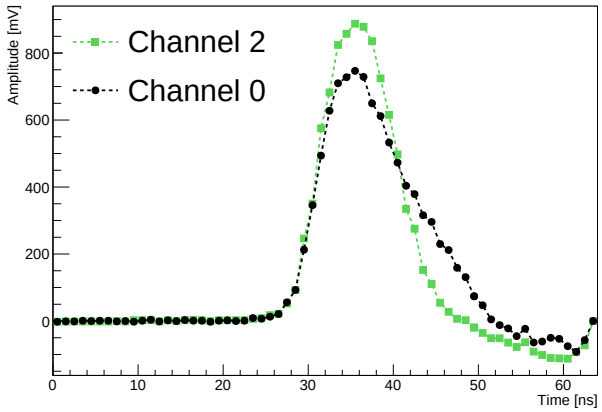

Figure 3.11: Comparison of measured waveforms for signal input in both channel 0 and 2. The crosstalk from channel 2 into channel 0 drastically changes the shape of the waveform in channel 0.

even in the saturated regime of the input channel. This fact and the knowledge of the exact crosstalk pattern helped to trace down this unexpectedly large crosstalk to the amplifying circuit of the module. The amplified signal line of channel 2 is routed parallel to the amplifier input line of channel 0 and 1. Despite being separated by several grounding layers these lines seem to be able to interfere with each other. The injected crosstalk signal shape shown in Figure 3.10 verifies this assumption. The input and crosstalk signals are delayed by several ns. This delay fits to the delay between input and output of the amplifying circuit.

The danger in this large crosstalk amplitude is not only given by a wrong integration value of the signals in the receiving channels but also by the change in the signal shape. The big advantage of TARGET is that the full waveform is read out for every event. Therefore the signal shape can be used to extract the charge in the saturated regime. However in the presence of crosstalk this shape changes with respect to input signals on other channels. In order to visualise this the input signal was injected into both channel 0 and 2 at the same time. The signal shape in channel 0 shown in Figure 3.11 is clearly influenced by the delayed crosstalk signal. A crosstalk of this kind is simply not acceptable for the TARGET readout system. The observation of the level of crosstalk in this work was one of the reasons for the

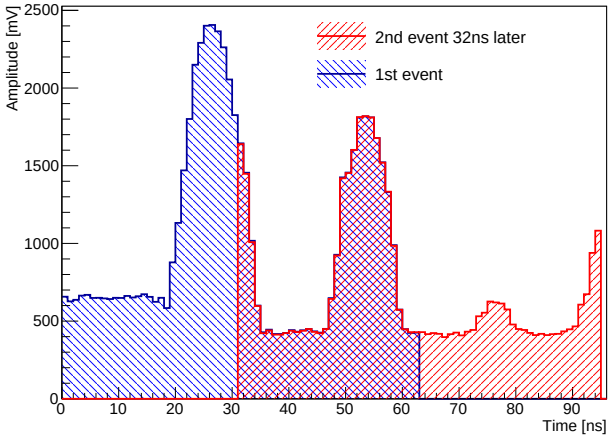

Figure 3.12: Triggered events with a time delay of 32 ns. Both events nicely overlap. The successful readout of these events illustrate the dead time free operation of the TARGET ASIC.

module redesign for TARGET C. In this new module generation the crosstalk issue has been resolved. The charge resolution measurements shown in Chapter 4 were performed for single channels only without the presence of signals in other channels.

3.4 Event Rate Performance of the Sampling Path

In order to correctly characterize the charge resolution, the maximum achievable trigger acceptance rate of the sampling path has to be known since a neglected event would count as a maximal misreconstructed event. The trigger acceptance includes a potential dead time. According to Paz Arribas et al. (2012) the expected SST trigger rate will be $\lambda \sim 600\,\mathrm{Hz}$. The distribution of the time δt between two events is given by an exponential distribution $\propto e^{-\lambda \delta t}$. Events with a small temporal distance will therefore occur much more likely than events with a large one.

In order to test for a potential dead time of the TARGET readout system a conventional PMT was used as both signal and trigger input source. The frequency generator itself was not capable of generating signals with a ns spacing. The PMT output was connected to a signal processing chain consisting out of a discriminator generating NIM pulses and a NIM-TTL converter. The resulting ns-width TTL pulses were used as input and trigger signal for the TARGET module. Figure 3.12 shows the example of two events separated by $\sim 32\,\mathrm{ns}$ that nicely overlap. Unfortunately neither a constant signal amplitude level nor an exponential distribution of δt could be achieved, very likely due to the signal processing. Nevertheless two important conclusions could be drawn out of the recorded signals. The dead time free operation of TARGET ASICs could be confirmed since many successful triggers with a ns spacing could be recorded.

The second conclusion is that blocks that are in the readout process prevent the recording of new events that fall into these blocks. This behavior is visible in Figure 3.13. The distribution of the time between two events shows dips for integer multiple of the storage buffer size ($\sim 16000\,\mathrm{ns}$). Since the affected events are rejected, this leads to a reduced trigger acceptance. A possible solution to this issue would be to simply jump over blocks that are currently in the readout process. Firmware adaptations regarding this issue are currently under development.

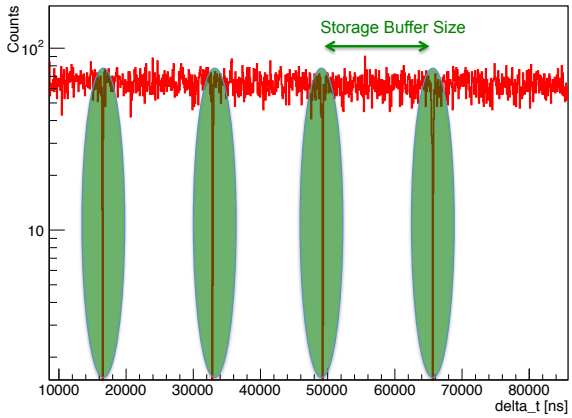

Figure 3.13: Time delay distribution of two successively triggered events for a homogeneous time delay injection. The distribution shows drops at the time delay that fits to integer multiples of the total size of the storage array ($\sim 16\,\mu$s). This behaviour could be fixed very easily by jumping over blocks that are read out at the occurence of the next event.

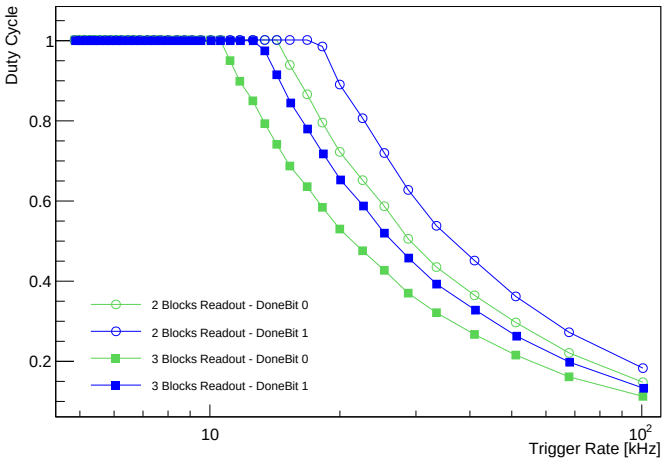

Figure 3.14: Duty cycle of the sampling path for evenly spaced triggers at different rates.

The maximum achievable trigger acceptance rate has been evaluated by injecting signals as specified in Table 3.1 with an after-amplification amplitude of $\sim 500\,\mathrm{mV}$ and a varying frequency using the frequency generator. Figure 3.14 shows the duty cycle, defined as the fraction of triggered input events, for readout windows of two and three blocks, respectively. Additionally the performance of the "Done-Bit" was tested. In normal operation the ramp counter in the digitization block always counts from 0 to 4095 and does not stop when exceeding the cell voltage. By activating the "Done-Bit" the digitized ADC value is transferred as soon as the ramp exceeds the capacitor voltage, which speeds up the digitization process depending on the digitized signal amplitude. For small and mediocre signals this technique shows a large speed gain. The scenario of a constant rate is of course not valid for normal operation since an exponential distribution is expected. Nevertheless given that rates up to $10\,\mathrm{kHz}$ are achievable with a fixed δt and the non-presence of any dead time the conclusion that the TARGET modules fulfil the requirement of a $600\,\mathrm{Hz}$ trigger acceptance rate can be drawn.

CHAPTER 4

Charge Reconstruction and Charge Resolution

The ultimate goal of this work was to develop a stable charge reconstruction method for the TARGET 7 module generation and to draw conclusions for the next TARGET generation from the charge resolution performance. The charge reconstruction method itself will be introduced in Section 4.1. Within this method the normal operation will be distinguished from operation in the saturated amplitude regime. Necessary corrections to the signal observables are introduced in Section 4.2. The performance of the charge reconstruction method with respect to the charge resolution requirements of CTA will be discussed in Section 4.3.

4.1 Development of a stable Charge Reconstruction Method

The task of the charge extraction method implemented for this work was to find an observable of the signal waveform that can be connected to the charge of the event. The charge is given by the number of photoelectrons generated by the photodetector. For this work the charge could be determined by the signal amplitude since the plan for the GCT camera was to tune the photodetector gain to achieve 3-4 mV/p.e. after amplification. Therefore all observables that can be connected to the signal amplitude are of interest for the charge extraction. The requirements for the charge extraction method were the following:

- Three blocks (96 ns readout window) have to be read out.
- Not a single event may be dropped during charge reconstruction.
- The charge resolution requirement for the CTA SST cameras shall be met.

The charge extraction algorithm is summarized in a flow chart in Figure 4.1. The algorithm always starts with a Gaussian fit to the waveform in the readout window. The position of the waveform inside the readout window is a priori known to an extent of ± 8 ns. This knowledge is used as a seed value for the Gaussian fit. The best-fit Gaussian determines the peak position of the waveform. Furthermore, the baseline can be extracted from the Gaussian fit and be subtracted. The waveform is then integrated ± 7 ns around the peak position. Based on

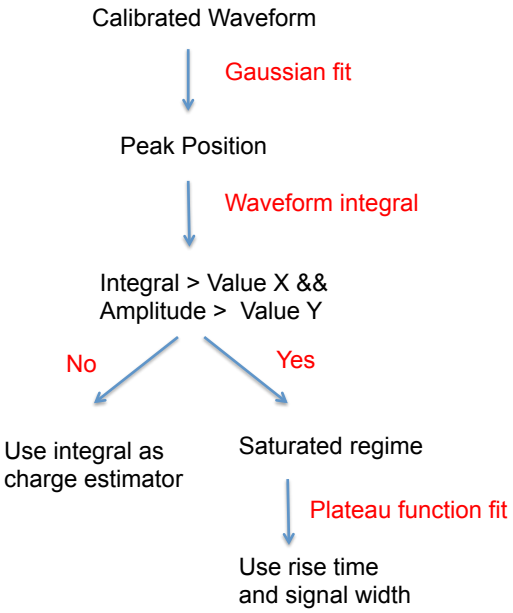

Figure 4.1: Scheme of the charge extraction algorithm that was applied.

the waveform amplitude and the integral value the charge extraction algorithm has to decide whether to use the integral itself as charge estimator or to pick the saturated extraction route. The two extraction routes are briefly discussed in the following.

Non-Saturated Regime

In the non-saturated regime the waveform integral depicted in Figure 4.2 is the best charge estimator. The waveform integral is calibrated prior to the charge resolution measurement using "calibration runs" with the frequency generator. The measured waveform amplitude is converted to a photoelectron equivalent assuming either 3 or 4 mV/p.e. after amplification. Of course the measured amplitude is not the true amplitude but only an estimator, systematic deviations might be present and will be taken care of by introducing an additional systematic

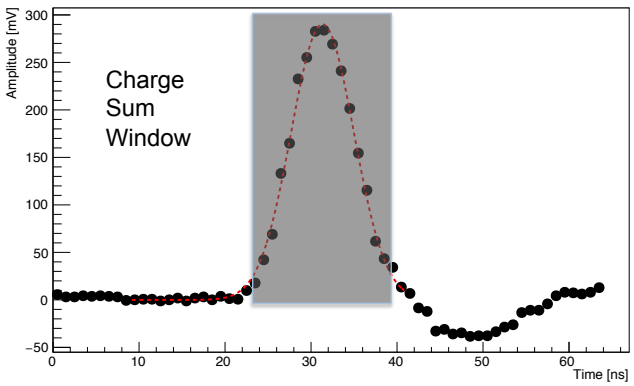

Figure 4.2: Calibrated signal waveform in black and best-fit Gaussian model in red. The integral window is depicted by the grey shaded box.

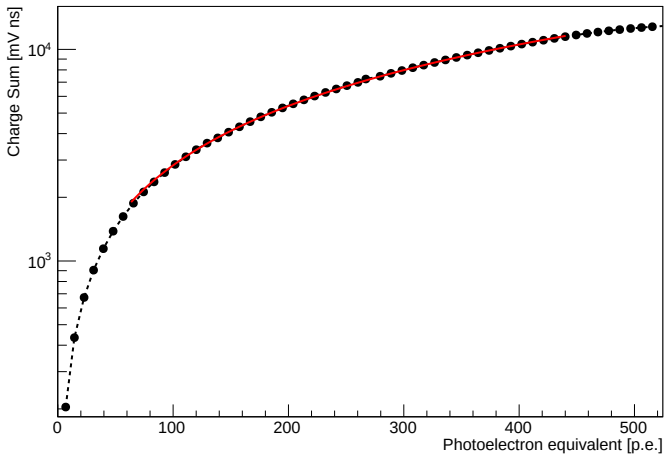

Figure 4.3: Dependence of the charge integral onto the injected signal amplitude in the dynamic regime. The amplitude is converted to a photoelectron equivalent by assuming 3 mV/p.e. Additionally the best-fit linear model is shown in red.

uncertainty in the charge resolution determination. An example of an integral calibration measurement is shown in Figure 4.3. The charge integral shows a linear dependence on the number of photoelectrons for a very large range. Most importantly the calibration curve also shows a very small spread for each injected amplitude.

Saturated Regime

In the saturated regime the waveform integral is not a good charge estimator any more since the integral value only grows slowly. The waveform basically behaves like a growing Gaussian with a chopped-off top. This behavior can be utilized by extracting the rise and fall time and the width of the waveform. After the decision has been made to treat a waveform as a saturated signal, the waveform is fit with a plateau-like function defined in Equation 4.1.

$$V(t) = \frac{A}{\left(e^{r(t-w)}+1\right)\left(e^{f(-t-w)}+1\right)} \tag{4.1}$$

Here A is the amplitude, r the rise time, t the fall time, and $2w$ the width of the signal. A drawback of using this fit function is the need for very strict seed values since the function is very unstable due to the two exponentials in the denominator. An example of a saturated waveform and the best-fit plateau function is shown in Figure 4.4. The waveform observables chosen for the charge extraction algorithm are the rise time and the width of the waveform. Due to the undershoot after the waveform the fall time shows a very large spread and cannot be used. The rise time and width for different signal amplitudes as set on the frequency generator (pre-amplification) are shown in Figure 4.5. The error bars are given by the rms-spread. Especially the rise time shows a stable increase with increasing amplitude. However in contrast to the waveform integral in the non-saturated regime this time only a x^2 dependence can be achieved as indicated by the second-order polynomial fit. This leads to a $\sqrt{x}$-dependence when inverting the function and using it for charge extraction. Another complication is the very large spread for a fixed waveform amplitude which will drastically increase the charge resolution uncertainty. However due to the absence of any other charge estimator the charge

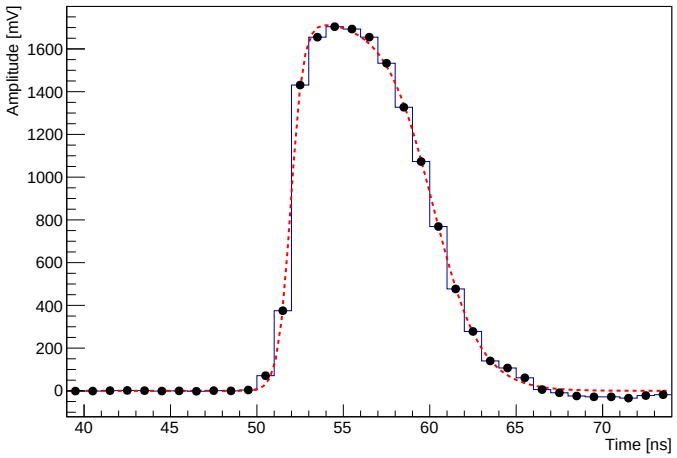

Figure 4.4: Calibrated waveform in the saturated regime in black and best-fit plateau model in red. The width and rise time of the waveform have been used as waveform observables in this regime.

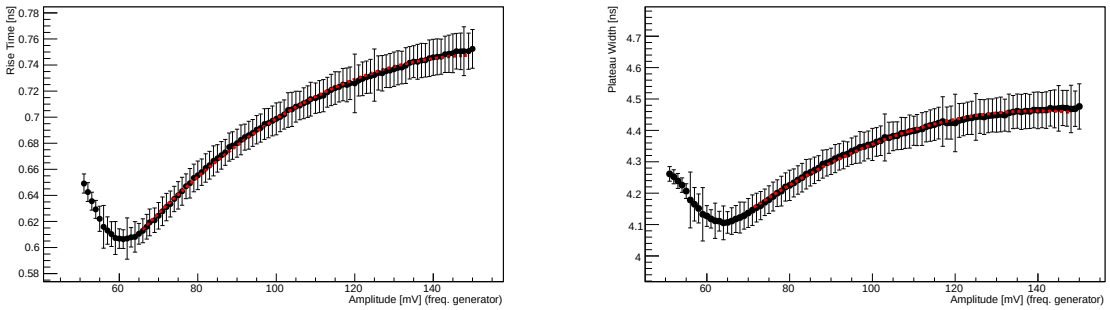

Figure 4.5: Dependence of the rise time and signal width on the injected signal amplitude as set by the frequency generator. Both observables show a very large spread and only a x^2 dependence in difference to the linear dependence of the charge integral in the dynamic regime.

was extracted by averaging over the charge determined with the rise time and the width of the signal. The observables were calibrated to a photoelectron equivalent by linearly extrapolating the pre-amplification/post-amplification dependence of the injected signal amplitude from the non-saturated regime.

4.2 Spatial Dependence of Waveform Observables

During the development phase of the charge extraction algorithm it was observed that all waveform observables (integral, rise time and width) depend on the position of the waveform in the storage array. All observables change in a periodic 64 ns pattern that is stable across the whole storage array. The pattern is furthermore stable for different channels and even modules. An example of this pattern for all used waveform observables and a post-amplification amplitude of 1000 mV is shown in Figure 4.6. The magnitude and shape of this pattern depends heavily on the amplitude of the injected signal. The source of this effect is very likely to be found in the calibration method introduced in Section 3.2. Alternating current (AC) effects are simply neglected by this calibration method which uses a simple voltage offset

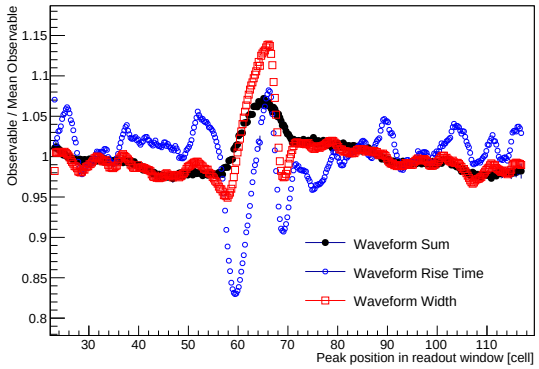

Figure 4.6: Spatial dependence of all three waveform observables. This measurement has been used to calibrate the observed variation.

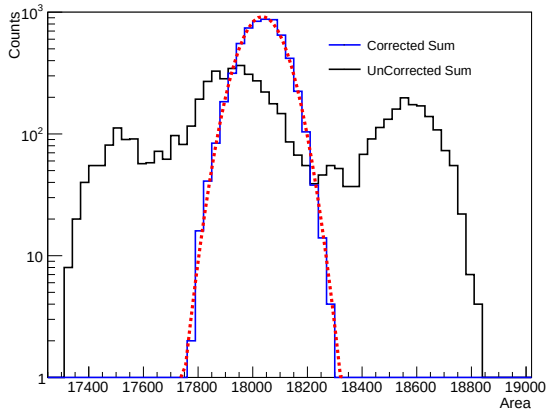

Figure 4.7: Charge integral distribution for signals injected at several storage array positions before (black) and after (blue) applying the spatial correction shown in Figure 4.6. Additionally the best-fit Gaussian model is shown.

(Vped) for calibration. The fact that these patterns show a 64 ns periodicity points towards the sampling array being the origin of this AC effect. This effect could be circumvented in principle by directly calibrating with signal pulses. Tests of this calibration method for the TARGET C generation are currently ongoing and hence can not be disussed here.

The presence of such an effect would of course influence the performance of the charge extraction method. However since the observable patterns are very stable across the whole storage array and also all tested channels, this effect can be corrected very easily by using a simple 64 ns lookup for every observable. In order to test the observable correction method, pulses were injected into one channel at different storage array positions. In Figure 4.7, the waveform integral is shown for one amplitude before and after the correction. Before the correction, a very large distribution can be observed. After the correction, the distribution can be very well described by a Gaussian model, indicating that no systematic integral dependence is left.

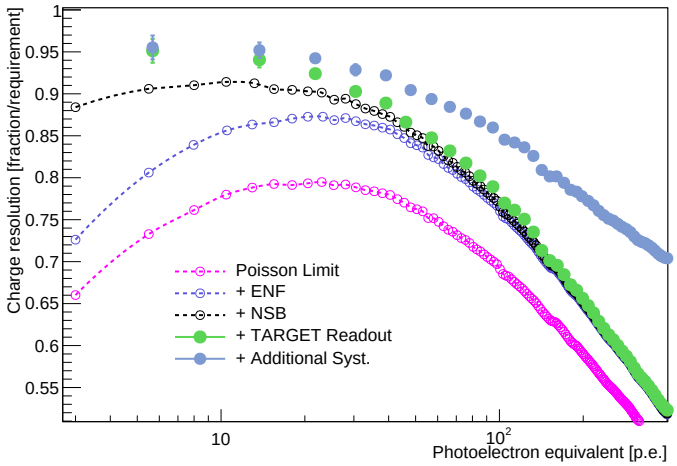

Figure 4.8: Charge resolution in the dynamic regime divided by the CTA SST camera requirement as measured in this work for a gain of 3 mV/p.e. Additionally the total resolution has been split into the Poisson limit, contributions from the photodetector (ENF), contributions from a night-sky background (NSB) with a rate of 125 MHz and the impact of additional systematic uncertainties approximated to be 5 %.

4.3 Performance of the Charge Reconstruction Method

The charge resolution requirement given by CTA is defined for a full camera system including photodetector and for a specific night-sky background (NSB) rate. Since neither the impact of the photodetector nor the NSB has been measured in this work the contributions to the charge resolution have to be approximated. The definition of the charge resolution $\frac{\Delta Q}{Q}$ used in this work is shown in Equation 4.2.

$$\frac{\Delta Q}{Q} = \sqrt{\sigma^2_{TARGET} + \frac{(1+ENF)^2}{Q} + T_{Int} \cdot NSB_{Rate} \frac{1}{Q^2} + \sigma^2_{sys}} \tag{4.2}$$

Here σ^2_{TARGET} is the fractional charge resolution of the TARGET readout system alone (amplifying circuit + module noise + TARGET ASIC contribution). The second term describes the Poisson limit of the charge resolution $\frac{\sqrt{Q}}{Q}$ and the noise contribution of the photodetector using the excess-noise factor (ENF). The ENF quantifies the gain stability of the photodetector. For this work it was set to $ENF = 0.1$ which is an optimistic, but reasonable estimate for both PMTs and SIPMs. According to (Vinogradov 2012) such a low ENF can be achieved with SIPMs even in the presence of pixel-to-pixel crosstalk in the low-gain regime. The third term parametrizes the contribution of the NSB on the charge resolution. The NSB rate that has to be considered for the normal CTA operation (requirement by CTA) is $NSB_{Rate} = 125$ MHz. Since the charge extraction algorithm uses a waveform integral over $T_{Int} = 14$ ns on average ~ 2 NSB photons are present in each waveform. An additional systematic charge uncertainty of $\sigma_{sys} = 5\,\%$ has been introduced to cover effects like temperature dependence of the transfer functions, module crosstalk (on the scale of a few %) and calibration uncertainties. This uncertainty is chosen to be an upper limit rather than the value to be achieved by the final TARGET generation.

The charge resolution calculation was performed for the gain assumption of 3 and 4 mV/p.e.. The error bars are given by the spread over 20 repetitions of the charge resolution measure-

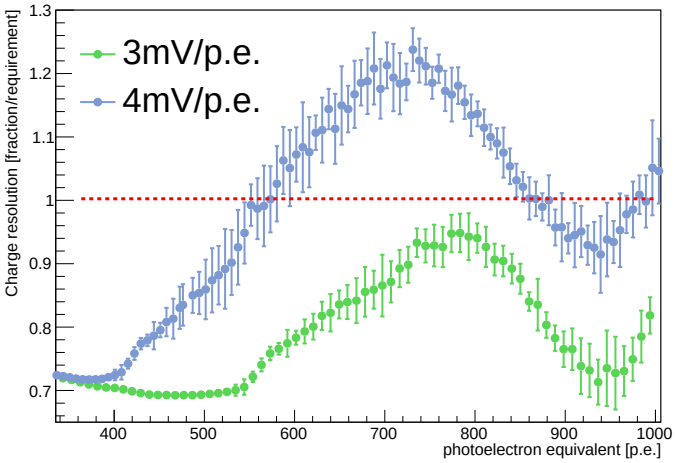

Figure 4.9: Relative charge resolution in the saturated regime for gains of 3 mV/p.e. in green and 4 mV/p.e. in blue. The CTA SST camera requirement is shown as a red dashed line.

ment. The charge resolution in the dynamic, non-saturated regime is shown in Figure 4.8 for 3 mV/p.e. for one channel. The determined resolution values have been divided by the SST requirement, so everything below one fulfils the requirement. Additionally the different contributions are shown starting from the pure Poisson limit. The TARGET modules fulfil the SST requirement in the whole dynamic regime.

The TARGET performance in the saturated regime is shown in Figure 4.9. The charge resolution is shown for both assumed gain values. Depending on the gain the saturated regime starts at different charge values. It is observable that the charge reconstruction performs much worse than in the dynamic regime. This is expected due to the small slope in the waveform observables with increasing charge. The requirement is fulfilled for 3 mV/p.e., but not for 4 mV/p.e.. The fact that the spread in the measured charge resolution vales is rather small shows that the developed charge extraction algorithm is very stable. No failed event reconstructions were detected in the whole saturated regime. The implication of the measurements in Figure 4.9 is that choosing a gain above 3 mV/p.e. is very dangerous for the TARGET 7 modules at least with the assumed value for σ_{sys}. On the other hand a 4 mV/p.e. gain is favored with respect to the performance of the trigger circuit. The higher the gain the lower the charge threshold of the trigger circuit. TARGET C + T5TEA will have to show in the future that they can achieve both charge resolution and trigger performance requirements with an appropriatly chosen gain.

CHAPTER 5

Conclusions

The goal of this work was to characterize the performance of the TARGET 7 readout modules with respect to charge resolution and to extract implications for the following TARGET generation, TARGET C + T5TEA. A charge extraction method has been developed that is able to extract the charge of an injected waveform in the charge range defined by the CTA requirements. It could be shown that the performance of this extraction algorithm is stable and produces reproducible results. It was furthermore shown that the TARGET 7 modules fulfil the charge resolution requirements for the CTA SST cameras if the gain is chosen in the range $\leq 3\,\mathrm{mV/p.e.}$ and the module crosstalk is neglected.

Implications for the TARGET C + T5TEA module generation that arose during the characterization of TARGET 7 are summarized in the following:

- The sampling path of TARGET 7 shows very low and homogeneous noise with respect to channel-to-channel variations. This circuit was therefore adopted nearly unchanged for TARGET C. No temperature dependence of the DC noise could be observed.
- The DC calibration methods introduced in this work lead to AC effects in the waveform observables. However these can be corrected relatively easy. A calibration method using individual transfer functions for every storage array capacitor is preferred over a method using averaged transfer functions due to its much better performance.
- The layout of the amplification circuit induces a huge channel-to-channel crosstalk. A stable operation with such a level of crosstalk is not possible. Solving this issue is one of the key goals of the TARGET C module design.
- The maximum trigger acceptance rate of the sampling path is within the requirements. Minor adaptations to the firmware are however necessary to achieve a dead time free operation with a duty cycle of one for trigger rates $\leq 600\,\mathrm{Hz}$.
- The waveform shape observables in the saturated regime show a rather large spread. This leads to a large charge uncertainty in the saturated regime. The amplification and shaping circuit of TARGET C has been designed to show a much larger waveform shape

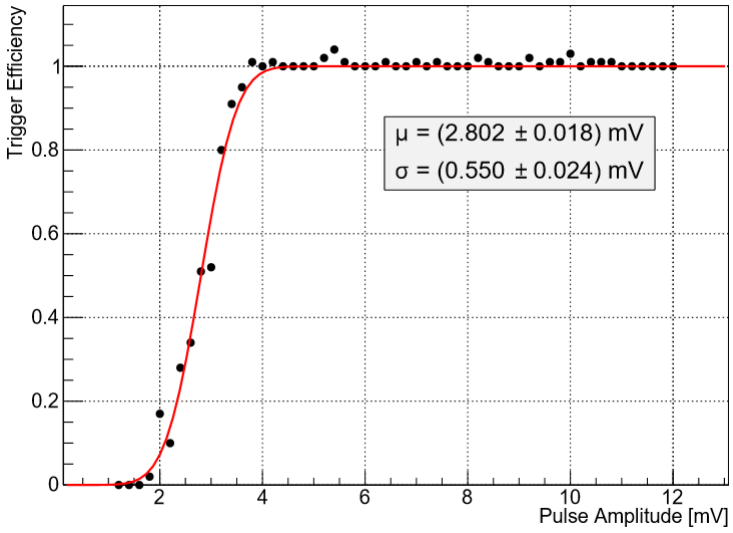

Figure 5.1: Preliminary trigger performance measurement for the T5TEA ASIC. The trigger threshold is reduced to $\sim 3-5\,\mathrm{mV}$ in different to the $\sim 60\,\mathrm{mV}$ threshold for the TARGET 7 trigger path.

variation in the saturated regime. The goal is to introduce such a high level of variation that even for saturated waveforms a simple waveform integral is usable.

The biggest issue for the TARGET 7 ASIC performance, the performance of the trigger path, has been solved with the new dedicated trigger ASIC T5TEA. It could be shown by Funk et al. (2016) that the trigger threshold of $\sim 60\,\mathrm{mV}$ for TARGET 7 is lowered to $\sim 3-5\,\mathrm{mV}$ for T5TEA. A preliminary trigger threshold measurement for T5TEA is shown in Figure 5.1.

In summary the TARGET sampling ASIC has proven to be very well suited for the operation in a CTA SST camera and for IACT cameras in general. Since the trigger performance issues will be solved with the newest TARGET generation, this combined readout system will be both cost-efficient and show a good performance.

Appendix

A.1 BDT Layout and Configuration

BDT Parameter	Value
Boosting	Gradient Boosting (BDTG)
Shrinkage	0.3
GradBaggingFraction	0.8
MaxDepth	3
nCuts	200
NTrees	500
NegWeightTreatment	Pray

Figure 5.2: BDT parameters used in this work. All other BDT parameters were left unchanged with respect to the standard values of TMVA version 4.2.0.

Bin Nr.	Energy Range [TeV]	Electron Training Events	Proton Training Events
1	[0.3,0.4]	95k	230k
2	[0.4,0.5]	80k	180k
3	[0.5,0.6]	69k	140k
4	[0.6,0.7]	60k	110k
5	[0.7,0.9]	100k	160k
6	[0.9,1.2]	105k	160k
7	[1.2,2.0]	155k	230k
8	[2.0,4.0]	150k	225k
9	[4.0,8.0]	100k	165k
10	[8.0,40.0]	130k	255k

Figure 5.3: BDT Layout with the energy ranges of the training bins and the number of simulated electron and proton events used for the training.

A.2 Stability of the ImPACT-MSSG Analysis

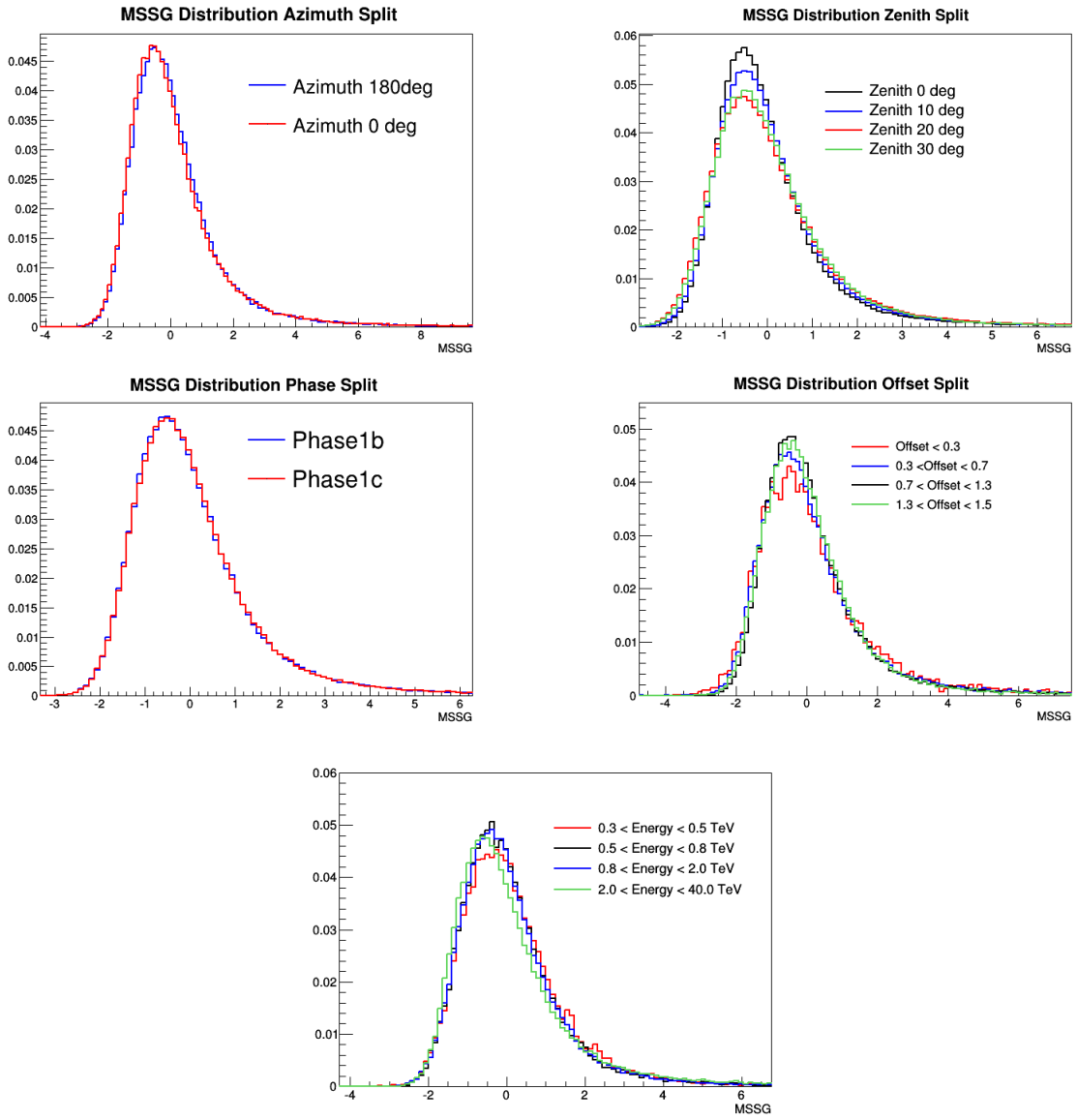

Figure 5.4: MSSG distributions for simulated electrons. The data has been split in azimuth angle, zenith angle, optical phase, offset angle and energy.

A.3 ZetaBDT Template Fits

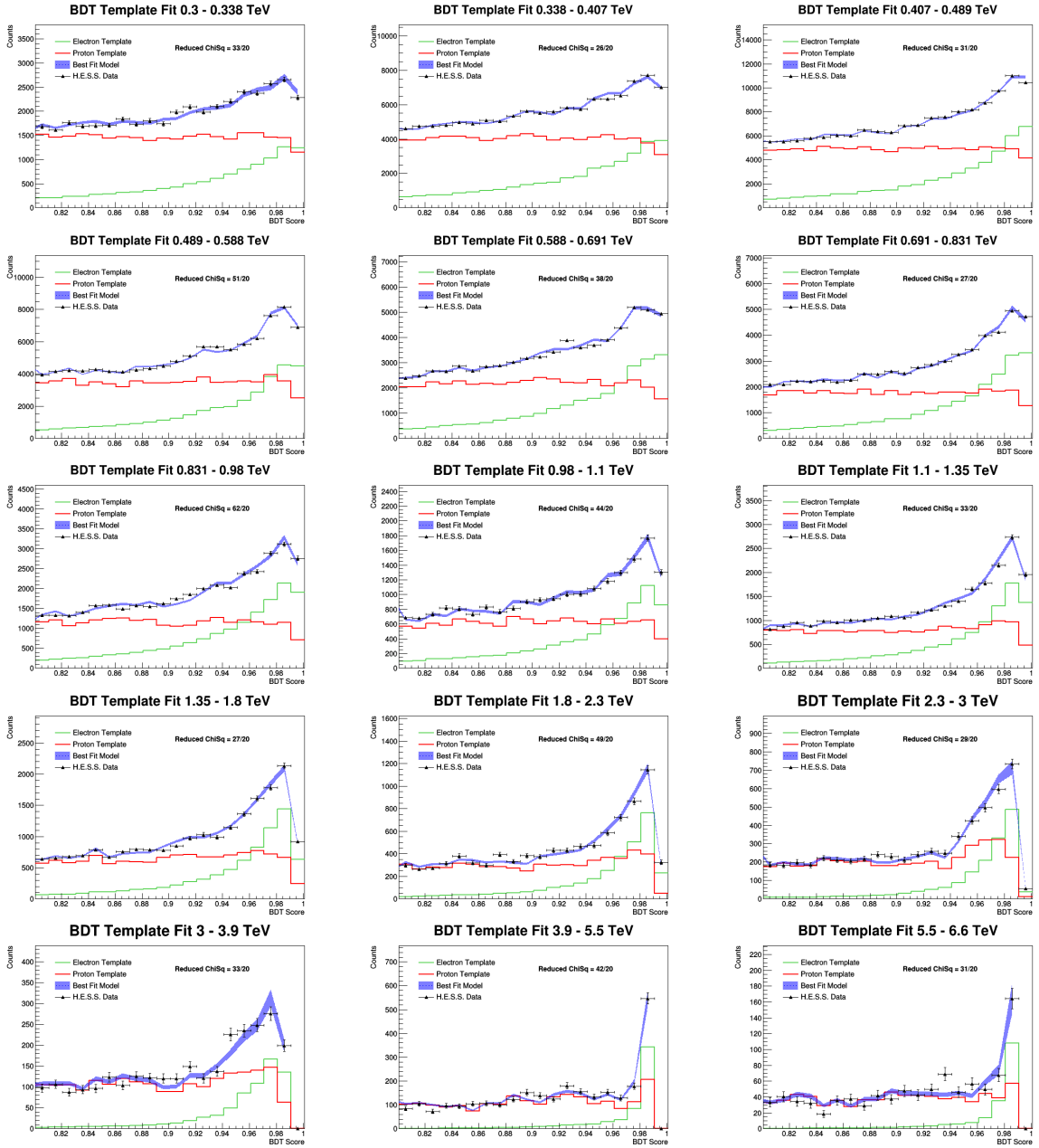

Figure 5.5: Template fits as derived with the ZetaBDT method for the cosmic-ray electron spectrum. The H.E.S.S. data is shown in black, the proton template in red, the electron template in green and the best-fit model in blue.

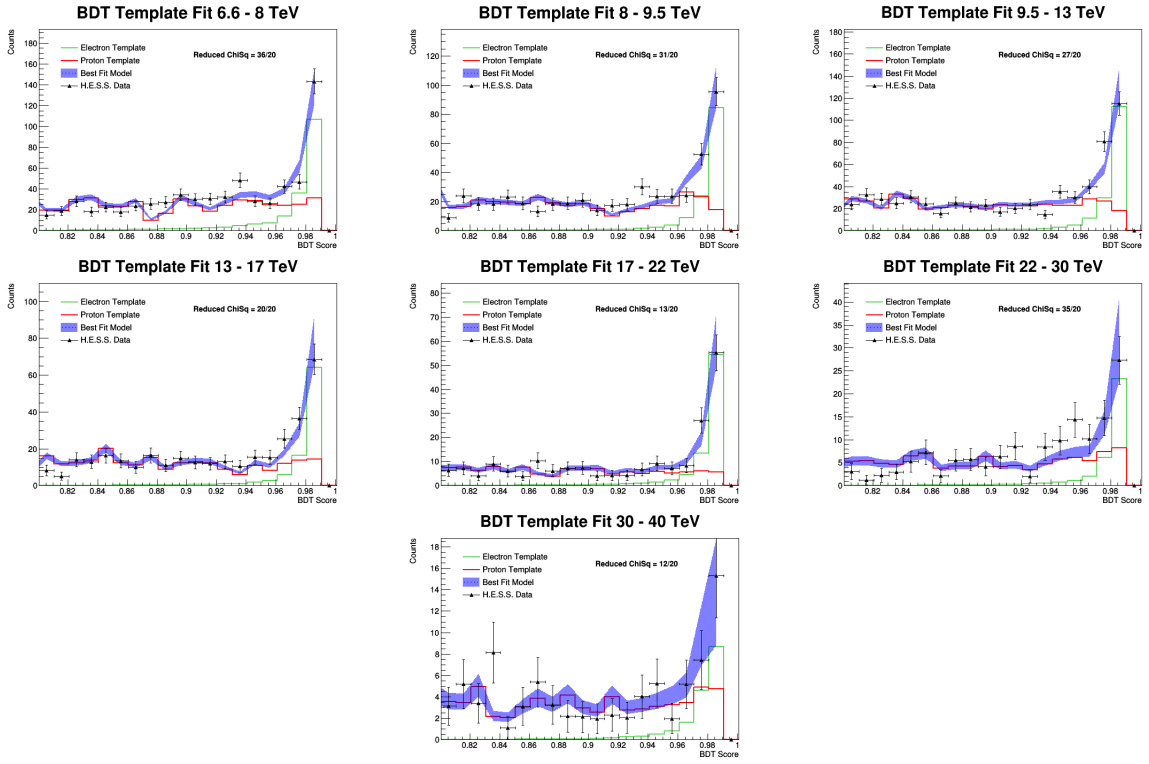

Figure 5.6: Template fits as derived with the ZetaBDT method for the cosmic-ray electron spectrum. The H.E.S.S. data is shown in black, the proton template in red, the electron template in green and the best-fit model in blue.

A.4 Local Sources Flux Fits

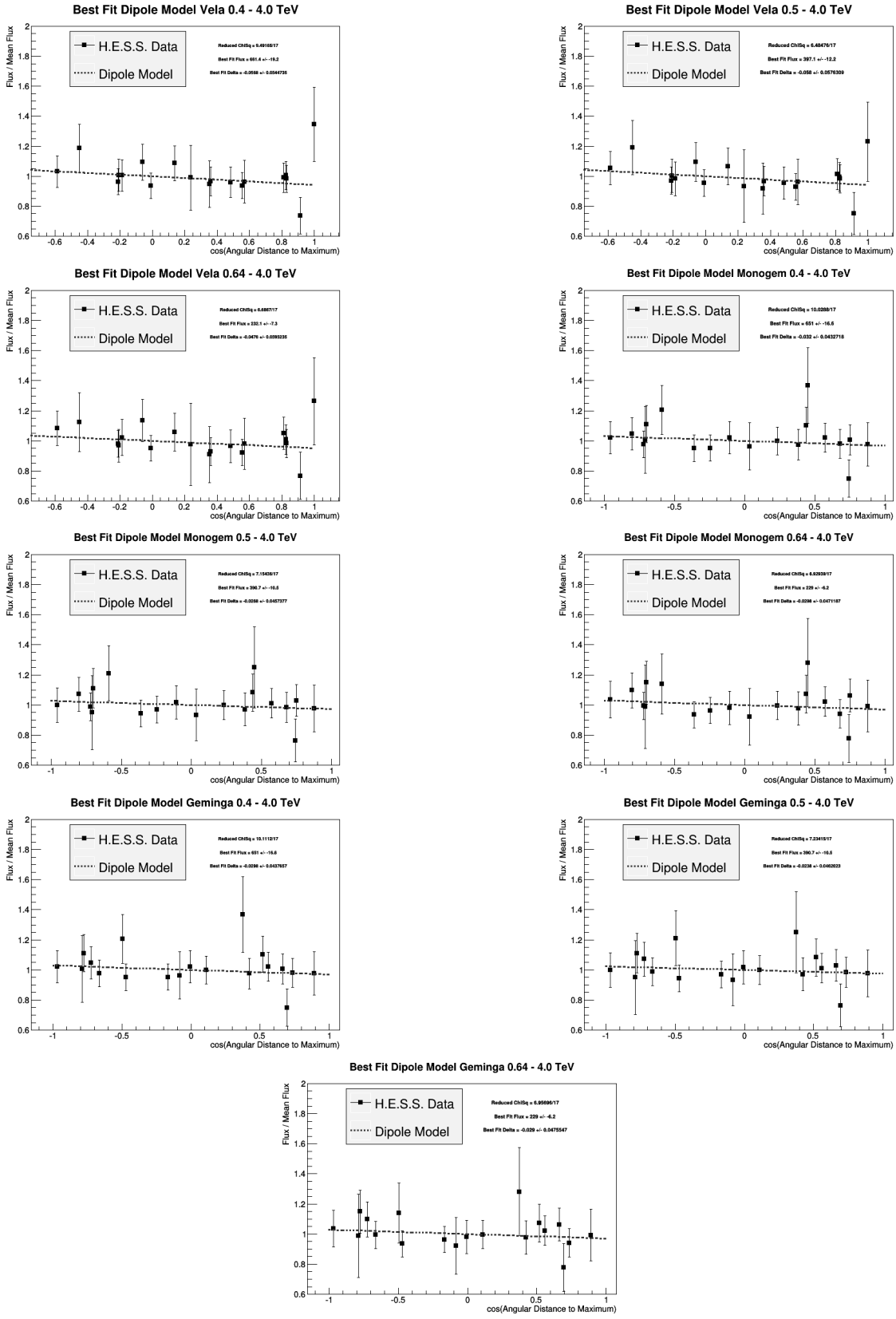

Figure 5.7: Anisotropy dipole model flux fits for the directions of Vela, Monogem and Geminga for all energy thresholds.

A.5 Model++ Anisotropy Cross-Check Plots

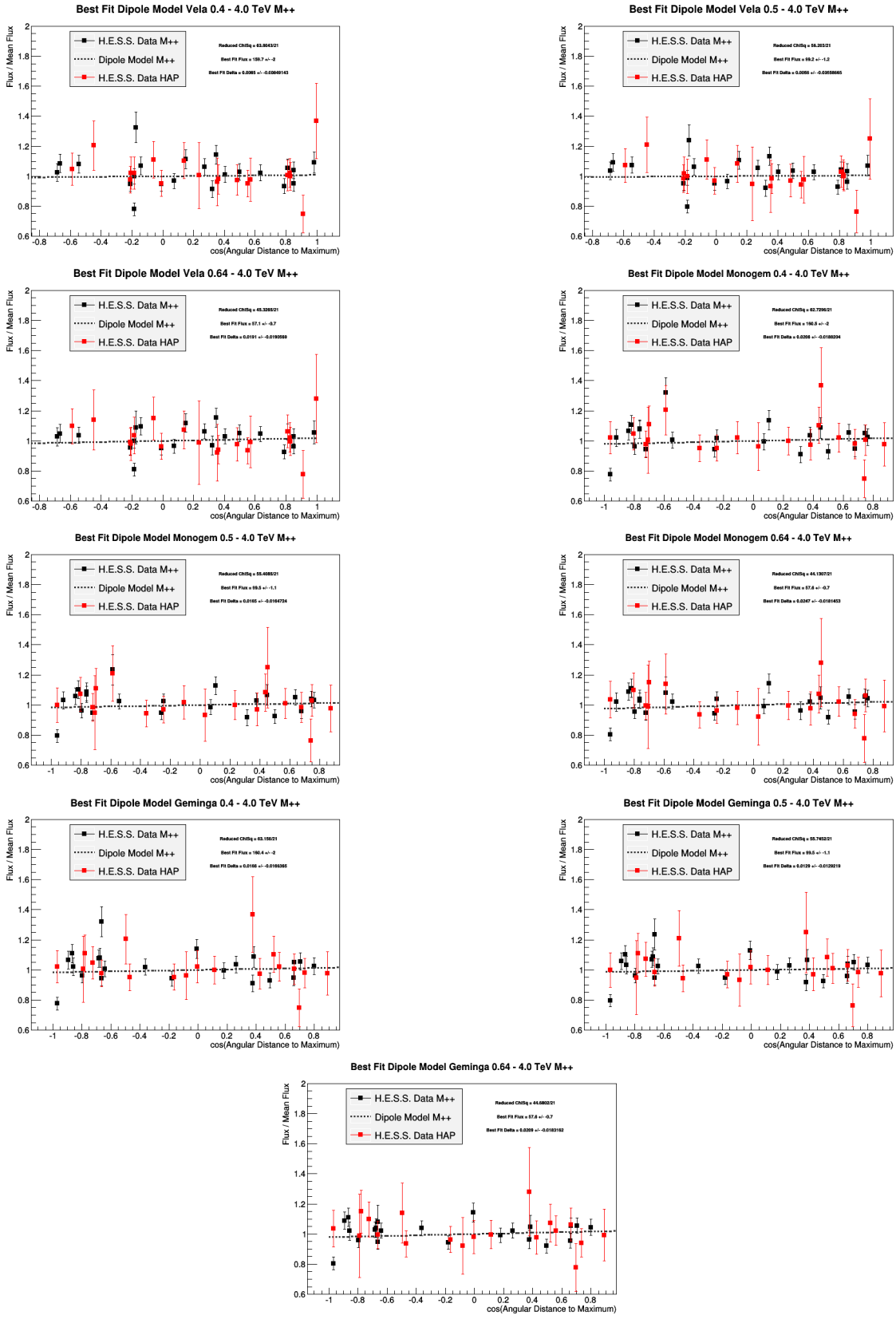

Figure 5.8: Anisotropy dipole model flux fits for the directions of Vela, Monogem and Geminga for all energy thresholds. The results derived in this work are shown in red, for PA Model++ in black.

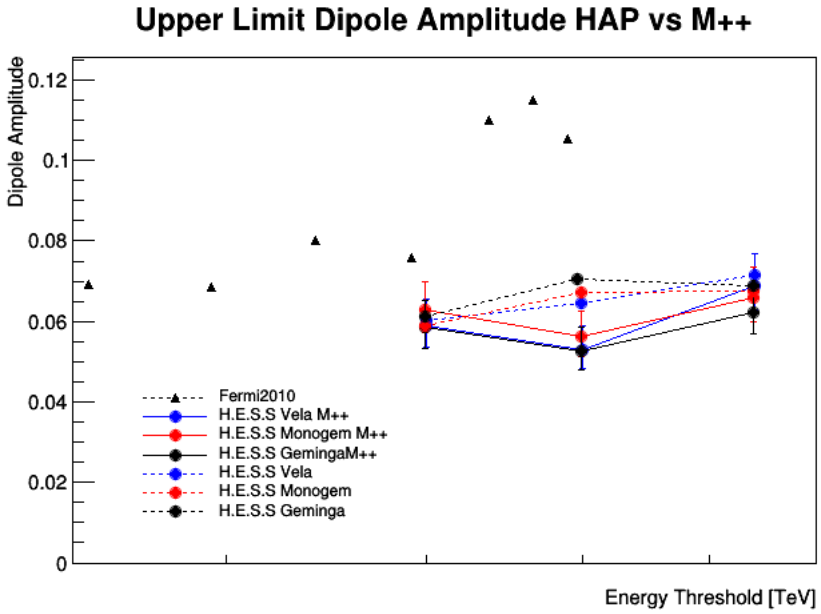

Figure 5.9: Upper limits on the dipole amplitude as determined by the dipole fit method for the directions of Vela, Monogem and Geminga. The limits are shown for HAP (solid lines) and PA Model++ (dashed lines).

A.6 TARGET 7 ASIC Register Values

Register Name	Register Value
CMPbias	0x4e
CMPbias2	0x2e1
DBbias	0x3d9
Isel	0xa2d
ITbias	0x3d9
PUbias	0xc28
Qbias	0x5dc
SBbias	0x480
SGN	0x000
SSPinLE_Delay	0x2e
SSPinTE_Delay	0x3d
SSToutFB_Delay	0x03a
VadjN	0x8bb
VadjP	0x480
Vbias	0x4b0
VANbuff	0x000
VAPbuff	0x3d9
Vdischarge	0x0000
Vqbuff	0x426
VtrimT	0x4d8
WR_ADDR_Incr1LE_Delay	0x3f
WR_ADDR_Incr1TE_Delay	0xe
WR_ADDR_Incr2LE_Delay	0x25
WR_ADDR_Incr2TE_Delay	0x34
WR_STRB1LE_Delay	0x23
WR_STRB1TE_Delay	0x2d
WR_STRB2LE_Delay	0x2
WR_STRB2TE_Delay	0xc

Acknowledgements / Danksagung

Eine erfolgreiche Promotion ist nicht nur eine Einzelleistung, sondern wird maßgeblich von den Menschen geprägt, die diese ermöglichen, unterstützen und begleiten. Im Folgenden möchte ich mich daher bedanken bei:

- Herrn Prof. Dr. Stefan Funk für das Vertrauen in meine Person, die gute Betreuung und die Freiheit in meiner Themenwahl.
- Herrn Prof. Dr. Christopher van Eldik und Frau Dr. Ira Jung für das Beantworten meiner zahlreichen Fragen und für die Unterstützung.
- Allen Kolleginnen und Kollegen am ECAP, insbesondere bei der Gamma-Gruppe. Danke für das wundervolle Arbeitsklima, die vielen schönen gemeinsamen Abende und natürlich die Unterstützung bei meiner Arbeit und meinem Vortrag.
- Meinen Arbeitskollegen David, Stefan und Alex aus Raum 309. Danke für die Abwechslung von Chaos und Produktivität, kein Tag war langweilig!
- Meiner Familie für die bedingungslose Unterstützung während meines gesamten Studiums und die Ermutigung das zu tun, was mir Spaß macht.
- Meiner Julia für Alles! Du trägst eine riesige Mitschuld an dieser Arbeit.

Bibliography

Abdollahi, S., Ackermann, M., Ajello, M., et al. 2017a, Physical Review Letters, 118, 091103

Abdollahi, S., Ackermann, M., Ajello, M., et al. 2017b, Phys. Rev. D, 95, 082007

Abe, K., Fuke, H., Haino, S., et al. 2016, ApJ, 822, 65

Abramowski, A., Aharonian, F., Ait Benkhali, F., et al. 2014, Phys. Rev. D, 90, 122007

Acharya, B. S., Actis, M., Aghajani, T., et al. 2013, Astroparticle Physics, 43, 3

Ackermann, M., Ajello, M., Albert, A., et al. 2015, ApJ, 799, 86

Ackermann, M., Ajello, M., Allafort, A., et al. 2012a, Physical Review Letters, 108, 011103

Ackermann, M., Ajello, M., Atwood, W. B., et al. 2012b, ApJ, 750, 3

Ackermann, M., Ajello, M., Atwood, W. B., et al. 2010, Phys. Rev. D, 82, 092003

Adriani, O., Barbarino, G. C., Bazilevskaya, G. A., et al. 2013, Physical Review Letters, 111, 081102

Adriani, O., Barbarino, G. C., Bazilevskaya, G. A., et al. 2011, Science, 332, 69

Aguilar, M., Aisa, D., Alpat, B., et al. 2014, Phys. Rev. Lett., 113, 221102

Aharonian, F., Akhperjanian, A. G., Anton, G., et al. 2009, A&A, 508, 561

Aharonian, F., Akhperjanian, A. G., Aye, K.-M., et al. 2004, Astroparticle Physics, 22, 109

Aharonian, F., Akhperjanian, A. G., Barres de Almeida, U., et al. 2008, Physical Review Letters, 101, 261104

Aharonian, F., Akhperjanian, A. G., Bazer-Bachi, A. R., et al. 2006, A&A, 457, 899

Aliu, E., Anderhub, H., Antonelli, L. A., et al. 2008, Science, 322, 1221

Ambrosi, G., Awane, Y., Baba, H., et al. 2013, ArXiv:astro-ph/1307.4565

Amenomori, M., Bi, X. J., Chen, D., et al. 2017, ApJ, 836, 153

Anderhub, H., Backes, M., Biland, A., et al. 2013, Journal of Instrumentation, 8, P06008

Atoyan, A. M., Aharonian, F. A., & Völk, H. J. 1995, Phys. Rev. D, 52, 3265

Bell, A. R. 2013, Astroparticle Physics, 43, 56

Bernlöhr, K. 2008, Astroparticle Physics, 30, 149

Bernlöhr, K., Carrol, O., Cornils, R., et al. 2003, Astroparticle Physics, 20, 111

Bleicher, M., Zabrodin, E., Spieles, C., et al. 1999, Journal of Physics G Nuclear Physics, 25, 1859

Borla Tridon, D. 2011, International Cosmic Ray Conference, 6, 47

Borriello, E., Maccione, L., & Cuoco, A. 2012, Astroparticle Physics, 35, 537

Bringmann, T., Calore, F., Di Mauro, M., & Donato, F. 2014, Phys. Rev. D, 89, 023012

Canestrari, R. 2011, SPIE Newsroom, doi: 10.1117/2.1201105.003727

Caroff, S. 2016, arXiv:astro-ph/1612.09579

Carrigan, S., Brun, F., Chaves, R. C. G., et al. 2013, arXiv:astro-ph/1307.4690

Chalme-Calvet, R., de Naurois, M., & Tavernet, J.-P. 2014, ArXiv:astro-ph/1403.4550

Chang, J., Adams, J. H., Ahn, H. S., et al. 2008, Nature, 456, 362

Cornils, R., Gillessen, S., Jung, I., et al. 2003, Astroparticle Physics, 20, 129

CTA Observatory homepage. 2017

Daniel, M. K., White, R. J., Berge, D., et al. 2013, ArXiv:astro-ph/1307.2807

Di Mauro, M., Donato, F., Fornengo, N., Lineros, R., & Vittino, A. 2014, jcap, 4, 006

Di Sciascio, G., Iuppa, R., & Argo-Ybj Collaboration. 2012, in Journal of Physics Conference Series, Vol. 375, Journal of Physics Conference Series, 052008

Ebisuzaki, S., Edwards, P. G., Fujii, H., et al. 1991, International Cosmic Ray Conference, 2, 611

Fermi, E. 1949, Physical Review, 75, 1169

Fletcher, R. S., Gaisser, T. K., Lipari, P., & Stanev, T. 1994, Phys. Rev. D, 50, 5710

Funk, S., Jankowsky, D., Katagiri, H., et al. 2016, ArXiv:astro-ph/1610.01536

Gaensler, B. M. & Slane, P. O. 2006, ARA&A, 44, 17

Gaisser, T. K. 1990, Cosmic rays and particle physics

Gargano, F. 2017, ArXiv:astro-ph/1701.05046

Glicenstein, J., Barcelo, M., Barrio, J., et al. 2013, ArXiv:astro-ph/1307.4545

Goldreich, P. & Julian, W. H. 1969, ApJ, 157, 869

Górski, K. M., Hivon, E., Banday, A. J., et al. 2005, ApJ, 622, 759

Hahn, J., de los Reyes, R., Bernlöhr, K., et al. 2014, Astroparticle Physics, 54, 25

Hahn, J., de los Reyes, R., Bernlöhr, K., et al. 2015, ArXiv:astro-ph/1502.01182

Heck, D., Knapp, J., Capdevielle, J. N., Schatz, G., & Thouw, T. 1998, CORSIKA: a Monte Carlo code to simulate extensive air showers.

Heitler, W. 1938, Proceedings of the Royal Society of London Series A, 166, 529

Hillas, A. M. 1985, International Cosmic Ray Conference, 3

Hillas, A. M. 2006, arXiv:astro-ph/0607109

Hinton, J. 2013, CTA Internal Note

Hinton, J. A., Funk, S., Parsons, R. D., & Ohm, S. 2011, ApJ, 743, L7

Hinton, J. A. & Hofmann, W. 2009, ARA&A, 47, 523

Hoecker, A., Speckmayer, P., Stelzer, J., et al. 2007, PoS, ACAT, 040

Holler, M., Balzer, A., Chalmé-Calvet, R., et al. 2015a, ArXiv:astro-ph/1509.02896

Holler, M., Berge, D., van Eldik, C., et al. 2015b, ArXiv:astro-ph/1509.02902

James, F. & Roos, M. 1975, Computer Physics Communications, 10, 343

Kerszberg, D. 2017, PhD thesis

Kirk, J. G., Lyubarsky, Y., & Petri, J. 2009, in Astrophysics and Space Science Library, Vol. 357, Astrophysics and Space Science Library, ed. W. Becker, 421

Kobayashi, T., Komori, Y., Yoshida, K., & Nishimura, J. 2004, ApJ, 601, 340

Kohnle, A., Aharonian, F., Akhperjanian, A., et al. 1996, Astroparticle Physics, 5, 119

Kopp, J. 2013, Phys. Rev. D, 88, 076013

Lenain, J.-P., Benbow, W., Boisson, C., et al. 2008, in American Institute of Physics Conference Series, Vol. 1085, American Institute of Physics Conference Series, ed. F. A. Aharonian, W. Hofmann, & F. Rieger, 415–418

Longair, M. S. 2011, High Energy Astrophysics

Manchester, R. N., Hobbs, G. B., Teoh, A., & Hobbs, M. 2005, VizieR Online Data Catalog, 7245

Manconi, S., Di Mauro, M., & Donato, F. 2017, jcap, 1, 006

Mao, C. Y. & Shen, C. S. 1972, Chinese Journal of Physics, 10, 16

Marrocchesi, P. S. 2015, ArXiv:astro-ph/1512.08059

Mathis, J. S., Mezger, P. G., & Panagia, N. 1983, A&A, 128, 212

Matthews, J. 2005, Astroparticle Physics, 22, 387

Mertsch, P. & Funk, S. 2015, Physical Review Letters, 114, 021101

Niemiec, J., Bilnik, W., Błocki, J., et al. 2015, ArXiv:astro-ph/1509.01824

Nozzoli, F. 2017, ArXiv:astro-ph/1701.00086

Obermeier, A., Boyle, P., Hörandel, J., & Müller, D. 2012, ApJ, 752, 69

Ohm, S., van Eldik, C., & Egberts, K. 2009, Astroparticle Physics, 31, 383

Ostapchenko, S. & Heck, D. 2005, International Cosmic Ray Conference, 7, 135

Otte, A. N., Biteau, J., Dickinson, H., et al. 2015, ArXiv:astro-ph/1509.02345

Pareschi, G., Agnetta, G., Antonelli, L. A., et al. 2013, ArXiv:astro-ph/1307.4962

Parsons, R. D., Bleve, C., Ostapchenko, S. S., & Knapp, J. 2011, Astroparticle Physics, 34, 832

Parsons, R. D. & Hinton, J. A. 2014, Astroparticle Physics, 56, 26

Paz Arribas, M., Schwanke, U., Wischnewski, R., & CTA Consortium, f. t. 2012, ArXiv e-prints

Pühlhofer, G. 2017, in American Institute of Physics Conference Series, Vol. 1792, 6th International Symposium on High Energy Gamma-Ray Astronomy, 080002

Pühlhofer, G., Bauer, C., Eisenkolb, F., et al. 2013, ArXiv:astro-ph/1307.3677

Punch, M. & H.E.S.S. Collaboration. 2001, International Cosmic Ray Conference, 7, 2814

Sommerfeld, A. 1931, Annalen der Physik, 403, 257

Spurio, M. 2014, Particles and Astrophysics (Springer)

Stahl, B. 2014, Internal Study

Staszak, D. 2015, arXiv:astro-ph/1508.06597

Strong, A. W., Moskalenko, I. V., & Reimer, O. 2004, ApJ, 613, 956

The HAWC Collaboration & The IceCube Collaboration. 2015, ArXiv:astro-ph/1510.04134

Tibaldo, L., Abchiche, A., Allan, D., et al. 2017, in American Institute of Physics Conference Series, Vol. 1792, 6th International Symposium on High Energy Gamma-Ray Astronomy, 080004

Tibaldo, L., Vandenbroucke, J., Albert, A., et al. 2015, in International Cosmic Ray Conference, Vol. 34, 34th International Cosmic Ray Conference (ICRC2015), 932

Tinivella, M. 2016, ArXiv:astro-ph/1610.03672

Vinogradov, S. 2012, Nuclear Instruments and Methods in Physics Research A, 695, 247

Völk, H. J. & Bernlöhr, K. 2009, Experimental Astronomy, 25, 173

Weekes, T. C., Cawley, M. F., Fegan, D. J., et al. 1989, ApJ, 342, 379